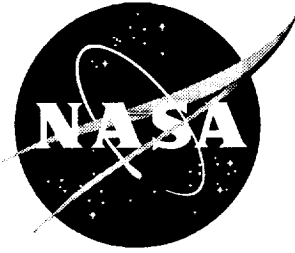


NASA/CR-1999-209717



# Development and Validation of a Supersonic Helium-Air Coannular Jet Facility

*Atherton A. Carty and Andrew D. Cutler  
Joint Institute for Advancement of Flight Sciences  
The George Washington University  
Langley Research Center, Hampton, Virginia*

National Aeronautics and  
Space Administration

Langley Research Center  
Hampton, Virginia 23681-2199

Prepared for Langley Research Center  
under Cooperative Agreement NCC1-217

---

November 1999

---

Available from:

NASA Center for AeroSpace Information (CASI)  
7121 Standard Drive  
Hanover, MD 21076-1320  
(301) 621-0390

National Technical Information Service (NTIS)  
5285 Port Royal Road  
Springfield, VA 22161-2171  
(703) 605-6000

# ABSTRACT

The development of high speed air-breathing propulsion technology is dependent in large part upon the efficient mixing of fuel and air in a supersonic flow environment. Incomplete mixing of fuel and air will result in less heat release in the combustion process than is potentially available, thereby reducing overall engine performance. Experimental research of supersonic reacting flows is difficult to carry out due the complex fluid phenomena which are present as well as the extremely harsh environment in which experimental models must operate. Computational research, while circumventing some experimental difficulties, requires the accurate modeling of these high speed flow phenomena and hence relies upon validation against experimental results. All too often however, these desired data do not exist at all, do not include the relevant computational flow parameters or do not accurately address computational cases of interest. This fundamental research project is undertaken in order to acquire data in a simple coannular He/air supersonic jet suitable for validation of CFD codes for high speed propulsion. Helium is employed as a non-reacting hydrogen fuel simulant, constituting the core of the coannular flow while the coflow is composed of air. The mixing layer interface between the two flows in the near field and the plume region which develops further downstream constitute the primary regions of interest, similar to those present in all hypersonic air breathing propulsion systems. A computational code has been implemented from the experiment's inception, serving as a tool for model design during the development phase.

# ERRATA

Subsequent to the completion of this research it was noted that a design or manufacturing error occurred which resulted in the centerbody of the nozzle being incorrectly located with respect to the outer body. The axial distance between the downstream end of the centerbody (i.e. the end of the nozzle middle contour) and the downstream end of the outer body with extension cone removed (i.e. the end of the nozzle outer contour) was 5.601 mm rather than 8.408 mm as called for in the design (see Figure 7). This has little effect on the nozzle contour in the vicinity of the area minimum and the region of supersonic flow downstream of this (except for the change in length) since the outer nozzle contour is essentially parallel to the axis in this region. (The radius of the outer contour at the area minimum which would have been 30.064 mm without the shift, is now 30.062 mm and the radius of the outer contour 64.114 mm downstream of the area minimum, which would have been 30.233 mm, is now 30.224 mm. These numbers are based on the design contours and the measured error in location and may not coincide exactly with the actual article.) Thus there is expected to be little effect of this error in the flow at the nozzle exit. However, because of the way the axial locations of the pitot surveys were measured, locations reported as 13 mm, 23 mm, ... 243 mm (measured with respect to the end of the centerbody) were in fact located 2.8 mm further downstream (i.e. at 15.8 mm, 25.8 mm, ... 245.8 mm). Additionally, axial locations reported in Section 3.1, Nozzle Contours are similarly in error, and the computational fluid dynamics calculations are for the nozzle as designed, not the actual geometry.

# TABLE OF CONTENTS

ABSTRACT.....	i
ERRATA .....	ii
TABLE OF CONTENTS.....	iii
LIST OF FIGURES .....	v
NOMENCLATURE .....	vii
1.0 INTRODUCTION .....	1
2.0 BACKGROUND .....	5
2.1 SUPERSONIC MIXING.....	5
2.2 2-D, PLANAR MIXING LAYERS .....	6
2.3 AXISYMMETRIC FREE AND COANNULAR JETS .....	10
3.0 EXPERIMENTAL MODEL.....	13
3.1 NOZZLE CONTOURS.....	13
3.2 MODEL ASSEMBLY .....	18
4.0 EXPERIMENTAL METHOD.....	22
4.1 TEST FACILITY AND PROCEDURE .....	22
4.2 PITOT SURVEYS .....	27
4.3 FOCUSING SCHLIEREN .....	33
5.0 COMPUTATIONAL ANALYSIS .....	36
5.1 AXISYMMETRIC COMPUTATIONAL CODE.....	36
5.2 CODE MODIFICATIONS .....	37

6.0 RESULTS .....	40
6.1 CFD NOZZLE DESIGN VALIDATION .....	40
6.2 SCHLIEREN IMAGES.....	43
6.3 PITOT PROBE SURVEYS .....	46
7.0 SUMMARY .....	52
8.0 APPENDIX A - MANUFACTURING DETAILS.....	55
9.0 APPENDIX B - UNCERTAINTY ANALYSIS .....	60
10.0 REFERENCES .....	63
11.0 FIGURES.....	67

# LIST OF FIGURES

Viscous Corrected Nozzle Contours	67
Viscous Corrected Nozzle Contours - Throat Region	67
Transverse Jet Facility Adaptor Flange	68
Centerbody Support Flange	68
Centerbody Secured in Support Flange	69
Coflow Nozzle Body Mounted and Centered	69
Coannular Nozzle	70
Transverse Jet Facility	71
Pitot Probe Response Time	72
Probe Survey Rake	72
Probe Translation Mechanism Installed on Model	73
Focusing Schlieren Flow Visualization System	73
Computational Grids - 201x51 Coflow, 201x25 Centerjet	74
Computational Grids - Clustering in Throat Regions	74
CFD Mach Contour Calculation - Air / He	75
CFD Mach Contour Calculation - Air / He	75
CFD Pressure Contour Calculation - Air / He	76
CFD Pressure Contour Calculation - Air / He	76
Exit Plane Mach Profile	77
Exit Plane Mach Profile: Detail	77
Coflow Nozzle Exit Plane Boundary Layer: Outer Wall	78
Coflow Nozzle Exit Plane Boundary Layer: Inner Wall	78
Centerjet Nozzle Exit Plane Boundary Layer	79
Exit Plane Velocity Profile - Air Center Jet	79
Focusing Schlieren Images Comparing Air and Helium Centerjet Flows	80
Focusing Schlieren Image in Vicinity of Air Centerjet Nozzle Exit	81
Focusing Schlieren Image in Vicinity of Helium Centerjet Nozzle Exit	81
Centerjet Nozzle Exit Flow Structure	82

Pitot Pressure Surveys - 3-4mm	83
Pitot Pressure Surveys - 13mm	83
Pitot Pressure Surveys - 23mm	84
Pitot Pressure Surveys - 33mm	84
Pitot Pressure Surveys - 43mm	85
Pitot Pressure Surveys - 63mm	85
Pitot Pressure Surveys - 83mm	86
Pitot Pressure Surveys - 103mm	86
Pitot Pressure Surveys - 123mm	87
Pitot Pressure Surveys - 143mm	87
Pitot Pressure Surveys - 163mm	88
Pitot Pressure Surveys - 203mm	88
Pitot Pressure Surveys - 243mm	89
400 pt. Air Centerjet Nozzle Surveys - 3mm through 243mm	89
100 pt. Helium Centerjet Nozzle Surveys - 3mm through 243 mm	90
Comparison of CFD and Experimental Survey Results at Exit Plane	90
Helium Centerjet Nozzle Surveys with Specified Reference Planes	91
Helium Centerjet Nozzle Surveys - Definition of Mixing Layer Edges	91
Coannular Jet Growth	92
Averaged Coannular Jet Growth	92
Normalized Spreading Rate Comparison with Dimotakis Correlation	93
Transverse Jet Facility Adaptor	94
Centerjet Flow Straightener	95
Centerbody Support Flange	96
Centerbody	97
Coflow Nozzle Outer Body	98
Coflow Nozzle Extension Cap	99
Model Assembly Drawing	100
Alignment Hardware	101



# NOMENCLATURE

$A$	area
$a$	speed of sound
$D_{ref}$	coflow nozzle reference diameter
$M$	Mach number
$n$	index of refraction
$p$	pressure
$Re$	Reynolds number
$U, u$	velocity component in the x-direction
$V, v$	velocity component in the x-direction
$x$	length in streamwise direction, axial coordinate

## Symbols

$\gamma$	ratio of specific heat capacities
$\delta^*$	boundary layer displacement thickness
$\delta'$	growth rate (shear layer)
$\theta$	flow angle measured from axial centerline
$\phi$	velocity potential
$\rho$	density
$\lambda$	wavelength

## Subscripts

$c$	convective
$e$	nozzle exit
$i$	incompressible
$o, t$	stagnation (total) pressure condition
$p$	pitot probe measurement
1	coflow (air composition)
2	centerjet (helium or air composition)
$\infty$	freestream
$M$	minimum total pressure
$CL$	centerline (pressure)
*	sonic or throat condition

## Abbreviations

CCD	charge coupled device
CFD	computational fluid dynamics
EDM	electrical discharge machining
psia	pounds per square inch (absolute)
scramjet	supersonic combustion ramjet

# 1.0 INTRODUCTION

Over the course of the past several decades enormous strides have been made in the field of high speed propulsion. A common incentive to develop such propulsion systems is for use in a single stage to orbit (SSTO) successor to the space shuttle. Such a vehicle would need the capability of sustained cruise in the hypersonic flight regime, that of Mach 5 and greater. A now commonly held belief is that the use of an airbreathing engine such as the supersonic combustion ramjet (or SCRamjet) is essential to the success of a future SSTO vehicle. Development of such a propulsion system will drastically reduce the price per pound of payload delivered to orbit and dramatically increase access to space.

Rocket propulsion has for quite some time represented a viable solution to this high speed propulsion problem with one inescapable drawback to their economical use in such an application. A rocket powered vehicle must carry along with it not only fuel but also oxidizer required to burn this fuel (which typically accounts for a large percentage of the launch weight), greatly reducing the available vehicle payload capacity<sup>1</sup>. A current multi-stage rocket system weight fraction breakdown includes 65% oxidizer and 24% fuel and in fact, prior to its lift-off for the moon the Saturn V rocket weighed over 6 million lbf, 4 million lbf of which was composed of liquid oxygen alone<sup>1</sup>. Clearly then, airbreathing engines possess a marked potential advantage over rocket powered vehicles from an efficiency standpoint. This advantage, however, is significantly offset by the new technical challenges encountered in the implementation of these advanced propulsion concepts, many of which have to date not been resolved.

Existing airbreathing engines capable of sustained operation at high speeds (such as ramjets and their derivatives) require that air injected into the engine be decelerated to subsonic

speeds in order to facilitate effective mixing and combustion. This process results in large losses in total pressure and static temperature which can easily exceed material limits. In addition, these excessive temperatures may lead to the dissociation of the air itself, further reducing the amount of energy which may be reaped in the combustion process if recombination does not occur.

The scramjet engine has come about in an effort to circumvent many of the aforementioned difficulties by maintaining supersonic flow through the entire engine. The pressure losses as well as the thermal and structural loading encountered as a hypersonic flow is slowed to subsonic speeds (as is the case in the conventional ramjet engine) would be greatly reduced if the flow remained supersonic throughout the propulsion unit. In addition, these relaxed design constraints allow the expansion of the vehicle operational range as previous thermal and structural limitations permit vehicle operation at higher speed levels. As the velocity of engine throughflow increases however, other problems, this time fluid mechanical in origin, emerge as the limiting performance parameters.

The high speed mixing of fuel and air as well as its subsequent combustion have emerged as paramount technical issues yet to be resolved. The size of the engine combustor is limited by weight restrictions, so that fuel must be mixed and burned over a very short physical distance. Injection of fuel perpendicularly into a supersonic airstream has been shown to be efficient. However this configuration can often lead to unacceptable total pressure losses. In higher operational speed regimes, the percentage of overall thrust generated by the fuel injectors themselves becomes an increasingly larger percentage of the overall thrust<sup>1</sup>. Orientation of the injectors in a streamwise direction maximizes the direct thrust contribution of the fuel injectors while adversely affecting mixing efficiency of the fuel and air.

Experimental engine testing of the aforementioned propulsion concepts is

notoriously difficult and expensive. For this reason, the development of computational tools capable of accurately predicting these types of flows is of great interest. The experiment which is the subject of this thesis is intended to provide data in a simple flow which can be used to test and validate such codes. In particular, it is the intent to provide data which will test the empirically-based models for turbulence stresses and mass transfer (mixing) that they use. Thus, an axisymmetric coannular jet in which the center jet is a light gas (simulating a scramjet fuel), the coflow is air, and which discharges into stagnant air is selected for this study. Being axisymmetric, this geometry presents fewer numerical difficulties for code developers and requires only modest computer resources, and having regions where the different gases mix, it should provide a sensitive test of turbulence modeling aspects of the codes. Since much of the thesis work involved the design and manufacture of the test hardware, only preliminary test data are presented here. This includes focusing schlieren flow visualization and pitot probe surveys of the jet flow field. In these tests, the center jet gas was helium.

It is anticipated (and the facility was designed with this in mind) that more sophisticated diagnostic techniques would be employed in future tests utilizing the hardware. In particular, the RELIEF<sup>2</sup> flow velocimetry technique will be employed. For these tests, the center jet gas would be a mixture of 95% helium and 5% oxygen (the gas for which the facility was designed). In the RELIEF method the oxygen molecules are first tagged by exciting them from one energy state to another by stimulated Raman scattering. The lifetime of this energy state is relatively long and, by causing the tagged molecules to fluoresce, the location of these oxygen molecules can be found at some later time using an Planar Laser-Induced Fluorescence. Knowing the initial location of the molecules (the tagged line) at the time they were tagged as well as at some later time, the fluid velocity can be deduced.

Clearly this mixing study neglects the process of combustion as well as its effects on

the fluid flow. Nevertheless, for the sake of experimental practicality this approach represents a useful alternative to addressing the entire problem of supersonic combustion and mixing, allowing focus on the physics of turbulent mixing, absent heat release.

Many aspects taken into account in the design and fabrication of this experimental model were ultimately driven by the need to provide simple, well defined boundary conditions to the flow field, and accurate data in the flow field itself. Great care was taken to design and fabricate a model which would produce a uniform flow at the nozzle exit plane, and for which both the inner and outer nozzle geometries were accurately defined and manufactured. Steps were also taken to provide good optical and probe access, so as to ensure high quality data throughout the jet flow field.

## **2.0 BACKGROUND**

### **2.1 SUPERSONIC MIXING**

The problem of mixing at the interface between two turbulent moving fluid media of either dissimilar composition or differing speeds (or both) has been the topic of extensive experimental, computational and analytical research. Supersonic mixing in particular, has been a focus of many research efforts due to the important role which it plays in the arena of high speed air-breathing propulsion concepts. In fact, the entire operational premise upon which a supersonic combustion ramjet is based depends upon the efficient mixing of fuel and air at high speed. The following survey does not by any means constitute a complete accounting of the work conducted in this and other related fields. However it does identify several fine examples relevant to the field of supersonic shear layer mixing.

Many of the most detailed studies of supersonic mixing have concentrated on the 2-D planar mixing layer between two freestream flows at different velocities (and usually also of different compositions). Such flows are inherently simpler than axisymmetric jets (in which mixing occurs with the stagnant surrounding air) or coannular jets (in which mixing occurs between central and annular jets). This greater simplicity comes about due to the fact that 2-D planar mixing layers relatively quickly achieve self-similarity, where profiles of flow variables at subsequent streamwise stations are similar in shape<sup>3</sup>. On the other hand, axisymmetric jets have a nearfield region where there exists a two-stream mixing layer around the jet circumference which is similar to the 2-D planar mixing layer. Further downstream however, the central core which consists of pure centerjet fluid disappears due to the mixing layer growth. The region located

downstream of this point is called the plume. In so far as the validation of codes for a scramjet engine application is concerned, coannular jet flows are of the greatest interest. This is because in a scramjet, gaseous fuel (typically a light gas such as hydrogen) is injected as a jet, and the subsequent fuel - air mixing occurs in both two stream mixing layers and plumes, although plume regions comprise the major part of the engine combustor.

The references pertinent to the current research have therefore been divided into two distinct technical areas: 2-D planar mixing layers, and axisymmetric and coannular jets.

## **2.2 2-D, PLANAR MIXING LAYERS**

The research of Brown and Roshko<sup>4</sup> addressed and subsequently validated the belief that significant supersonic mixing layer growth rate reduction observed with increasing Mach number stemmed from flow compressibility effects and not density differences alone. This was accomplished by studying incompressible mixing layers in which large density differences were achieved through the use of different gas compositions - such as nitrogen and helium. They observed that although there was a small effect of density on mixing layer growth rate (the change in mixing layer thickness with respect to axial distance) in the incompressible case, this effect was very much smaller in the subsonic case than that found in the corresponding compressible supersonic case, thus proving the dependence of mixing layer growth rate upon compressibility.

This dependence upon compressibility (in plane shear layers) was further considered by Bogdanoff<sup>5</sup> and later by Papamoschou and Roshko<sup>6,7</sup>. In this research a natural coordinate system was established which moves with the large scale turbulent structures present in the shear layer. Within this system an alternative Mach number, the convective Mach number or  $M_c$ , is



defined in an effort to parameterize the aforementioned effect of compressibility. The  $M_c$  is defined as the convection velocity of the large scale structures in the shear layer relative to either of the freestream flows, normalized by the freestream speed of sound. Citing the previous work of Brown and Roshko<sup>4</sup>, Bogdanoff estimates that the supersonic planar shear layer growth rate drops to 20% of the incompressible spreading rate for equal velocity and density ratio. Papamoschou and Roshko<sup>6</sup> observed in schlieren flow visualization experiments a reduction of growth rate by a factor of 3-4 overall with increasing  $M_c$ . The rate of reduction of growth rate becomes significant at around  $M_c=0.5$  and then becomes small as  $M_c$  exceeds 1.0. Bogdanoff attributed this growth rate reduction at least in part to the decrease in the maximum growth rates of Kelvin-Helmholtz instabilities.

Later research conducted by Papamoschou and Roshko<sup>7</sup> involved a broadening of the scope of previous research, studying various combinations of gases at Mach numbers from 0.2 to 4.0. This investigation, however, focused on the use of Pitot-pressure surveys for measurement of growth rates (as opposed to schlieren measurements used previously). As before,  $M_c$  was used for correlating the growth rate. Growth rate was again found to decrease with increasing  $M_c$ , asymptotically approaching 20% of the corresponding incompressible growth rate for  $M_c$  near unity. This implied that in the convective frame of reference compressibility comes into play before any shock or expansion waves appear. It was taken to be significant that relative to this convective frame of reference all velocities are subsonic and potentially dominated by subsonic-type instabilities (despite the fact that the region is supersonic with respect to ambient). Furthermore, it was suggested that this is connected to the fact that the shear layer remains unstable regardless of the magnitude of  $M_c$ .

The publication of Dimotakis<sup>8</sup> serves as a summary of much of the theory of turbulent

planar mixing layers touched on above and includes extensive reference sections on the subject as well. In a more recent work, Dimotakis<sup>9</sup> estimated the convection velocity of turbulent large scale structures in low  $M_c$  supersonic mixing layers. The work was motivated by recent experiments suggesting that convection velocities of two-dimensional turbulent structures at high convective  $M_c$  are much closer to one of the two freestream flows than at lower (compressible) ones. The strength of shocks generated by these turbulent structures (assumed to be born within the mixing layer and to propagate into one of the two freestreams) was obtained by assuming the flow, taken in a reference frame moving at the convective velocity (the Galilean frame of reference), is stationary with respect the large scale structures. This is to say that the analysis of Dimotakis is based on the temporal behavior of the large scale structures in a convective (Galilean-invariant) frame of reference. Utilizing shock strength derived in this stationary frame, the convection velocity was estimated (along with the  $M_c$ ) by matching estimated total pressures at the stagnation points of the turbulent structure in the convective frame. Convection velocity was claimed to play a significant role in the process of shear layer entrainment in this work.

As discussed in the work of Clemens and Mungal<sup>10</sup>, recent experiments in compressible planar mixing layer seem to suggest that the actual flow structure at compressible Mach numbers undergoes a transition from the low speed quasi-two dimensional (but turbulent) spanwise coherent vortical structures of Brown and Roshko. Their Planar Laser Mie Scattering (PLMS) visualizations indicate a transition to a relatively random three dimensional structure as convective Mach number increase to around 0.62. PLMS and Planar-Laser-Induced Fluorescence (PLIF) measurements also led them to identify an apparent change in entrainment mechanism with increased compressibility as well. Changes in the flow structure were indicated by a typical mixture fraction field exhibiting different entrainment motions at differing compressibility

conditions. Flow uniformity observed to be prevalent in the cross-sectional direction with a gradient in the streamwise direction at  $M_c = 0.28$  was found to exhibit the opposite trend (a mixture fraction field of greater uniformity in the streamwise direction and a gradient in the cross-sectional direction) at  $M_c = 0.62$ . The mixture fraction statistical results (including probability density functions (PDF) and root mean square (RMS) fluctuations) concur with qualitative observation and suggest that mixture fraction fluctuations are reduced in magnitude by increased compressibility effects.

## 2.3 AXISYMMETRIC FREE AND COANNULAR JETS

This final section is a description of the most relevant studies of axisymmetric jets, including several early studies of jets in stagnant air (free jets), and then a more comprehensive review of the coannular jets literature. Some of the earliest studies of the theory of turbulent jets by Abramovich<sup>11</sup> et. al. utilized an axisymmetric jet experimental configuration. This research resulted in characterization of turbulent gas jets in varied configurations including free, confined, submerged and coflowing jets, wakes behind bluff bodies, and jets confined by solid walls.

The work of Smits and Dussauge<sup>12</sup> serves as a more current summary of the field of turbulent shear layers in supersonic flow, providing a review of pertinent flow physics in general and, in several instances, focusing upon axisymmetric free and coannular jets in particular.

The work of Fourquette, Mungal and Dibble<sup>13</sup> was undertaken to investigate the evolution of the mixing layer of an axisymmetric supersonic free jet in the near field of the nozzle exit. In particular a comparison was sought of these results obtained employing a non-intrusive two dimensional laser Rayleigh scattering technique with the aforementioned experimental results of Papamoschou and Roshko<sup>7</sup>. Good agreement was found overall, with the exception of increased three dimensionality (such as rotated flow structures), visible using the planar Rayleigh scattering technique<sup>13</sup> but obscured in the schlieren technique<sup>7</sup>.

A direct numerical simulation of an axisymmetric free jet was conducted by Freund, Lele and Moin<sup>14</sup> at a Mach number of 1.92 and results compared to a nearly incompressible simulation at Mach 0.4. Intended for use in the study of supersonic jet noise, this computation captured flow features similar to those present in the planar shear layers. It was in part motivated by recent findings of linear theory which (as do to the previously mentioned experimental results) indicate

increased three dimensionality with increasing Mach number as oblique instability modes become more unstable than the two dimensional modes dominating incompressible flow. The results of the study were found to indicate negligible dilatation effects in both cases considered and a suppression of pressure fluctuations in the supersonic case which, it has been suggested, may suppress growth rate via the effect on the pressure-strain-rate term of the Reynolds stress transport equation. In addition, a decreased importance of the pressure-diffusion term of the turbulent kinetic energy transport equation in the supersonic case compared to the subsonic case was identified. This term acts to transport turbulent kinetic energy into regions of high shear.

Early work pertaining to the area of coannular jets, which examined subsonic and supersonic jet streams exhausting into a supersonic stream, was conducted by Wilder and Hindersinn<sup>15</sup>. These experimental results were successfully correlated with a simple theoretical analysis for the prediction of jet spreading which contained coefficients evaluated with the aforementioned experimental data. In addition, the effects of normal and oblique shock structures on jet streams were addressed in this research. The most rapid mixing and corresponding breakup of supersonic jet stream structure came as a result of interaction with a normal shock. Similar research conducted with oblique shock structures was shown to agree with jet stream contraction and displacement predictions of 2D plane shock theory.

The next three noted references all contain different works of the same group of researchers, Gutmark, Schadow and Wilson<sup>16,17,18</sup>. These works bear significant resemblance to the present research and hence comprise a good basis for comparison. They considered coaxial jets where the centerjets were generated by various circular and rectangular nozzles. Cases were considered both with and without the outer annular coflows. Pitot pressure and gas sampling probe surveys were obtained in addition to schlieren flow visualization. The compressible growth

rate was defined as the axial rate of change of the centerjet mixing layer thickness. Without coflow this thickness is defined as the radial distance between the point at which the pitot pressure equals 5% of the value on the centerline and the point at which it equals 95% of the value on the centerline. The pitot pressure is assumed measured relative to ambient (gauge). With coflow, the centerjet mixing layer thickness is defined between the point where the pitot pressure equals the coflow value plus 5% of the difference between the coflow and centerline values, and the point where it equals the coflow value plus 95% of this difference. For circular centerjets, compressible growth rate was observed to fall gradually with convective Mach number, reaching a plateau for  $M_c > 1.4$  where the growth rate was 0.2 to 0.3 of the incompressible value. The centerjet changed its growth rate as a function of axial distance, with a near field transitional region having a different rate than the fully developed far field region. It was also established that growth rate comparisons must be based upon the same criteria for width measurement since results based upon schlieren images, and other criteria based upon the pitot data were all different.

## 3.0 EXPERIMENTAL MODEL

### 3.1 NOZZLE CONTOURS

As described previously, a model was designed for this study to provide a simple coannular flow with mixing between the centerjet and coflow and with well defined boundary conditions. In order that this flow should be fundamentally similar to those mixing flows which exist in scramjets, the centerjet fluid was a light gas (which has a higher speed of sound than air) while the coflow was air. The Mach number of both centerjet and coflow was selected to be about 1.8, which is representative of the Mach numbers of fuel and air in a scramjet combustor in the low end of the hypersonic speed range. The design calculations assumed that the centerjet was a mixture of 95% helium and 5% oxygen, as required by the RELIEF velocimetry technique, although the tests reported here utilized pure helium due to time and economic constraints. This selection of parameters provided a centerjet velocity greater than that in the coflow, with convective Mach number (actually, the average of  $M_{c1}$  and  $M_{c2}$  - see Section 6.3) in the mixing layer between the centerjet and coflow of about 0.704 for the helium-oxygen mixture and 0.823 for pure helium, i.e., compressible. Quasi- 1D calculations are used to obtain values of  $u_1, u_2, a_1, a_2, \rho_1, \rho_2$  as described in Section 4.1.

The model was thus designed to form two nozzles, the coflow nozzle and the centerjet nozzle (which was within a centerbody, the exterior of which formed part of the coflow nozzle). These nozzles were designed so as to provide the flow required while maintaining structural integrity and stiffness. Figures 1 and 2 are plots of the nozzle contours utilized in this study. The outer and middle contours represent the interior surfaces of the coflow nozzle while

the inner contour represents the interior surface of the centerjet nozzle. The area minimum of the outer nozzle lies at an axial distance of 6.845 inches (173.87 mm) and at this point the middle contour diameter is 1.349 inches (34.26 mm) and the outer contour diameter is 2.367 inches (60.13 mm); the area minimum of the inner nozzle lies at an axial distance of 9.026 inches (229.26 mm) and at this point the inner contour diameter is 0.3335 inches (8.47 mm). The exit plane of the centerjet nozzle lies at an axial distance of 9.370 inches (238.00 mm) and at this location the inner nozzle diameter is 0.3937 inches (10.000 mm), the middle nozzle diameter is 0.4134 inches (10.500 mm) and the outer nozzle diameter is 2.380 inches (60.47 mm). Note however that for practical reasons the outer contour does not terminate at this point in the experimental model - this will be discussed later.

The design of the experimental model began with the specification of the nozzle contour coordinates. This was done in several stages as outlined below. Firstly, “inviscid” contours were defined utilizing arbitrary (but smoothly varying) functions in the subsonic and throat regions and the method of characteristics in the supersonic regions (downstream of the throats). These calculations were performed previously by Dr. A.D. Cutler and will not be discussed further. Secondly, the boundary layers were calculated<sup>19</sup> and the inviscid contours were corrected for the displacement effect of these. Thirdly, the middle contour was modified in the subsonic region and the inner contour was extended upstream, as dictated by structural and material requirements. Fourthly, the middle contour was truncated at the downstream end and the coflow and centerjet nozzle contours were aligned at the exit plane. (The results of these steps are shown in the previously described Figure 1 and Figure 2.) The final (fifth) step was to truncate/extend the outer contour. Steps 2 to 5 are described below.

The boundary layer computations were performed for each of the three surfaces



of the two nozzles (outer, middle and inner contours) using a code<sup>19</sup> which solves the “boundary layer equations”. These are a simplified set of the Navier-Stokes equations (solved directly by the SPARK FNS code<sup>20</sup> as described in section 5.0) which are valid only in the boundary layer. The boundary layer calculations assumed turbulent boundary layers throughout, an assumption that was justified on the following grounds: (i) No special efforts were employed to polish the surfaces (see Appendix A) or to ensure laminar boundary layers entering the nozzle; indeed the flow entering the inner nozzle contraction was nearly fully developed turbulent pipe flow. (ii) Turbulent boundary layer calculations yielded Reynolds numbers based on momentum thickness which were consistent with turbulent flow ( $Re_\theta$  about 1000 at the  $Re_\theta$  minimum located just upstream of the coflow nozzle throat for the outer and middle contours,  $Re_\theta = 510$  at the throat of the inner nozzle). These calculations require as input on the upstream conditions (which typically involve a statement that the boundary layer is thin) and a specification of the axial distribution of pressure at the edge of the boundary layer, results that are derived from calculations of inviscid, irrotational flow in the nozzles. (Inviscid flow calculations were performed as part of the nozzle “inviscid” contour design.) The code yields, among other things, profiles of Mach number at the exit station which are used later for comparison with computational fluid dynamics calculations (see Chapter 5 and Section 6.3), and the distributions of displacement thickness ( $\delta^*$ ), which are used to correct the nozzle contours for the displacement effect of the boundary layers. This correction is done either by adding or subtracting (addition for the outer and inner contours, subtraction for the middle contour)  $\delta^*$  at each axial location of the nozzle contour to or from the contour radius at that location. This modification consists essentially of enlarging the nozzle flow passages a small amount with respect to the original inviscid contours and will yield the final coordinates required to produce

the desired nozzle performance in viscous flow.

Several modifications were made to the contours calculated as described above in the subsonic regions. Since the “inviscid” contours were corrected with the displacement thickness (which varies in the streamwise direction) this led to contours which vary slowly in radius in regions in which the specified inviscid (i.e., uncorrected) contour radii were constant with axial distance. (This was the case for the upstream portion of the middle and inner contours.) For ease of manufacturing and since the contour shapes in these subsonic regions are not very important (provided the contours are smooth), these radii were again set constant. Furthermore, machining tolerances (which were very small in the supersonic regions - see Appendix A) were relaxed in the subsonic regions. Further adjustments were made to provide sufficient strength and rigidity of the centerbody. The inner nozzle was tapered (moving upstream) from a diameter of 0.781 inches (19.84 mm) to a diameter of 5/8 inch (15.87 mm) and the outside diameter of the centerbody was increased from a constant diameter of 1.147 inches (29.13 mm) to a constant diameter of 1.65 inches (41.91 mm). These two constant diameter regions were smoothly (continuous slope) joined by a region which was specified with a third order polynomial function.

The middle contour was truncated at the downstream (supersonic) end to increase the thickness of the lip between middle and inner contour at the exit plane and to reduce the thickness of the boundary layer at the end of the middle contour. (Note that the boundary layers on the middle and inner contours at the exit plane form the part of the initial condition for the mixing layer which develops between centerjet and the coflow, and they should ideally be thin.)

The outer contour was truncated at an axial location of 9.369 inches (237.98 mm) to afford the required optical and probe access near the centerjet nozzle exit. The truncation

point was well downstream of the point at an axial location of 8.86 inches (225 mm) where the final expansion wave is reflected from this surface and so was in the region of constant surface Mach number (equal to the exit Mach number). A static pressure tap was located in this region of constant surface Mach number, upstream of the truncation point at an axial location of 9.119 inches (231.63 mm). In order to extend the outer contour 0.719 inches (18.26 mm) further downstream when optical or pitot probe access is not required at the “exit” plane, an outer nozzle exit cone was manufactured to mate to the alignment rim of the outer nozzle exit lip. The interior diameter (which was constant) was matched to the outer nozzle contour at the truncation point; care was taken in the manufacture of this component to minimize the discontinuity in surface at the joint, and hence to minimize the disturbance to the flow. The purpose of the extension cone was to extend slightly downstream the point at which the free shear layer between the coflow jet and the ambient air was initiated. Since, for the present purpose (where we are interested mainly in the mixing between the centerjet and coflow) the useful region of the coflowing jet field is limited at the downstream end by the growth of this shear layer and also, to some degree, by waves generated from this shear layer, the extension cone in effect slightly increases the useful extent of the jet. The extension cone is tapered externally to provide a smooth merging of entrained ambient air and the coflow jet at the nozzle exit.

### 3.2 MODEL ASSEMBLY

In moving from the specification of the nozzle contours to the mechanical design, various issues in addition to nozzle performance, particularly structural integrity of the model under the expected pressure loadings were considered. The various components (shown in Figure 3 through Figure 6), their assembly (shown in Figure 7), and some of these mechanical design issues are discussed in this section. Manufacturing issues are discussed and detailed machine drawings presented in Appendix A. Many aspects of mechanical design were carefully considered both to ensure the structural integrity of the model itself under extreme pressure loading conditions as well as to obtain the required nozzle performance. As shown in the aforementioned figures, the coannular jet nozzle consists of the following components (proceeding from the bottom to the top): transverse jet facility adaptor flange, centerbody, support flange, centerbody, and coflow nozzle body. The full assembly mounts directly to the top of the transverse jet facility plenum chamber and is approximately 18 inches wide and 15 inches tall.

The adaptor flange as shown in Figure 3 is an existing transverse jet facility component which was modified for this application. It is solid steel, 18 inches in diameter and nearly 2 inches (50.8 mm) thick, designed to facilitate easy mounting of the following experimental model components atop the transverse jet facility plenum. The main modification required for its implementation into the new facility was a provision for a 0.5 inch high pressure line to supply the inner nozzle with helium. This is accomplished with the installation of a connecting steel tube fitted to the rear flange face inside the plenum and spanning the plenum pressure chamber. This steel tubing lies in the path of the nozzle coflow high pressure air supply. However, the flow velocity is low subsonic in this region and far upstream of the coflow sonic throat and consequently the disturbance of the coflow is minimal.

The helium flow, in moving through the steel tubing, turns around several corners which may introduce unwanted vorticity to the flow. Thus an installation of in-line flow straightener (shown in Figure 7) is placed downstream of the final bend in the supply line. It is composed of a seven hole steel insert (resembling a honeycomb structure which has been shown to be an effective means of breaking up and removing vorticity from a fluid flow) through which the helium flow must pass before entering into the inner nozzle. The total area of these honeycomb passages is roughly equal to that of the inner nozzle sonic throat and the Mach number in this region is significantly high as well. The velocity in this flow straightener will, however, never reach sonic conditions since the total pressure here is higher than at the inner nozzle throat due to large losses in total pressure in this component. The insert is located in a pipe fitting which connects the 0.5 inch steel tubing to the entrance passage of the centerbody.

On top of this component is mounted the support flange shown in Figure 4 which secures the centerbody. This is perhaps the most crucial component from a structural strength standpoint in that the coflow nozzle performance is dependent upon the centered location of the centerbody with respect to the inner wall contour of the outer contour. In order for a uniform flow field to be achieved, a paramount design criterion was to achieve and maintain an axisymmetric flowfield throughout the nozzle passages. The concentricity of the nozzle is determined by the structural stiffness of the centerbody nozzle itself and the support struts of the support flange which hold the centerbody nozzle in place (see Figure 4 and Figure 5). In order to manufacture this support flange, three wedge-shaped sections of material are removed from the original solid component. The struts are tapered to sharp edges at both upstream and downstream ends.

Maximum allowable operating deflections for the inner nozzle contour surface with respect to those of the outer were imposed in addition to stringent machining tolerancing in order

to maintain the concentricity of the outer and inner nozzles during facility running. It was hypothesized that the most extreme nozzle loading condition achievable during facility operation would result in a significant moment being applied to only one side of the centerjet nozzle tip - a condition which was modeled by the application of a 60 lb. force applied near the tip of a cantilever tube. In order to achieve maximum structural rigidity, key structural components such as this centerbody as well as the support flange described below are constructed of 15-5 stainless steel, heat treated to a T4 hardness condition. The centerbody itself is modeled as a pipe of uniform crosssection and thus the maximum permissible length ( $l$ ) of this rod is determined by specifying a maximum permissible deflection ( $\delta$ ) of this rod under the aforementioned loading condition of 2.5/1000 inch. Similarly, by estimating the dimensions of a single support strut, the corresponding deflection ( $\theta$ ) at the tip due to the applied load is obtained. Thus the support flange structure as designed is triple redundant as three of these interconnected support struts are used to form the support flange. In these equations  $I$  is the moment of inertia<sup>21</sup>,  $W$  the applied load (force),  $E$  the modulus of elasticity of the component material, and  $M$  is the applied couple (force-length).

$$\delta = \frac{Wl^3}{3EI} \qquad \theta = \frac{Ml}{EI}$$

The internal passage of the centerbody “body” is tapered out to a slightly larger internal diameter downstream of the portion which slides into the support flange (the critical structural region requiring additional wall thickness for added strength) in order to match the diameter of the second piece of the centerbody (the centerbody “head”). Within the internal passage of the centerbody “head” (approximately three inches in length) is located the contracting flow passage leading to the centerjet throat. The outer surface of the centerbody, together with the inner surface of the coflow nozzle outer body form the coflow passage, with its annular sonic throat located at

the maximum diameter of the centerbody head, upstream of centerjet sonic throat location.

In assembling the complete apparatus (shown in Figure 7), the centerbody support flange is fitted with an O-ring on its lower face and seated onto the transverse jet facility adaptor flange. Next a second O-ring is placed on the upper face of the centerbody support flange and the coflow nozzle body is seated onto the support flange. The centerbody is then lowered down through the outer nozzle opening into place in the support flange collar as shown in Figure 6 and is secured to the support flange which centers it by a locking nut.

The assembly is then aligned through the use of a circumferential micrometer and is checked for concentricity throughout the uniform securing of the components in order to maintain a maximum radial variation of 0.001 inch. The centerbody nozzle is then connected to the adaptor flange with a stainless steel tubing and the assembly lowered onto the transverse jet facility plenum chamber as one component. After securing the nozzle assembly and connecting the helium supply line, pressure taps and relevant instrumentation, assembly is complete.

Provisions were made for attaching test apparatus. The exterior surface of the outer nozzle was finished with opposed parallel mounting flats to which the stepper motor assembly used to survey the nozzle exit flow was attached. Alternatively these surfaces could be utilized to mount additional support structures, optical equipment or even hoisting provisions for moving the model itself into place. An extension cone is secured directly to the outer nozzle lip with its constant inner diameter matched exactly to that of the coflow nozzle main body. Longer extension pieces could be substituted in the future, if required.

## **4.0 EXPERIMENTAL METHOD**

### **4.1 TEST FACILITY AND PROCEDURE**

The Transverse Jet Facility used to conduct the experimental portions of this test is located in building 1221C of the NASA Langley Research Center in Hampton, Virginia. This facility is a resource of the Langley's Hypersonic Airbreathing Propulsion Branch and is shown in its current configuration (with the coannular nozzle installed) in Figure 8. It is an open jet blowdown facility based around a high pressure plenum, 3.5 feet (1.167 m) tall and 15.75 inches (0.400 m) in internal diameter. Atop this plenum chamber is mounted the coannular nozzle which was designed and fabricated as part of the present experimental work. The plenum chamber which supplies the test nozzle coflow is fed by a 600 psia (4.14 MPa) supply line of compressed nominally ambient temperature air. A single "Rigimesh" plate along with four wire mesh screen is installed in the Transverse Jet Facility plenum chamber to eliminate large acoustical disturbances and nonuniformities from the plenum chamber air supply (i.e., any swirl or vorticity which may be present) and produce a minimally distorted air flow at the test model coflow nozzle entrance. This plate is composed of several layers of fine metal screen material sintered together and rolled to form a rigid semi-porous plate, resulting in a substantial pressure drop on the order of 50 psi (345 kPa) during facility operation.

The nozzle centerjet was run utilizing air (used most often due to its essentially limitless supply) or helium (used sparingly). The facility helium resource is a field of twelve 'K' bottles linked together in series to produce a combined pressure of up to 2700 psia depending on bottle size and fill levels (as well as helium temperature) and with a volumetric capacity of



approximately 200 SCF per bottle. At the design operating pressure, this helium reserve could easily be exhausted in 3 minutes. In order to maintain some measure of logistic feasibility several data sets must be collected with one bottle field supply. A minimum of 10 to 20 seconds of run time is required for a single survey in order to establish the helium flow (that is to bring the helium supply on line and stabilize the helium at the required pressure). Once this procedure has been carried out the actual data acquisition may be initiated, a task which typically takes an additional 30-40 seconds per pitot survey. This translates into a minimum required run time of around 45 seconds - a mere 4 helium runs may be obtained from a full supply of helium before the entire bottle field must be replaced.

In order to effectively monitor the performance of the Transverse Jet Facility during its operation it is instrumented with pressure taps in a variety of key locations. Pressure taps are placed immediately upstream and downstream of the regimesh located in the facility plenum. The purpose of these taps is to monitor the plenum pressure downstream of the screens and the pressure drop across the Rigimesh. A type K thermocouple is used to monitor the facility plenum air temperature upstream of the Rigimesh plate and screen assembly described as well as the centerjet supply line temperature at its attachment point to the aforementioned adaptor flange fitting. The model itself has two additional static pressure taps and one additional type K thermocouple used to monitor normal facility operation as well. One of the static pressure taps is located at the exit of the nozzle coflow, just downstream of the point at which the Mach number reaches its final value. This value should be that of atmospheric pressure if the pressure is properly set. This static pressure tap is an 0.008 inch (0.20 mm) diameter orifice placed 0.5 inches (12.7mm) from the nozzle exit plane. It is located equidistant between the nozzle exit (without the extension cap installed) and the reflection point of the aforementioned terminating Mach wave of

the nozzle coflow. The second model pressure tap is used to monitor the centerjet flow as well. This tap is placed just downstream of the honeycomb flow straightener discussed previously and is used to set the inner nozzle operating pressure.

Facility operating conditions were as follows. The nominal stagnation pressure of the coflow, measured at the plenum pressure tap, was calculated to be 84.4 psia (582 kPa) by assuming isentropic flow of a calorically perfect gas ( $\gamma=1.4$ ) to an exit Mach number of 1.8 and an exit static pressure of 1 atmosphere (101.3 kPa). Actual operating conditions were held in the range 580 kPa to 584 kPa. The nominal pressure at the centerjet pressure tap was calculated to be 73.4 psia (506 kPa) for air as the centerjet gas and 90.6 psia (625 kPa) for helium. Actual operating pressures were held in the range 505 kPa to 507 kPa for air and 624 kPa to 626 kPa for helium. It should however be noted that this is not the inner nozzle stagnation pressure since the flow is not at rest but rather moving at a comparatively low flow velocity of approximately 0.16 Mach.

These calculations, which assumed quasi-1-D isentropic flow of a calorically perfect gas, firstly required specification of the centerjet nozzle throat area (from the known geometry) to calculate exit area given the design gas composition ( $\gamma=1.645$ ) and design Mach number (1.8):

where

$$\frac{A_{throat}}{A_e} = \left(\frac{\gamma+1}{2}\right)^{\frac{\gamma+1}{2 \cdot (\gamma-1)}} \cdot M \cdot \left(1 + \frac{\gamma-1}{2} \cdot M^2\right)^{-\frac{\gamma+1}{2 \cdot (\gamma-1)}}$$

Secondly, the exit Mach number was calculated given this area ratio and the actual centerjet gas composition (either helium with  $\gamma=1.667$  or air with  $\gamma=1.4$ ) using the same equation. Note for future reference that the calculated exit Mach number was 1.721 for air centerjet gas and 1.807 for

helium. Thirdly, the Mach number at the centerjet pressure tap was calculated given the area of the passage just downstream of the static tap (5/8 inch diameter), the throat area, and the gas composition. Fourthly, the pressure at the centerjet pressure tap was calculated given the Mach number at the pressure tap, the exit Mach number, the gas composition, and an exit static pressure of 1 atmosphere (101.3 kPa):

$$p_{tap} = \frac{p}{p_t}(M_{tap}) \cdot p_t$$

where

$$p_t = \left\{ \frac{p}{p_t}(M_e) \right\}^{-1} 101.3 kPa$$

and

$$\frac{p}{p_t} = \left( 1 + \frac{\gamma-1}{2} \cdot M^2 \right)^{-\frac{\gamma}{(\gamma-1)}}$$

The pressures and temperatures were monitored during facility operation with National Instruments LABVIEW data acquisition software<sup>22,23</sup> for PC, tailored to this particular experiment and facility. This system was originally developed by J. Quinn<sup>24</sup> for other experimental projects and was modified for use in the current work. Pressure data were collected using pressure transducers chosen appropriately for specific operational ranges and calibrated using the same LABVIEW data acquisition system. The transducers themselves produce voltages of a few millivolts corresponding to a given range of calibrated pressures. In order then to convert a voltage to a pressure reading, the transducer is first calibrated by applying a known pressure to

a least squares fit to a linear function is performed. These voltage readings are collected by a model AT-MIO-E216E data acquisition board and passed through an AMUX-64T multiplexer board which repeatedly scans a given block of data channels for voltages levels and passes the data on to the LABVIEW computer application. The LABVIEW subroutine responsible for collecting, converting and reporting relevant pressure levels scans from the designated AMUX - 64T channels at a rate of 2500 Hz. These continuously updated transducer pressure readings are subsequently converted to pressure readings as described above and then reported to the LABVIEW virtual control panel. It is with this control panel that the facility performance is monitored "real time" during operation. These readings are then written to data files for post-processing and analysis.

## 4.2 PITOT SURVEYS

The primary data collection tool employed in this experiment was a pitot probe specially designed to have high spatial resolution in order to accurately resolve the mixing layer region between centerjet and coflow. (The mixing layer is a region of steep pitot pressure gradients, especially near the nozzle exit.) In order to achieve this high resolution, the probe tip was manufactured utilizing a hypodermic needle 0.010 inches (0.254 mm) in inside diameter and 0.020 inches (0.508 mm) in outside diameter, which was cut to a length of 0.175 inches (4.44 mm) and ground square at the ends. This needle was brazed into a hole on the axis of a machined stainless steel cone which was in turn brazed into a length of standard 1/8 inch (3.18 mm) stainless steel tube. The solid material of the probe lay within a 10 degree semi-vertex angle cone drawn from the tip, which was sufficiently small to ensure that the shock wave generated by the probe lay very close to the tip for Mach numbers greater than about 1.05. This precaution ensures that the probe measures pitot pressure (defined as the total pressure behind a normal shock) at the location in the flow of the probe tip, as required. One disadvantage of this small tip diameter is that it can lead to a long probe/connecting-tubing/transducer instrument response time. This is because, as the probe responds to a change in pitot pressure at the tip, there is a settling time required until the pressure in the tubing which leads to the pressure transducer, and in the transducer itself, is in equilibrium with the pressure at the tip. Since the probe tip is so small, precautions were taken minimize the tubing/transducer internal volume by making the length of tubing between the pitot probe and the transducer as short as possible and choosing relatively small internal diameter tubing. The probe response time determines the time the probe must dwell at each point in the flow at which data is to be taken before this data can be acquired - if the dwell time is too short the probe does not make an accurate measurement. On

the other hand, it is important that the dwell time not be too long given the limited helium supplies and the necessity of obtaining sufficient data points to resolve the steep pitot pressure gradients in the mixing layer. Thus it was necessary to accurately determine the response time of the probe. The probe response time was obtained in an experiment in which the pitot probe was moved rapidly into the centerjet, which was operated at design conditions (but with no coflow), and a pressure time history was obtained.

As discussed in Section 4.1, all data were acquired using a personal computer running LABVIEW software. A specialized probe calibration LABVIEW routine was written to determine the response time of the probe. It collects pressure readings at a specified sample rate from the probe pressure transducer and these readings are then both displayed to the virtual control panel as well as written to a data file. The calibration procedure involved triggering said data acquisition routine and then directing the primary stepper motor to move into the supersonic jet as rapidly as possible. Minimizing the time which the motor requires to move the probe across the nozzle mixing layer and into the uniform flow of the nozzle core was crucial since during this time the pitot pressure level being measured is not constant but rather changing. In order to minimize the time which the probe tip spends in the mixing layer, the probe is mounted only 3-4 mm above the inner jet exit plane (the first survey plane) where the jet mixing layer is relatively thin. The probe is traversed from a distance of 0.50 inches (12.7 mm) outside the region of jet influence into the uniform core of the jet. The motor is accelerated to its traversing velocity essentially instantaneously (394 inches per second squared) and traverses the prescribed distance at a velocity of 11.81 inches (300 mm) per second. The period of time which the probe spends in the shear layer is approximately 0.00667 seconds as it traverses into the supersonic jet. In contrast, the response time measured by establishing the time required for the probe to move from

one constant pressure value outside the jet to another higher pressure value inside the jet (or vice versa) is 0.4 seconds as illustrated in Figure 9. The entire traversing motion of the pitot probe into the jet takes only 0.0434 seconds, an order of magnitude less than the measured probe response time.

During data acquisition the pitot probe is secured in a slot of an existing probe survey rake and is shown in its current experimental configuration in Figure 10. The probe rake as well as much of the stepper motor probe traverse mounting hardware was developed by C. Johnson<sup>25</sup> for an earlier experimental application. This probe rake was designed to accommodate four survey probes in a stainless steel, two dimensional airfoil-like housing. It was manufactured with leading and trailing edges tapered to a sharp edge to minimize flow disturbance. Near the top of the rake are three slots into which small survey probes such as the pitot probe described above may be secured. Probe interchange is accomplished by removing a flush side panel shape and feeding the probe pressure tubing (and/or signal wire if required) down through the body of the probe rake. When the side panel is replaced and tightened the probes are pressed tightly and centered in the slots inside the rake and secured for use. A fourth probe is permanently affixed to the probe rake and also protrudes from the rake leading edge. Its purpose in the past was as a sample collecting probe for gas concentration measurements - however the gas analyzer was not available at the time of this experiment and hence gas sampling was not employed in the nozzle surveys. The pitot probe was situated in the first probe slot, the other two slots and the gas sampling probe remained unused. This entire surveying rake was attached directly to the smaller of two stepping motor driven translation stages, which was manufactured by Klinger and is shown in Figure 11. This translation stage traverses more slowly and is hence used not as the primary sweeping axis but rather to advance the rake to the position of the next survey.

The Klinger translation stage mounts directly on top of the second, larger translation stage manufactured by Compumotor, which was in turn secured via a mounting bracket and mounting plate to the model. Two different mounting plates, both one inch in thickness and constructed of aluminum were used during the completion of the test matrix. One such plate was used to mount the pitot probe tip 3-4 millimeters from the lip of the center jet nozzle (which protrudes beyond the lip of the coflow jet nozzle by several millimeters if the outer jet exit cone is removed). In order to survey the jet at varying heights, provisions were made in the design of the second mounting plate to facilitate a somewhat simplified relocation of the probe traverse assembly. This was accomplished by machining vertical slotted bolt holes through the mounting plate. In order to move the traversing hardware from one configuration to another, one need only place a leveling bar of some kind at the assembly's current position and relocate the assembly (after loosening its securing bolts) by placing a spacing plate of appropriate thickness between the relocated assembly and the leveling bar. The assembly is then re-secured and final alignment and height adjustment is accomplished through the use of specially designed alignment tools which mount securely atop the outer nozzle lip.

The aluminum alignment tools described in Appendix A serve both to verify location of the pitot probe tip a given distance above the inner nozzle lip as well as to center the probe tip over the nozzle itself. In this way the probe is zeroed with respect to the nozzle centerline each time a survey is taken at a new height.

Using this method of relocating and leveling the probe translation mechanism, surveys were collected at probe tip heights ranging from 13 to 163 mm above the inner nozzle lip. Additional survey heights were achieved by bolting extension plates to the probe mounting assembly thus extending the potential survey height to nearly 253 mm above the inner nozzle lip



although only surveys up to 243 mm are included here.

The nozzle was designed and manufactured with great care so as to be axisymmetric, and thus, it was expected that the coannular flow would also be axisymmetric. This allows data acquired to be limited to surveys across the diameter of the flow, i.e., from one edge of the coflow to the other. The existence of symmetry was checked by observing the symmetry (left versus right side) of these surveys.

The typical survey routine involved using the aforementioned alignment tools to manually position the probe tip over the center of the jet. Once the probe was positioned (with the stepper motors powered off) the surveying stepper motor was powered on and an initialization LABVIEW program was run. In addition, a 'start' command was sent to the stepper motor to conduct a practice survey of the nozzle exit plane. Following the practice survey's successful execution the probe was returned to its standby position - 1.25 inches from the centerline of the nozzle exit plane - in preparation for facility start-up. At this point a second LABVIEW program specific to the type of probe survey to be taken (either 0.7, 1.1, or 2.5 inches in diameter) was loaded and run. Once the facility was started, and the inner and outer jet flow conditions allowed to settle, another 'start' command is given to the motor which immediately moves the probe to the appropriate starting position for any one of three potential probe survey routines (described below). The survey is executed over the specified diameter in a given number of steps, and following the completion of the pitot survey, the probe is returned to its original standby position.

Different survey ranges were performed across the coannular nozzle diameter at various axial positions above the nozzle exit plane. Surveys of 100 points were collected over three regions of the flow - the entire coannular jet, the center 0.7 inches (17.78 mm) of the jet and of the center 1.1 inches (27.94 mm) of the jet with both helium and air as the centerjet gas. The

0.7 inch survey allows a high density of points over the centerjet - about one point every 0.00769 inches (0.195 mm) and was utilized exclusively in surveying the exit plane. Note that the outside diameter of the pitot probe is 0.020 inch (0.508 mm) which in essence fixes the spatial resolution of our measurement. The 1.1 inch (27.94 mm) survey brackets the centerjet at downstream locations where the centerjet has spread to a somewhat larger diameter and makes it possible to capture weak shock waves emanating from the nozzle lips as well as the flow features of the centerjet itself in the nearfield.

In addition, 400 point surveys were collected of the entire coannular jet with air as the centerjet gas (supplies of helium were limited) to characterize the development of the coflow and the mixing layer between the coflow and the ambient air rather than to examine the mixing of the centerjet. They provided information as to the location of Mach and expansion waves within the coflow at the various downstream locations as well as a detailed (400 point) picture of the entire flow field - approximately 160 points per inch (6.30 points per mm) or one point every 0.00625 inches (0.159 mm). In the cases of the final two survey heights of 200mm and 240 mm, only two different surveys (omitting the 0.7 inch survey) were made.

### 4.3 FOCUSING SCHLIEREN

Flow visualization of the coannular nozzle flow was obtained through the use of a focusing schlieren system. The system implemented here (shown in Figure 12) is based on the work of L. Weinstein<sup>26</sup> and was developed by J. Quinn<sup>24</sup>. The basic idea behind a schlieren system is that some of the light emanating from a single finite thickness line source in the case of a conventional schlieren, or an array of finite thickness line sources in the case of the focusing schlieren, is deflected as it passes through the flowfield of interest and is blocked by a “knife edge” (or an array of knife edges if an array of sources is employed) before it reaches the imaging plane. Thus certain parts of the field through which this light has passed appear darker than others dependent upon the amount of deflection the rays undergo within the flow field as they encounter flow structures (such as shock and expansion waves, etc.). Utilizing this technique, variations in the first derivative of the light path length integral of refractive index are displayed in the field of view. In contrast, techniques such as shadowgraph display an image corresponding to the second derivative of the light path length integral of refractive index and interferometry techniques display fringe patterns whose location may be related directly to the light path length integral of refractive index<sup>27</sup>.

In a flow of constant composition the refractive index  $n$  is proportional to the density as expressed below, where  $c$  is the Gladstone-Dale constant, and so the schlieren image may be taken as a measure of density gradient:

$$n - 1 = c_\rho$$

For a mixture of chemical species (rather than a pure species for which the above expression strictly holds), the refractive index is expressed as a weighted sum, as shown below. Here the

subscript  $i$  refers to the  $i^{\text{th}}$  species and  $\rho_i$  is the species partial density.

$$n - 1 = \sum_i c_i \rho_i$$

In the case of a flow of differing composition such as our mixing flow of helium and air (with indices of refraction of 1.000036 and 1.0002926 respectively at 273.15 K, 101325 Pa and 589 nm wavelength light<sup>28</sup>), the schlieren image no longer provides a direct measure of density gradient. However, since  $(n-1)$  is much less under these reference conditions for helium than for air (as is its molecular weight) schlieren still gives a qualitative indication of density gradient.

The first element of the system (shown in Figure 12) is a strobe light source (pulse length  $\sim 1 \mu\text{sec.}$ ). Light from the strobe is passed through a diffuser (actually a pair of Fresnel lenses) and an array of sources is created as the light emanating from the single light source is broken into a planar distribution of smaller sources, one from each slit of the source grid. The light from the source grid passes through the coannular jet (where it is deflected as it encounters refractive index gradients) and onto the focusing schlieren lens which focuses an image of the source grid onto the cutoff grid. Light which is passed by the cutoff grid forms an image of the coannular jet at the image plane. This image is then photographed by the digital camera system. A diffuser and fresnel lens are located at the image plane, the purpose of the latter being simply to increase the brightness of the image formed within the digital camera (i.e., formed by the lens of the camera at the camera image or detector plane).

The cutoff grid is “shot” by placing a sheet of unexposed film (Kodak Ultratech) at the location of the image of the source grid formed by the focusing schlieren lens (with the room lights out, of course). By pulsing the strobe (seven high intensity pulses was found to be the optimum number) a sharp negative image of the source grid is captured on the now exposed film

sheet. The exposed film is developed and the developed cutoff grid is replaced in the precise position in which it was “shot” with the assistance of alignment pin holes punched through the side of the film sheet. The cutoff grid is a negative of the source grid which may at this time be offset by a small amount in order to allow part of the light to pass as described above.

A Photometrics Ltd. AT200 digital CCD camera<sup>29</sup> interfacing with a personal computer through the PMIS software package<sup>30</sup> with a Nikon camera lens of F number 1.8 and a 50mm focal length is used for image collection. The digitized images contain up to 15 bit data (32,768 gray levels) digitized at 40000 pixels per second. The CCD array itself is composed of a 512x512 pixel field binned 2x2 thus yielding a 256x256 pixel image. The term binning refers to the combination of charge levels in adjacent pixels. The entire schlieren optical system including the camera was mounted on a traversing rail system, consisting of a single mounting rail 6 feet in length, in order to maintain consistent alignment of all components. This rail was secured to a large vertical axis stepping motor driven translation stage which could be used to remotely traverse the schlieren system.

## 5.0 COMPUTATIONAL ANALYSIS

### 5.1 AXISYMMETRIC COMPUTATIONAL CODE

The computational code used in this research is one of the SPARK family of reacting flow solvers<sup>20</sup>. This code has existed in several different forms including 2-D and 3-D versions as well as its present axisymmetric form - an extension of the 2-D case. It solves the 2-D Navier Stokes and species conservation equations governing multi-species chemically reacting flows. The code is extremely versatile and possesses many options as to the computational configuration in which it is run. SPARK is used to calculate parameters of the centerjet and coflow nozzle flow, including contours of Mach number and static pressure as well as exit plane profiles of Mach number, velocity, and pitot pressure. The code also has provisions to specify individual flow compositions (on a per mass basis) of both the coflow and centerjet fluids.

The code was run in both its viscous and inviscid forms during different stages of the research. In particular, the inviscid form was used during the initial computations in order to minimize run times. This version was employed as well during development of other aspects of the code, namely implementation of a specialized geometry and corresponding grid specification. Once these issues had been resolved, the final computations were run in the full viscous form. As the flow to be studied is non-reacting, no kinetic model was utilized.

The temporal integration of the code is second order accurate with an explicit formulation of the hydrodynamic terms. This includes a time accurate integration option which was used initially to implement and develop the code. A local time stepping option was chosen to run the test cases in order to speed convergence. By employing a local time stepping the solution

was allowed to progress to a steady state solution at the maximum local timestep at each respective gridpoint, thus greatly speeding convergence. Although not employed in this solution, it should be noted that the code also has provisions for explicit and implicit formulation of chemical temporal integration as well. In addition, several spatial discretization options exist as well including a second order MacCormack scheme, a fourth order Gottlieb scheme, a fourth order cross-MacCormack and a 4th order viscous MacCormack scheme used in the code's present form.

## **5.2 CODE MODIFICATIONS**

Modifications were made to the aforementioned code in order to most efficiently solve the current computational problem. Several of these modifications involve specializing the code to the particular geometry and nozzle boundary conditions. SPARK was initially run in a basic configuration - no turbulence model and 2-D planar as opposed to the actual 2-D axisymmetric nozzle geometry - to ensure sufficient grid distribution and resolution. A key feature of the code is its ability to cluster points in both dimensions as required to adequately resolve regions of particular interest. Such regions in the present case include the boundary layers forming along the contour walls, the axisymmetric centerline and most importantly both the centerbody nozzle and coflow nozzle sonic throat regions. The aforementioned flow areas consist of high gradient levels and hence are burdened with satisfying more strict resolution criteria. In particular, the transonic throat regions encompass subsonic, sonic and supersonic fluid flow regimes, all of which are solved over a single computational grid.

As stated previously, the centerjet nozzle is formed by the inner nozzle contour alone

(generated as a body of revolution about the nozzle centerline). By invoking the flow symmetry condition along the nozzle centerline we effectively halve the computational domain (no matter at this point whether the code is in its 2D planar or 2D axisymmetric configuration). Based on symmetry conditions, the streamwise 'U' velocity component, temperature and pressure are extrapolated to the centerline from the adjacent cell while the transverse (radial in the axisymmetric case) 'V' component is taken to be zero. Along the centerjet nozzle wall the no-slip condition is imposed, i.e., both the 'U' and 'V' velocity components are set to zero. Viscosity effects are present in the solution as a boundary layer grows along the physical nozzle contours resulting from the no-slip condition imposed along the contour surfaces. The same wall conditions are imposed for both wall surfaces of the coflow nozzle.

For both centerjet and coflow nozzle cases the exit plane outflow boundary is extrapolated from the two previous lines of grid points using a second order accurate approximation. Also for both geometries, the subsonic inflow boundary conditions are set by first specifying total temperature, total pressure and flow angle. The static pressure is calculated from

$$\frac{dp}{dx} = 0$$

The static temperature is obtained from the expression

$$T = T_t \cdot \left( \frac{p_t}{p} \right)^{\left( \frac{1-\gamma}{\gamma} \right)}$$

The Mach number is then determined using

$$M = \sqrt{\left( \frac{2}{(\gamma-1)} \right) \cdot \left( \left( \frac{T_t}{T} \right) - 1 \right)}$$

Finally, the streamwise velocity is determined from



$$u = a_o \cdot M$$

Similarly, taking  $\theta$  to be flow angle (which is set to be zero in the current case), the corresponding transverse velocity is found from

$$v = u \cdot \tan(\theta)$$

The three contours which defined the coflow and centerjet nozzles (the outer, middle and inner contours) were provided from the design as a series of discrete points. In order to facilitate the aforementioned clustering of grid points without altering the spacing of the physical nozzle contour points (or limiting the number of grid points used), the contours themselves need to be functionally specified. Three IMSL (International Math and Science Library) subroutines were enlisted to apply cubic splines to the contour points. The first of these three routines - CSAKM- computes a cubic spline interpolant to a set of data points (the array of surface points). The routine generates a matrix of cubic polynomial coefficients which is read by two other computational routines - CSVAL and CSDER - to evaluate the cubic splines and their derivatives respectively. In this way piecewise polynomials are constructed over the entire length of each contour which are then evaluated at the computational grid point axial location and return the corresponding surface point radial location.

Figure 13 and Figure 14 illustrate the final grid spacings of 201X51 used through the coflow computational domain and the 201X25 employed in the considerably smaller core flow domain. Gridpoints were clustered in the flow regions of highest gradient as mentioned previously, including the inner and outer sonic throats in the axial direction as well as the boundary layer and centerline regions in the radial direction (as shown in Figure 14).

## 6.0 RESULTS

### 6.1 CFD NOZZLE DESIGN VALIDATION

The SPARK two-dimensional axisymmetric Navier-Stokes flow solver was used to carry out preliminary design validation of the viscous nozzle flow contours discussed previously. The resulting computational solutions predict excellent nozzle performance when employing these viscous corrected nozzle profiles. Contour plots of Mach number variation through the nozzle as well as in the near throat region are shown in Figure 15 and Figure 16, respectively, and contour plots of pressure are shown in Figure 17 and Figure 18; plots of computations are presented for the helium centerjet gas case only. The Mach number and pressure can be seen to vary smoothly through both centerjet and coflow nozzle (with no sign of shock waves) and the nozzles appear to produce uniform parallel flows at the exit plane. (Recall that the exit plane coincides with the exit of the centerjet nozzle and lies downstream of the coflow nozzle junction with the extension cone but upstream of the end of the extension cone.)

Figure 19 and Figure 20 show plots of the centerjet and coflow exit plane Mach number. The Mach number decreases in the coflow from about 1.815 at a radial position of about 0.016 m to about 1.77 at 0.008 m. This condition arises due to the truncation of the middle contour (as discussed in Section 3.1) which results in the region of uniform parallel flow not reaching the downstream projection of the nozzle middle contour until a position beyond the exit plane. For radial position greater than about 0.016 m the coflow can be seen to be nearly uniform with a Mach number of 1.815, a little higher than the design Mach number of 1.8. The Mach number within the freestream of the centerjet lies between 1.82 and 1.835, again a bit higher than the

design Mach number. Part of this discrepancy in the calculation can be attributed to the use of helium in the centerjet rather than the gas used in the nozzle design (which was a mixture of 95% helium and 5% oxygen, with a gamma of 1.645 rather than 1.667). Recall from Section 4.1 that the isentropic, quasi-1-D calculation gave an exit Mach number of 1.807 for helium (a little higher than the design value but still less than the CFD calculated exit Mach number). Finally, note that the Mach number in the freestream of the centerjet is not quite as nearly uniform as that in the coflow at radial position greater than 0.016 m. This may be because the flow entering the centerjet nozzle, while it is low speed, is (turbulent) pipe flow and is therefore not irrotational as assumed in the design calculations.

In comparing the computational exit profiles calculated by the SPARK Navier-Stokes flow solver in the vicinity of the nozzle walls with the boundary layer profiles calculated utilizing the Harris boundary layer code, discrepancies are evident (as seen in Figure 21, Figure 22, and Figure 23). In general, the profiles determined by the SPARK code in the vicinities of the nozzle walls are more full than those determined by the Harris code, seemingly indicating an elevated effect of viscosity in the SPARK code (or reduced effect in the Harris code) but more probably stemming from insufficient grid resolution in the SPARK code. Currently there is about one grid point within the viscous sublayer in the SPARK computations, at least an order of magnitude fewer points than the number placed within this region in the Harris code computation. Recall however, that the purpose of the SPARK calculations was to validate the design calculations for the free stream flow, for which accurate calculations of the boundary layer were deemed unnecessary. The existing grid point resolution therefore strikes a reasonable balance between adequate resolution of the flow field as a whole and reasonable computer run times. However, Navier-Stokes calculations of the nozzle flows should be run in the future which do accurately

resolve the boundary layer since these will be required to provide the initial conditions for future calculations of the coannular jet flow (remember that the boundary layers on the nozzle inner and middle contours at the exit plane provide the inflow condition to the mixing layer between centerjet and coflow).

Finally, Figure 24 is included to illustrate the nature of the coannular flow being produced in the He / air configuration. Despite the matched Mach numbers between the two jets, a large mismatch in flow velocity is evident due primarily to the difference in molecular weights between the two gases (4.00 for helium as compared to 28.97 for air). It is the jets' velocities (or more correctly, the velocity difference between them) that drives the growth of the mixing layer.

## 6.2 SCHLIEREN IMAGES

Focusing schlieren images of the coannular jet flows are shown in Figures 25a and b. These images are each composites of four separate instantaneous overlapping images acquired at different heights above the nozzle exit plane at different times and later merged together. (Thus, the composite image may possibly give an incorrect impression of the period and repeatability of the large, coherent structures of the jet mixing layers or centerjet plume.) The image on the left (Figure 25a) is for the centerjet composed of air and the image on the right (Figure 25b) is for the centerjet composed of helium, but at nominally the same conditions of gas total temperature and jet exit pressure. Notice that the images are approximately antisymmetric about the axial centerline (dark and light regions are interchanged). This antisymmetry occurs because the schlieren source and cutoff grids are oriented vertically so as to be sensitive to horizontal gradients in density, and horizontal gradients in density are themselves antisymmetric about the axial centerline.

Consider first the case in which the centerjet gas is air (Figure 25a). Since the centerjet and coflow have the same composition and roughly the same Mach number at the exit plane, the exit velocities are nearly the same also. Since significant mixing requires a difference in velocity, this results in minimal mixing between the centerjet and coflow and in minimal spreading of the centerjet as a whole. The mixing which does occur, at least in the near field of the nozzle exit, occurs as a result of the wake of the centerbody lip, which in turn is influenced by the boundary layers on the inner and middle contour surfaces and the thickness of the lip at the nozzle exit plane. The mixing layer between coflow and stagnant surrounding air is initially thin but grows until at some point downstream it begins to influence the centerjet flow. In the downstream (top) part of the image the centerjet appears to become less distinct and its edges more irregular - this

may in part be due to the fact that the centerjet is viewed through the coflow so that the image of the centerjet region is also influenced by (instantaneous) horizontal density gradients in the coflow shear layer.

Consider now the case in which the centerjet gas is helium (Figure 25b). As was highlighted in Figure 24 (which showed the velocity distribution along a radius), the velocity difference between the centerjet and the coflow is very large with the helium centerjet. This leads to a much more rapid spread of the centerjet into the coflow than was observed with air. A quantitative discussion of mixing layer and plume growth rates obtained both from these images and from the pitot surveys will be presented in Section 6.3. Notice also that the much more distinct or “solid” appearance of the helium centerjet in Figure 25b as compared to the air centerjet in Figure 25a, which appears “washed out”. This difference in appearance occurs because the refractive index of the helium is low in relation to that of air, which leads to larger horizontal gradients in refractive index in going from the coflow (which is air) into the centerjet in the case where the centerjet is helium. Also, there appears to be little structure (shock waves or turbulent eddies) within the centerjet in the helium case, unlike with the air centerjet. This difference also occurs because of the low refractive index of the helium. For example, oblique shock waves propagating through the centerjet which produce a given pressure change will produce a much smaller refractive index change if the centerjet is helium than if the centerjet is air (recall that refractive index of a given gas is proportional to its density, which in turn is proportional to pressure), and thus will be much less visible.

Examining the schlieren images of Figure 25 more closely we are able to make out the system of waves (weak oblique shock waves or expansion fans) present. Moving radially inward from the outer edge of the coflow at the nozzle exit, the first set of waves encountered (only

faintly visible) emanate from the lip of the extension cone and occur as a result of the discontinuity in surface boundary condition there. The next outermost set of waves appear to originate from the seam where the coflow nozzle and the extension cone join (which in these images is not visible, obscured by the extension cone itself). A set of waves emanating from the same position is also visible in the close up schlieren images, which are shown in Figure 26 and Figure 27 (seemingly emanating from the lower corners of both images). These images were obtained with the coflow nozzle extension cone removed and afford an unobstructed view of the centerjet in the vicinity of the nozzle lip. The next set of waves encountered originate at the lip of the centerjet nozzle and may be seen more clearly in both Figure 26 and Figure 27. In these images the presence of the boundary layer on the walls of the centerbody nozzle can be clearly discerned as well as the merging of these boundary layers with the nozzle lip wake.

The flow physics which produce this wave structures emanating from the nozzle lip are illustrated in the cartoon of Figure 28. It can be seen to be not a simple case of nozzle over- or underexpansion but rather a result of the finite thickness of the centerjet lip. Expansion waves result as the flows turn the corners created by the finite thickness nozzle lip and oblique shocks emanate from the compression corners formed as the two flows merge and are turned back to their original direction. The duplicity of these flow structures is evident again in the schlieren images of Figure 26 and Figure 27. The seemingly abrupt variation in refractive index (and thus density) across a single one of these flow structures emanating from the nozzle lip (illustrated in Figure 28) indicate the presence of not one but two discrete and very different flow discontinuities.

### 6.3 PITOT PROBE SURVEYS

A complete series of pitot surveys to a maximum survey height of 243 millimeters above the centerjet nozzle exit are shown in Figure 29 through Figure 41. The results are presented in such a manner as to bring out several key aspects of the collected data sets. Plots are overlaid to demonstrate the repeatability of the nozzle contour surveys. In all cases - 400 point air surveys as well as various 100 point abbreviated surveys of both helium and air - identical behavior is shown at a particular survey height. (Obviously the detail in flow structure was improved with increased survey point density.) In addition, the symmetry of all surveys - both helium and air- about the nozzle centerline should also be noted (which justifies the acquisition of data along only a single diameter of the flow).

At the first survey location proceeding downstream, 3-4 mm from the centerjet nozzle exit plane, the pitot profiles distinctly show the coflow region, the wake of the centerbody (regions of low pitot pressure between the coflow and centerjet), and the centerjet. The pitot pressure is nearly uniform in the coflow whereas sharp positive and negative spikes can be observed in the centerjet and at the outer edge of the centerbody wake. These spikes can be attributed to the expansion waves and oblique shock waves emanating from the centerbody lip at the exit plane (see Figures 26 and 28). The pitot pressure is higher in the centerjet with helium than with air, as is expected based on isentropic, quasi-1-D calculations of the flow in the nozzle (see Section 4.1 and also upcoming discussions in relation to Figure 44). At the 13 mm and downstream heights various waves in the coflow region, previously discussed in connection with the schlieren images, can be observed in the pitot surveys as positive and negative spikes in an otherwise flat profile. The mixing layer between the jet and the coflow grows in width while the pitot pressure defect in the mixing layer falls. The growth is more



rapid with helium in the centerjet, so that by between 123 and 143 mm the mixing layer has completely eliminated the core (presumably pure centerjet gas) region of the centerjet.

Downstream of this point (the plume region) the pitot pressure at the jet axis falls rapidly. With air in the centerjet the core is probably still present at the most downstream station (243 mm). A negative spike in pitot pressure is observed on the axis of the centerjet at the 13 mm location (both helium and air cases) which tends to decrease in amplitude going downstream. It is believed that this spike is a result of the inward-propagating shock generated at the centerbody lip which focuses as it approaches the axis and turns normal at the axis itself. (A normal shock produces a much larger entropy rise and total pressure drop than a weak oblique shock.) Figures 42 and 43 are, respectively, compilations of all the 400 point air surveys and all the 100 point helium surveys, spaced according to their relative streamwise position to give a “perspective” view of the overall development of the two flow fields.

A comparison between the pitot profiles at the 3-4 mm downstream location with the CFD calculation of the flow at the nozzle exit plane (which had helium as the centerjet gas) is given in Figure 44. The pitot profiles are a sufficient distance downstream of the exit plane that the waves emanating from the centerbody lip have nearly reached the axis of the jet, resulting in the previously described spikes in the pitot pressure. However, the overall level of pitot pressure is roughly 13% too high in the experiment, which cannot be explained by the presence of these waves. The explanation appears simply to be that the centerjet total pressure was set (roughly 13%) higher than was intended. Recall that the total pressure was set by setting the pressure measured at the centerjet pressure tap to a value calculated to produce a nozzle exit pressure of 1 atmosphere. This calculation assumed uniform flow in the 5/8 inch internal passage in the centerbody, upstream of the centerjet nozzle throat, and isentropic quasi-1-D

flow. In fact, as seen in Figure 7, the centerjet pressure tap was located just downstream of the “flow straightener”, which consisted of a plug into which seven holes of diameter 0.125 inches had been drilled (see Appendix A). Significant pressure recovery took place downstream of this plug (and the pressure tap) as the (multiple) high (subsonic) speed jets discharging from the plug spread to uniformly fill the 5/8 inch diameter passage. This explanation has been verified in experimental work performed subsequent to the work described in this thesis, by S. Doerner. In this work the “flow straightener” was replaced by a pair of wire mesh screens installed in line with the 5/8 inch pipe and which produced little pressure rise downstream. Setting the centerjet pressure tap (now just downstream of the screens) to the calculated value resulted in pitot pressure profiles much closer to (within 1% of) the calculation. The unfortunate consequence of this “high” value of total pressure in the present work is that the centerjet exit (static) pressure is roughly 13% greater than the static pressure in the coflow (which is one atmosphere). This leads to stronger expansion waves and oblique shock waves emanating from the centerbody exit lip than would have been the case if the exit pressure had been matched. (Recall that one goal in the design of the experiment was to minimize the strength of such wave structures.)

In order to make a meaningful comparison of the results obtained in this experimental research with previous work, mixing layer and plume growth rates are estimated. As in the case of the CFD results presented earlier, only those results collected in the helium centerjet experimental cases are analysed in this way. Two separate pitot pressure reference levels, representative of typical coflow or centerjet values, are chosen. Datum levels are chosen at 95% of the reference pressure levels and as illustrated in Figure 45 and Figure 46 the intersections of these datum levels with nozzle pitot pressure profiles are obtained. The magnitude of the radial locations of these intersecting points, which are measures of the location of the edge of the mixing layer between the

centerjet and the coflow or (further downstream) the edge of the centerjet plume, are plotted as a function of axial distance in Figure 47. A nonlinear mixing layer growth region in the nearfield (composed of the first 4-5 heights) is seen to exhibit comparatively slower growth rate than those stations located further downstream. Also presented here is a plot of the magnitude of the difference in radial location between the inner and outer edges of the centerjet/coflow mixing layer, which is seen to increase with downstream location as expected. The magnitude of the radial locations of the edge of the mixing layer or plume at each side of the axis of the jet is averaged and the result is plotted in Figure 48. The magnitude of the difference in radial location between the inner and outer edge of the mixing layer are similarly averaged and plotted. Linear curve fits of both of these data sets are calculated and plotted in this figure. Also shown in Figure 48 is a straight line which is obtained from the helium focusing schlieren image shown in Figure 25b. Straight lines are drawn by "eye" which bound (intersect tangentially the outer turbulent flow structures of) the centerjet in the schlieren image, and the radius of the centerjet at any given axial distance is taken as the width measured horizontally by between these lines, divided by two. Good agreement is found between the line obtained from schlieren flow visualization and the data obtained from the pitot surveys.

In a 2-D (planar) mixing layer with zero streamwise pressure gradient, fully turbulent and starting from zero thickness it is expected that the growth rate of the mixing layer would be linear (see e.g. Ref. 3). However, in the present case, due to the influence of the boundary layers generated on the centerbody and the finite thickness of the lip, the mixing layer does not start from zero thickness. Furthermore, as the mixing layer grows to a thickness no longer small in relation to the radius of the centerjet, it becomes no longer 2-D planar in character. Notwithstanding these difficulties, the straight line fit to the mixing layer thickness data shown in

Figure 48 appears reasonable.

In the previous work mixing layer growth has been characterized by a normalized growth rate. The growth rate of a mixing layer (or jet) is defined as the change in mixing layer width (or jet radius) with respect to  $x$  location (the slopes of the plots in Figure 48). The normalized growth rate is defined as the experimental (compressible flow) growth rate normalized by an incompressible growth rate<sup>4</sup> which is calculated assuming identical velocity and density ratio using incompressible flow data correlations:

$$\frac{\frac{d\delta}{dx}}{\left. \frac{d\delta}{dx} \right|_{incompressible}} = \frac{\delta'}{\delta'_{incompressible}}$$

The convective Mach number is defined as the relative convection speed of the large scale structures in the shear layer to one of the free streams, normalized by speed of sound of this stream. This convection speed of large scale disturbances within the shear layer itself is computed using the expression<sup>6,7</sup>:

$$u_c = \frac{\left( u_1 + \sqrt{\frac{\rho_2}{\rho_1}} \cdot u_2 \right)}{\left( 1 + \sqrt{\frac{\rho_2}{\rho_1}} \right)}$$

in which  $\rho$ , and  $u$  are respectively the local density and velocity values in the coflow (subscript 1) or the centerjet (subscript 2). The resulting expressions for convective Mach number are:

$$M_{c_1} = \frac{(u_c - u_1)}{a_1} \quad \text{and} \quad M_{c_2} = \frac{(u_2 - u_c)}{a_2}$$

where  $a$  is the speed of sound.

The incompressible growth rate is given as computed from the expression<sup>6,7</sup>:

$$\delta'_{incompressible} = 0.17 \cdot \frac{\left(1 - \frac{u_2}{u_1}\right) \left(1 + \sqrt{\frac{\rho_2}{\rho_1}}\right)}{\left(1 + \frac{u_2}{u_1} \cdot \sqrt{\frac{\rho_2}{\rho_1}}\right)}$$

The quantities  $u_1$ ,  $u_2$ ,  $\rho_1$ ,  $\rho_2$  were calculated assuming isentropic, quasi-1D flow in the two nozzles (centerjet and coflow) and calorically perfect gases.  $M_{c1}$  and  $M_{c2}$  were calculated from these to be 0.787 and 0.859, respectively, for the helium centerjet case. Similarly,  $\delta'_{incompressible}$  was found to be 0.186.

The following equation is a 2-D correlation fit by Dimotakis to several of the “benchmark” jet growth rate data sets referenced in the literature, including that of Clemens and Mungal<sup>10</sup> as well as Papamoushou and Roshko<sup>7</sup>, both referenced previously:

$$\frac{\delta'}{\delta'_{incompressible}} = 0.2 + 0.8 \cdot e^{(-3 \cdot M_c^2)}$$

The general trend captured by this expression illustrates clearly that convective Mach number need not be very large for compressibility effects to be significant and that this growth rate tends to a value of about 0.2 as convective Mach number increases. Normalized growth rates for our data are plotted alongside the Dimotakis<sup>9</sup> curve for 2-D data in Figure 49. The mixing layer growth rate results agree well with the curve of Dimotakis, while the plume growth data fall lower. However, it should not be expected that the plume growth rate data would agree particularly well with the correlation of Dimotakis since the fundamental flow types differ (plume verses 2-D mixing layer) and the data have been normalized to an incompressible growth rate correlation valid only for 2-D mixing layers.

## 7.0 SUMMARY

Due to the extreme difficulty and expense associated with experimental scramjet engine testing, the development of computational tools capable of accurately predicting the flows in these engines is of great interest. An experiment is undertaken for the purpose of generating data in a simple axisymmetric, coannular, supersonic jet flow suitable for the validation of such codes. Experimental results include jet flow pitot pressure surveys and focusing schlieren images, however much of the thesis is concerned with the design and manufacture of the model. The experiment was run with pure air or pure helium in the centerjet, although the centerjet nozzle was designed for 95% He, 5% O<sub>2</sub> to facilitate non-intrusive (laser based) diagnostics. The SPARK two-dimensional axisymmetric Navier-Stokes flow solver was used to carry out preliminary design validation of the nozzle contours. The results of the calculations - used for later validation of experimental results- show a uniform exit plane flow, free of nonuniformities and disturbances.

Little or no shear exists between the centerjet and coflow for the air centerjet case. In the helium case however, the centerjet and coflow constituents are significantly different, resulting in a convective Mach number  $M_c = 0.82$ . The experimental nozzle flow was assumed to be axisymmetric; thus surveys were taken across the entire jet (through its centerline), from one edge of the coflow to the other, in order to exploit this inherent flow feature. This was subsequently investigated by comparing the symmetry of resulting exit jet profiles about the survey center.

It was found that the centerjet exit pressure was not matched to atmosphere and thus did not produce perfectly expanded exit flow as was intended, yielding stronger expansion and shock waves at the centerjet exit than anticipated. As seen by comparison of the centerjet He/air CFD exit profile and the experimental He/air exit plane survey profile, the overall level of pitot

pressure is higher (roughly 13%) in the experiment than was intended. This discrepancy cannot be explained by the presence of the weak oblique shocks observed emanating from the centerbody and coflow nozzle lips, but rather is attributed to a pressure rise occurring downstream of the flow straightener (and of the static pressure tap which monitored the centerjet supply gas pressure). The unfortunate consequence of this “high” value of total pressure is that the centerjet exit (static) pressure is greater than the static pressure in the coflow (1 atmosphere), generating stronger expansion waves and oblique shock waves emanating from the centerbody exit lip than would have been the case if the exit pressure had been matched.

Examining closely the schlieren images of the dissimilar He/air and air/air cases, we are able to make out the system of flow discontinuities present. The schlieren data are quantified by defining the slope of the edge of the jet. In order to meaningfully compare this flow visualization data with the pitot pressure surveys, mixing layer and centerjet growth rates are estimated. Datum levels are chosen at 95% of the reference pressure ratio levels and the intersections of these datum levels with a nozzle pitot pressure profiles at each survey station are recorded. Very good agreement is found between the averaged jet spreading data (obtained via the pitot pressure surveys) and that observed from schlieren flow visualization. The magnitude of the difference in radial location between the inner and outer edges of the centerjet/coflow mixing layer is seen to increase with downstream location from this data. A marked increase in spreading angle of the centerjet within the coflow can be observed in the far field, just as is to be expected on the basis of previous research conducted with similar experimental configurations. At the same downstream location the He jet appears to spread to an apparent diameter 50% greater than its air jet counterpart.

Comparison of these results with those obtained in previous experimental research is made

by establishing two separate reference pitot pressure ratio levels, representative of typical coflow or centerjet values. The near field spreading rate results agree well with prior findings, while the far field and schlieren data fall a bit lower. As the aforementioned existing data is intended to represent only normalized growth rates for mixing layers (and not jets or plumes), these results are to be expected.



## 8.0 APPENDIX A - MANUFACTURING DETAILS

The following Appendix presents the manufacturing and assembly details (and associated engineering drawings) of the test model not previously presented in the main text. The first of these, the adaptor flange shown in Figure 3 and Figure 50, is an existing transverse jet facility component which was modified for this application by adding a provision for a 0.5 inch (12.7 mm) high pressure line to supply the inner nozzle with helium. This modification entailed the drilling of a 0.5 hole radially into the flange sidewall which intersects at a right angle with a second passage drilled from the rear face of the flange though half of its thickness. This forms a 0.5 inch 90 degree elbow passage though the flange, the ends of which are pipe threaded to accept NPT fittings. The helium supply line is attached to the side wall flange fitting which is in turn connected to the centerbody with a steel tube fitted to the rear flange face inside the plenum and spanning the plenum pressure chamber, thus completing the helium supply line connection. The in-line flow straightener (composed of a seven hole steel insert as shown in Figure 7 and Figure 51) is placed downstream of the final bend in the supply line in order to remove unwanted vorticity to the flow.

The support flange shown in Figure 4 and Figure 52 is constructed of a 15-5 stainless steel, heat treated 935 °F (791 °K) to take the metal from a “zero” to a T4 hardness condition. This stock (initially acquired in its “zero” condition - essentially the raw form of a given aluminum alloy prior to the application of any heat treatment procedure) was first milled into a circular plate of 11.5 inches (292 mm) in diameter, the flats and spickets milled in order to provide a precision machined surface on which to locate the high pressure O-ring seals, and clearance holes drilled for the high strength bolts which secure it as well as the centerbody which is inserted through the

center hub of this flange and secured on the flange rear face by a locking nut. The three support struts which hold the centerbody in place (when secured in the aforementioned collar) are then cut out using a wire EDM (or electron discharge machining) process. The EDM process involves the removal of material by applying an extremely high voltage charge which is localized about an electrode. The electrode (composed of graphite) essentially cuts through the material by vaporizing it. This method is extremely well suited to several of our specialized machining requirements. A key attribute is the various forms which an EDM electrode may be employed such as many specialized surface geometries, wires or drills. With this procedure three crescent shaped passages are carved from the support flange, with the material which remains forming the support struts. These are the passages through which the air coflow passes while keeping the support struts themselves intact. The three struts are then rough tapered at the leading and trailing edge with a counterboring drill. The complex nature of this particular geometry prohibits the use of conventional machining techniques, thus EDM is again used to create the struts' tapered corners and sharpened edges. This is accomplished by plunging the graphite EDM electrode down along the walls of the support flange internal passages until it contacts the corners of the strut leading or trailing edges.

As mentioned above, the centerbody nozzle component shown in Figure 5 and Figure 53 is also fabricated of 15-5 stainless steel (which is heat treated before beginning the machining process). Because of the complex nature of the inner nozzle flow passage as well as the degree of machining precision required of the inner nozzle contour itself (in order to obtain the desired flow quality), the nozzle was machined in two pieces and joined in a brazing process at a later time. The longer of the two pieces (approximately 7 inches, 178 mm in length), called the centerbody "body", possessed however the less complex of the two internal geometries. The centerbody

nozzle flow passage diameter is determined by the wall thickness in the region required to maintain the stipulated stiffness during nozzle operation. This end is also outfitted appropriately so as to mate securely to the helium supply line fitting as well as to accommodate a locking nut with which the inner nozzle is secured to the support flange.

The internal passage of the centerbody body is tapered out to a slightly larger internal diameter downstream of the portion which slides into the support flange (the critical area of material strength) in order to match the diameter of the second piece of the centerbody (the centerbody “head”). The end of the body is machined to mate precisely to the head with provisions made for the brazing procedure which the finished component, will undergo (consisting of two circumferential troughs into which a copper braising wire is place). After the finished pieces are assembled with the brazing wire in place they will be vacuum brazed to 2050 °F. In the brazing process, copper filaments liquefy and flow from troughs to cover the interfacing to form a continuous metal to metal junction. The finished component is nearly as strong as a solid component of like dimension and the method of joining allows alignment accuracy to be determined purely by machining tolerances of the two mating components.

The outer surface of the centerbody head is rough machined to within a few thousandths of its final shape before the aforementioned brazing. Recall that it is this outer surface which forms the middle contour for the coflow nozzle and requires every bit as much precision as does the inner contour for the centerjet nozzle. For this reason, the middle contour is machined to its final dimension with one continuous machining cut once the pieces have been joined. This assures the absence of seams and/or surface nonuniformities. The head of the centerbody (approximately three inches in length) critical to the overall performance of the centerjet nozzle from a fluid dynamic standpoint. The entire compression and subsequent expansion process

which the centerjet undergoes in transitioning to supersonic flow occurs over this three inch length. An array of drills are used to form the approximate interior flow passage diameter. The nozzle is turned on a lathe from the exit inwards using a specially designed tungsten carbide tool to reach inside the nozzle behind the throat minimum when the nozzle begins to expand to the inner passage diameter. The nozzle is then turned with the tool extending from the other end and the seam between the two bores is exactly matched and finished.

Near the sonic throats both the core and coflow nozzle surfaces are finished to 16 due to the sensitivity of the flows to perturbations in this region. Over most regions however, a less stringent 32 finish was specified with all brazes and seams polished to the point of being indistinguishable from the machined contour surfaces. The finish quality (of 16 or 32 as stated above) refers to the average surface roughness in microinches (the roughness profile's average deviation from the graphical centerline<sup>31</sup>).

The materials used for the coflow nozzle main body, shown in Figure 6 and Figure 54 was drawn from a stock of somewhat aged 2014 aluminum was located in NASA stores which was authenticated with x-ray composition analysis and tested for composition and hardness. As this stock was also acquired in the "zero" condition, the ingot underwent a somewhat extensive conditioning regimen in order to take it from a T4 to a T6 hardness level - the maximum level of aluminum heat treatment. During the heat treatment process carbon deposited throughout a given metal specimen is drawn to the surface and it is this concentrated carbon deposit which accounts for the hardening effect and provides a hardened surface for precision machining processes.

In order to extend the coflow nozzle outer contour an outer nozzle exit cone was manufactured to mate to the alignment rim of the outer nozzle exit lip seen in Figure 6 and also detailed in Figure 55. This 2025 aluminum extension cone is secured directly to the outer nozzle

lip with its constant inner diameter matched exactly to that of the coflow nozzle main body. This piece is externally tapered to provide a smooth merging of the entrained ambient air and the coflow jet at the nozzle exit.

As described in Section 3.2, these basic coannular jet nozzle components (proceeding from the top to the bottom): transverse facility adaptor flange, nozzle adaptor and support flange, centerbody, and coflow nozzle body, are assembled as illustrated in Figure 56 as well as shown previously in Figure 4 through Figure 7.

The aluminum alignment tools described in section 4.2 were machined in various height increments ranging from 10 to 80 millimeters as shown in Figure 57. They consist of a cap which fits snugly atop the outer nozzle lip alignment rim, and several 1 inch diameter aluminum dowel rods: 10, 20, 40, and 80 mm in length. If these pieces are stacked the maximum survey height of 240 mm (as well as all other relevant survey heights) can be obtained.

## 9.0 APPENDIX B - Uncertainty Analysis

### 1. UNCERTAINTY ANALYSIS: LOWER PLENUM PRESSURE MEASUREMENT

**DEVICE:** PRESSURE TRANSDUCER, OUTPUT RANGE=0-200PSIA (1378.6 kPa)

<b>ERROR SOURCES:</b>	<b>PRECISION(S)</b>	<b>BIAS(B)</b>
DRUCK CALIBRATION ERROR:	0.42 kPa	
DATA ACQUISITION ERROR: -NON-LINEARITY -HYSTERESIS -REPEATABILITY	16.30 kPa	
DATA RECORDING:	0.02 kPa	0.34 kPa
<b>ROOT SUM SQUARE OF DATA SOURCES</b>	<b>16.30 kPa</b>	<b>0.34 kPa</b>
<b>EXPERIMENTAL UNCERTAINTY, <math>U=(B+t_{95}S) = 2.39\%</math> FULL SCALE</b>		

### 2. UNCERTAINTY ANALYSIS: UPPER PLENUM PRESSURE MEASUREMENT

**DEVICE:** PRESSURE TRANSDUCER, OUTPUT RANGE=0-100 PSIA (689.3 kPa)

<b>ERROR TYPE:</b>	<b>PRECISION(S)</b>	<b>BIAS(B)</b>
DRUCK CALIBRATION ERROR:	0.21 kPa	
DATA ACQUISITION ERROR: -NON-LINEARITY - -HYSTERESIS - -REPEATABILITY-	3.31 kPa	
DATA RECORDING:	0.01 kPa	0.16 kPa
<b>ROOT SUM SQUARE OF DATA SOURCES</b>	<b>3.32 kPa</b>	<b>0.16 kPa</b>
<b>EXPERIMENTAL UNCERTAINTY, <math>U=(B+t_{95}S) = 0.99\%</math> FULL SCALE,</b>		

### 3: UNCERTAINTY ANALYSIS: HELIUM STATIC PRESSURE MEASUREMENT

DEVICE: PRESSURE TRANSDUCER, OUTPUT RANGE=0-100PSIA (689.3 kPa)

ERROR TYPE:	PRECISION(S)	BIAS(B)
DRUCK CALIBRATION ERROR:	0.21 kPa	
DATA ACQUISITION ERROR: -NON-LINEARITY - -HYSTERESIS - -REPEATABILITY-	2.43 kPa	
DATA RECORDING:	0.01 kPa	0.14 kPa
ROOT SUM SQUARE OF DATA SOURCES	2.44 kPa	0.14 kPa
EXPERIMENTAL UNCERTAINTY, $U=(B+t_{95}S) = 0.73\%$ FULL SCALE		

### 4: UNCERTAINTY ANALYSIS: PITOT PROBE PRESSURE MEASUREMENT

DEVICE: PRESSURE TRANSDUCER, OUTPUT RANGE=0-100PSIA (689.3 kPa)

ERROR TYPE:	PRECISION(S)	BIAS(B)
DRUCK CALIBRATION ERROR:	0.21 kPa	
DATA ACQUISITION ERROR: -NON-LINEARITY - -HYSTERESIS - -REPEATABILITY-	3.72 kPa	
DATA RECORDING:	0.01 kPa	0.11 kPa
ROOT SUM SQUARE OF DATA SOURCES	3.73 kPa	0.11 kPa
EXPERIMENTAL UNCERTAINTY, $U=(B+t_{95}S) = 1.10\%$ FULL SCALE		

## 5: UNCERTAINTY ANALYSIS: NOZZLE STATIC PRESSURE MEASUREMENT

DEVICE: PRESSURE TRANSDUCER, OUTPUT RANGE=0-25PSIA (172.3 kPa)

ERROR TYPE:	PRECISION(S)	BIAS(B)
DRUCK CALIBRATION ERROR:	0.05 kPa	
DATA ACQUISITION ERROR: -NON-LINEARITY -HYSTERESIS -REPEATABILITY	2.13 kPa	
DATA RECORDING:	0.002 kPa	0.04 kPa
ROOT SUM SQUARE OF DATA SOURCES	2.14 kPa	0.04 kPa
EXPERIMENTAL UNCERTAINTY, $U=(B+t_{95}S) = 2.51\%$ FULL SCALE		

## 6: UNCERTAINTY ANALYSIS: NOZZLE TEMPERATURE MEASUREMENTS

DEVICE: TYPE T THERMOCOUPLE

ERROR TYPE:	PRECISION(S)	BIAS(B)
CALIBRATION SYSTEM ERROR:		
LAB THERMOMETER ERROR	1.10 K	0.28 K
COLD JUNCTION SENSOR	1.0 K	0.13 K
DATA RECORDING:	0.13 K	0.39 K
ROOT SUM SQUARE OF DATA SOURCES	1.49 K	0.49 K
EXPERIMENTAL UNCERTAINTY, $U=(B+t_{95}S) = 3.41$ K		



## 10.0 REFERENCES

- 1 Heiser, W.H., and Pratt, D.T., with Daley, D.H. and Mehta, U.B., *Hypersonic Airbreathing Propulsion*, AIAA Educational Series, AIAA Inc. Washington D.C. 1991
- 2 Diskin, G.S., 1997, "Experimental and Theoretical Investigation of the Physical Processes Important to the *RELIEF* Flow Tagging Diagnostic," Ph.D. Dissertation, Princeton University.
- 3 White, F.M., *Viscous Fluid Flow, 2nd Edition*, McGraw -Hill, 1991, pp. 254-256 and 476-478.
- 4 Brown G.L. and Roshko, A., "On Density Effects and Large Structures in Turbulent Mixing Layers," *Journal of Fluid Mechanics*, Vol. 64, Part 4, 1974, pp. 775-816
- 5 Bogdanoff, D.W., "Compressibility Effects in Turbulent Shear Layers," *AIAA Journal*, Vol. 21, No. 6, 1983, pp. 926-927.
- 6 Papamoschou, D. and Roshko, A. "Observations of Supersonic Free Shear Layers," AIAA Paper 86-0162, January 1986.
- 7 Papamoschou, D. and Roshko, A. "The Compressible Turbulent Shear Layer: an Experimental Study," *Journal of Fluid Mechanics*, Vol. 197, 1988, pp. 453-477
- 8 Dimotakis, P. E., "Turbulent Free Shear Layer Mixing," *AIAA 27th Aerospace Sciences Meeting*, 9-12 January 1989 (Reno, Nevada), AIAA Paper 89-0262.

- 9 Dimotakis, P. E., "On the Convection Velocity of Turbulent Structures in Supersonic Shear Layers," *AIAA 22nd Fluid Dynamics, Plasma Dynamics and Lasers Conference*, 9-12 June 1991 (Honolulu, Hawaii), AIAA Paper 91-1724.
- 10 Clemens, N.T., and Mungal, M.G. "Large Scale Structure and Entrainment in the Supersonic Mixing Layer," *Journal of Fluid Mechanics*, Vol. 284, 1995, pp. 171-216.
- 11 Abramovich, G.N., *Theory of Turbulent Jets*, M.I.T. Press, 1943.
- 12 Smits, A.J. and Dussauge, J., *Turbulent Shear Layers in Supersonic Flow*, AIP Press 1996
- 13 Fourguette, D.C., Mungal, M.G. and Dibble, R.W., "Time Evolution of the Shear layer of a Supersonic Axisymmetric Jet," *AIAA Journal*, Vol. 29, No. 7, 1991, pp. 1123-1130.
- 14 Freund, J.B., Lele, S.K., Moin, P., "Direct Simulation of a Supersonic Round Turbulent Shear Layer," *AIAA 35th Aerospace Sciences Meeting*, 6-10 January 1997 (Reno, Nevada), AIAA Paper 97-0760.
- 15 Wilder Jr., J.G. and Hindersinn, K., "Spreading of Supersonic Jets in Supersonic Streams," Institute of the Aeronautical Sciences Inc., *Aeronautical Engineering Review*, October 1953.
- 16 Schadow, K.C., Gutmark, E., and Wilson, K.J., "Passive Mixing Control in Supersonic Coaxial Jets at Different Convective Mach Number," *AIAA 2nd Shear flow Conference*, 13-16 March 1989 (Tempe, Arizona), AIAA Paper 89-0995.
- 17 Gutmark, E., Schadow, K.C., and Wilson, K.J., "Mixing Enhancement in Supersonic Jets," *AIAA 20nd Fluid Dynamics, Plasma Dynamics and Lasers Conference*, 12-14 June 1989 (Buffalo, New York), AIAA Paper 89-1812.

- 18 Gutmark, E., Schadow, K.C., and Wilson, K.J., "Effect of Convective Mach Number on Mixing of Coaxial Circular and Rectangular Jets," *Physics of Fluids*, Vol. 3, January 1991, pp. 29-36.
- 19 Harris, J.E., Blanchard, D.K., "Computer Program for solving Laminar, Transitional or Turbulent Compressible Boundary-Layer Equations for Two Dimensional and Axisymmetric Flow," NASA Technical Memorandum 83207, 1982.
- 20 Drummond, J.P., "A Two -Dimensional Numerical Simulation of a Supersonic Chemically reacting Mixing Layer," NASA Technical Memorandum 4055, 1988.
- 21 Young, W.C., *Roark's Formulas for Stress and Strain - 6th ed.*, McGraw-Hill Inc. New York, 1989, pp. 201-226.
- 22 *LabVIEW for Windows Users Manual*, Part Num. 320534B-01, National Instruments Company, 6504 Bridge Point Parkway, Austin, Texas 78730-5039, 1994.
- 23 *LabVIEW for Windows DAQ VI Reference Manual*, Part Num. 320536B-01, National Instruments Company, 6504 Bridge Point Parkway, Austin, Texas 78730-5039, 1994.
- 24 Quinn, J. E., "Drag Reduction of Supersonic Cavities via Mass Injection with Applications to Scramjets," M.S. Thesis, School of Engineering and Applied Science, The George Washington University, 1997.
- 25 Johnson, C. H., "Applications of Streamwise Vorticity in Enhancement of Injectant Mixing and Penetration in a Supersonic Flow," M.S. Thesis, School of Engineering and Applied Science, The George Washington University, 1996.
- 26 Weinstein, L. M., "An Improved Large Field Focusing Schlieren System," *AIAA 29th Aerospace Sciences Meeting*, 7-10 January 1991 (Reno, Nevada), AIAA Paper 91-0567

- 27 Goldstein, R.J. Ed., *Fluid Mechanics Measurements*, 2nd Edition, Taylor and Francis, Washington D.C., 1996, Chapter 7.
- 28 Weast, R. C., Astle, M. J., Beyer, W. H. (Editors), *CRC Handbook of Chemistry and Physics*, 69th Edition, CRC Press Inc., 1988-1989, p. E-384.
- 29 *Photometrics -AT200 CCD Camera system, Hardware Reference Manual, 570075 Rev. A*, Photometrics Ltd., 3440 East Britannia Drive, Tuscon, Arizona 8570, 1992
- 30 *PMIS Image processing Software Users Manual, 570074 Version 1.5*, Photometrics Ltd., 3440 East Britannia Drive, Tuscon, Arizona 8570, 1992
- 31 *Surface texture - Surface Roughness, Waviness and Lay*, American National Standard, ANSI B46.1-1978, ASME, New York N.Y. 1978.

## 11.0 FIGURES

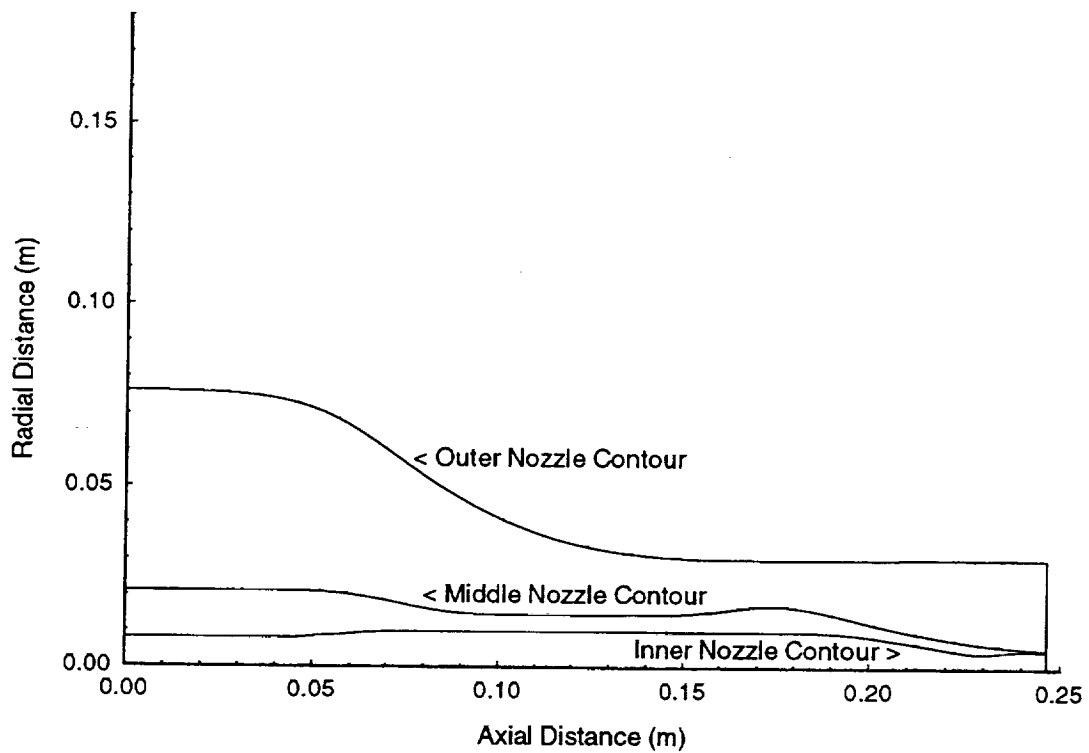


Figure 1: Viscous Corrected Nozzle Contours

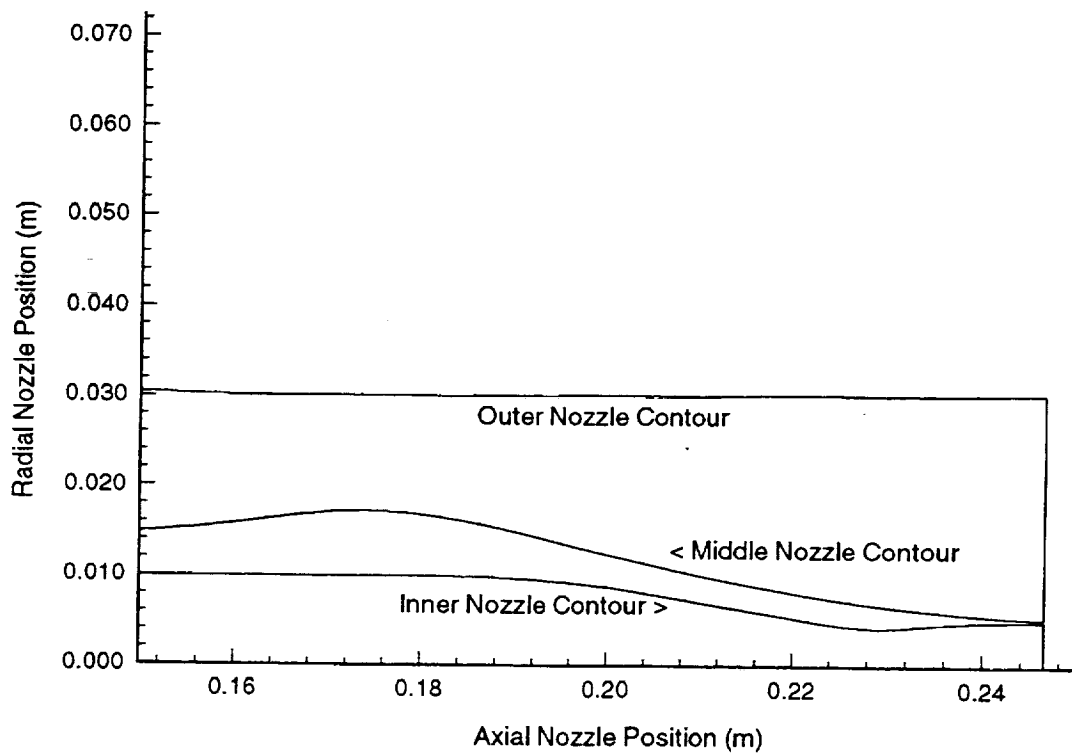
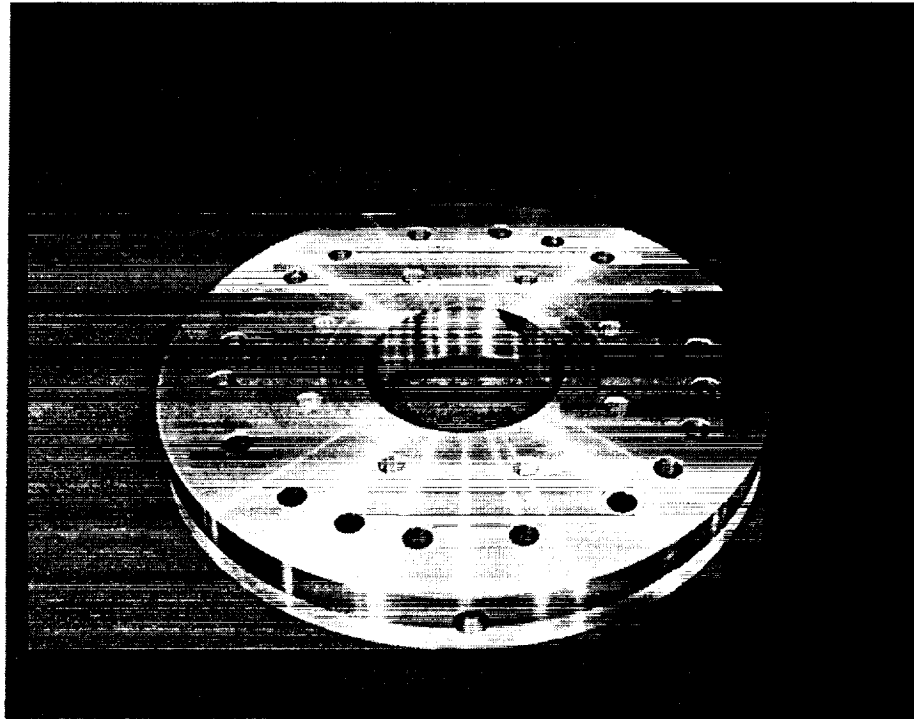
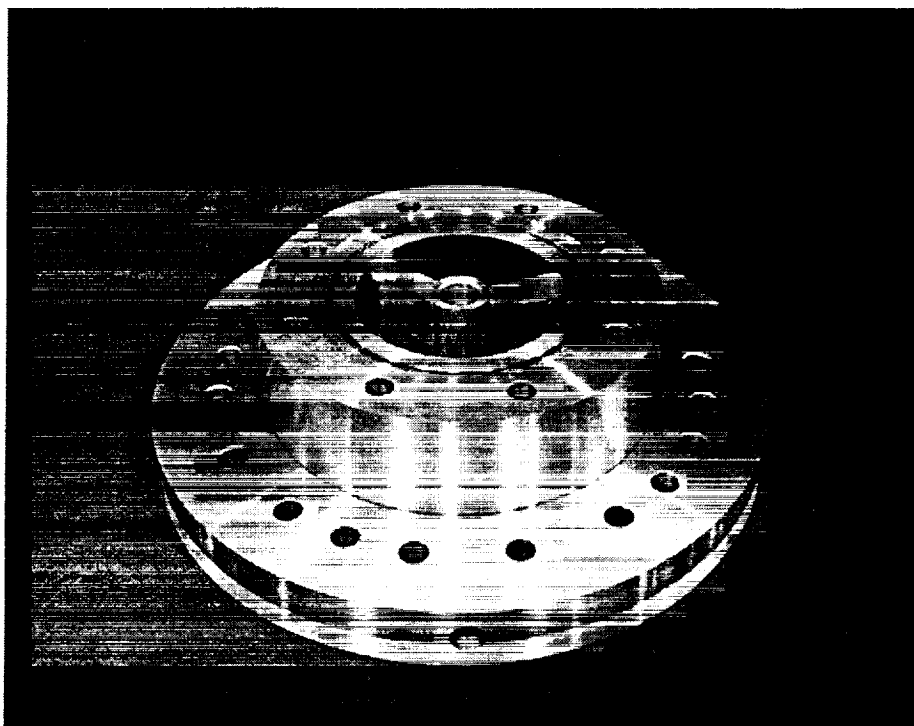


Figure 2: Viscous Corrected Nozzle Contours - Throat Region



**Figure 3: Transverse Jet Facility Adaptor Flange**



**Figure 4: Centerbody Support Flange**

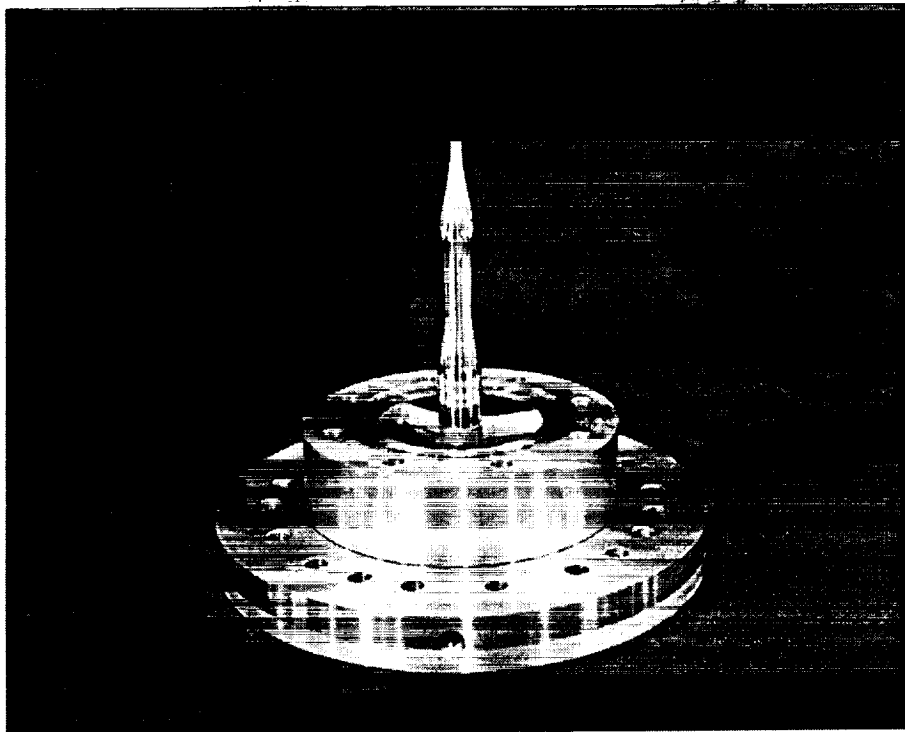


**Figure 5: Centerbody Secured in Support Flange**

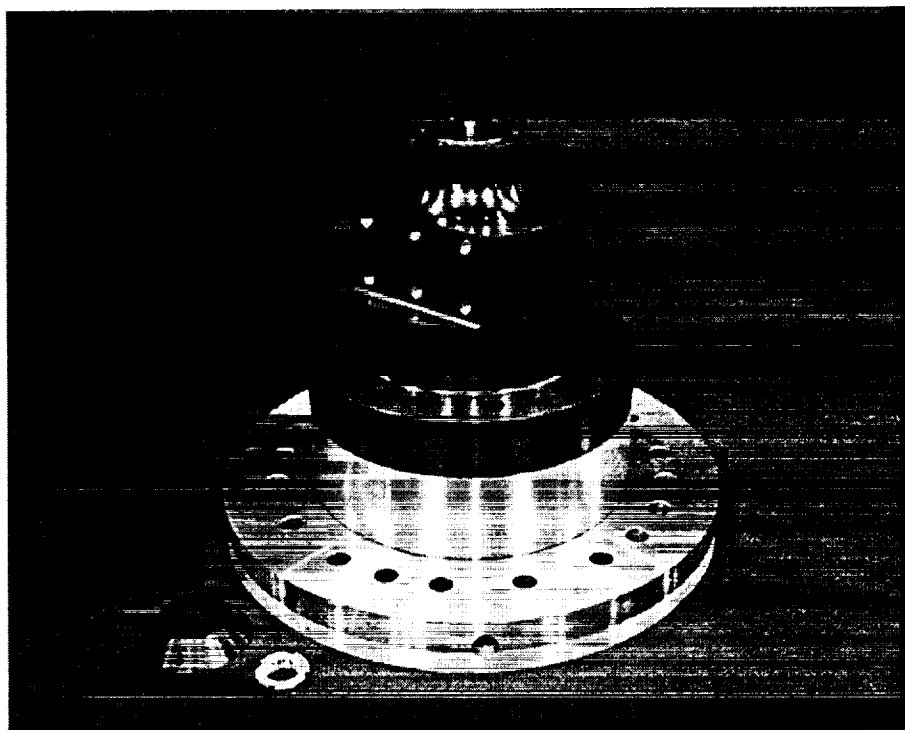


**Figure 6: Coflow Nozzle Body Mounted and Centered**

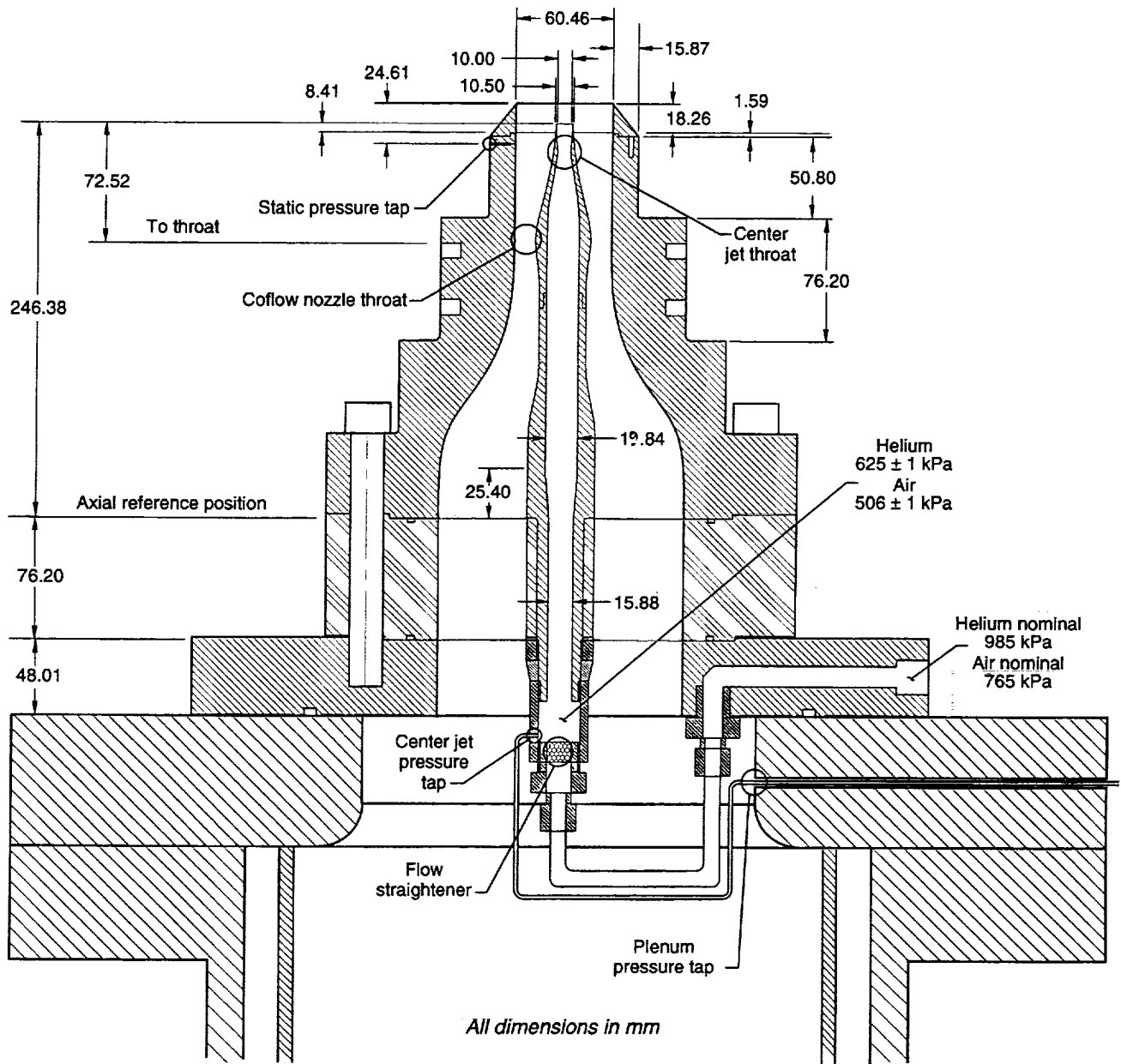


**Figure 7: Coannular Nozzle**



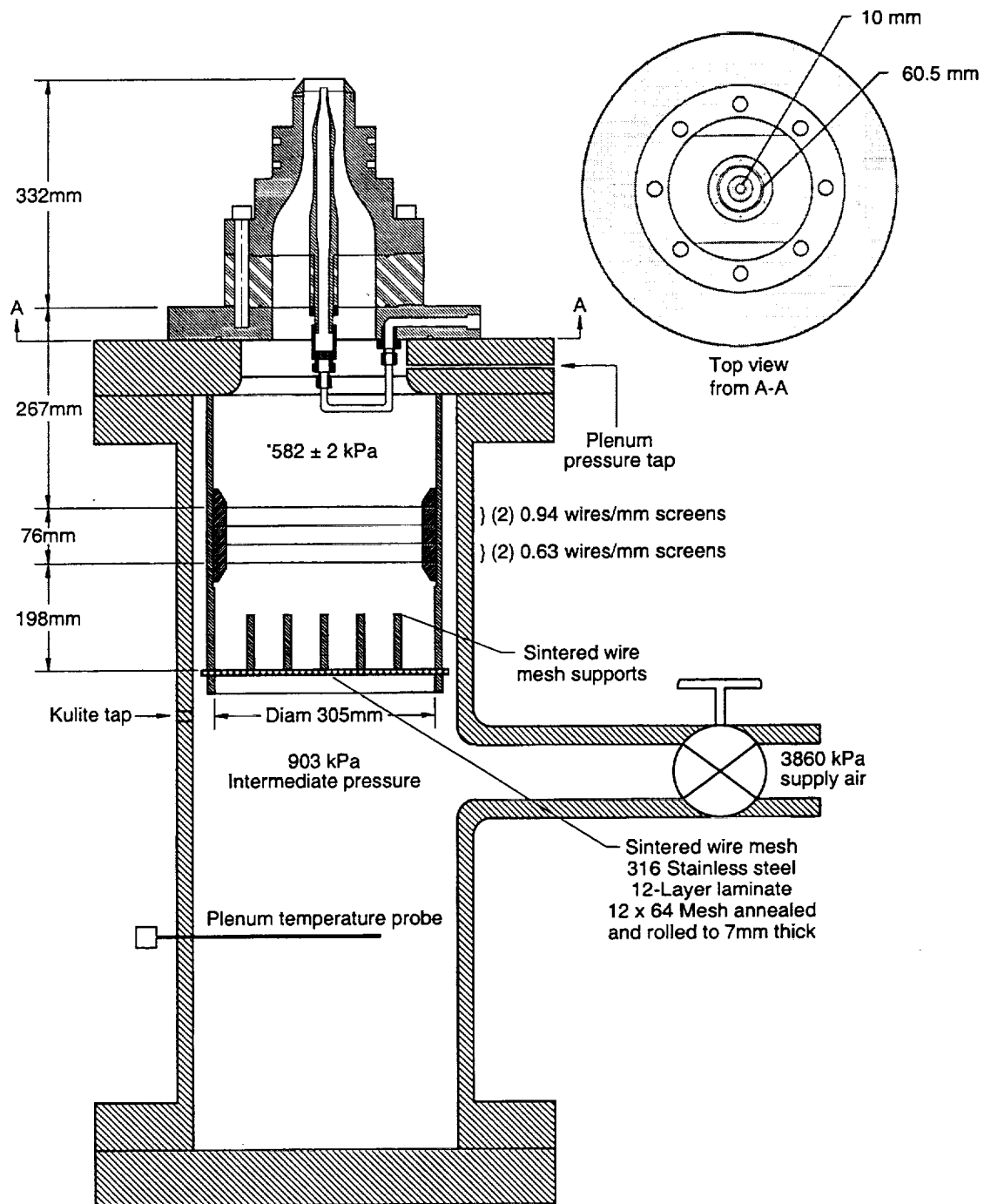


**Figure 8: Transverse Jet Facility**

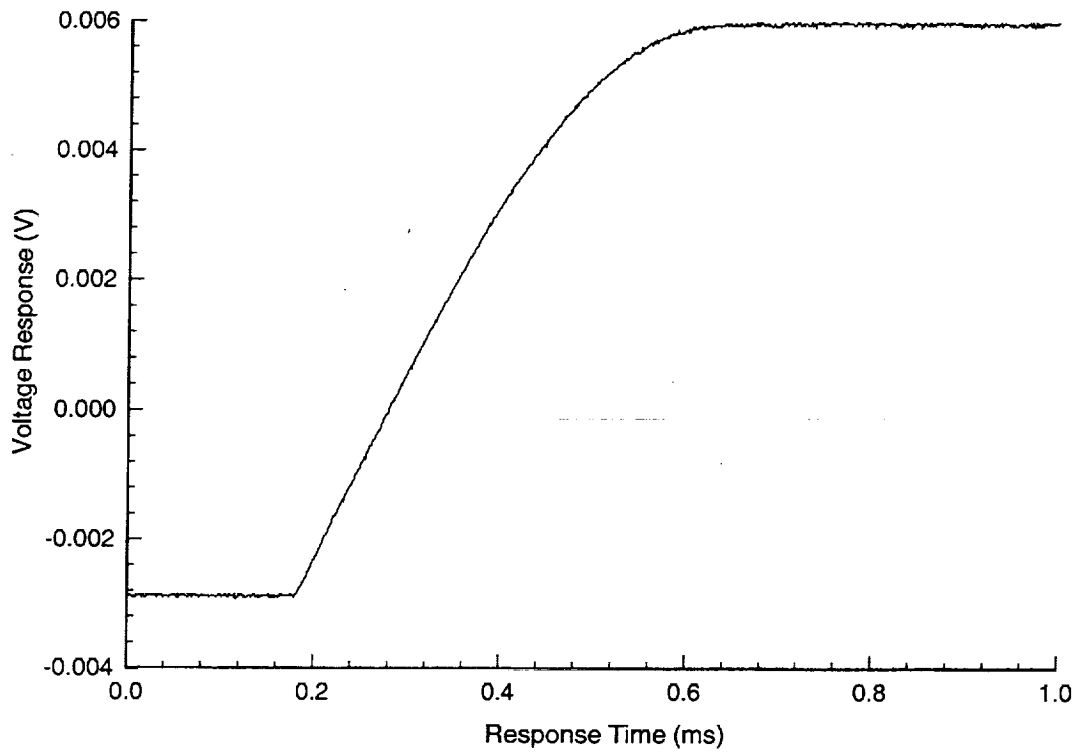


**Figure 9: Pitot Probe Response Time**

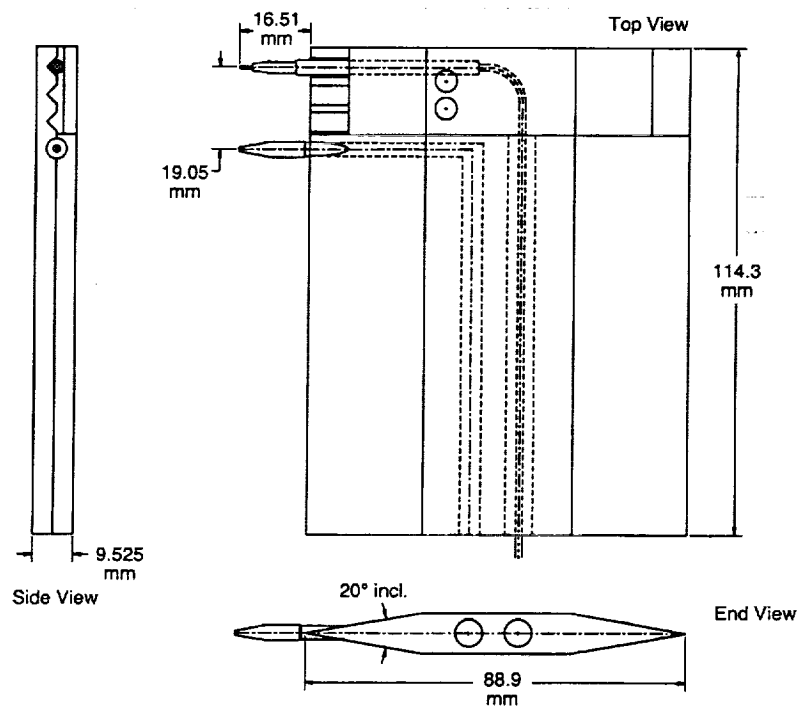


**Figure 10: Probe Survey Rake**

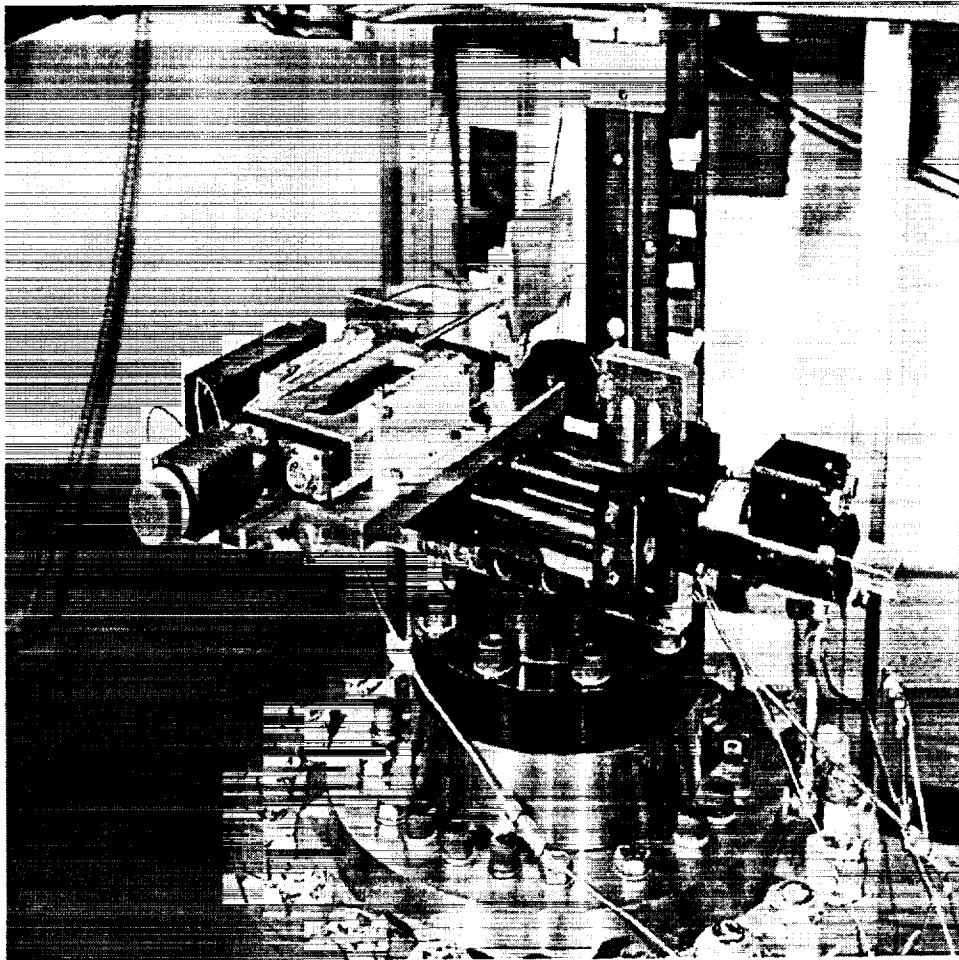


**Figure 11: Probe Translation Mechanism Installed on Model**

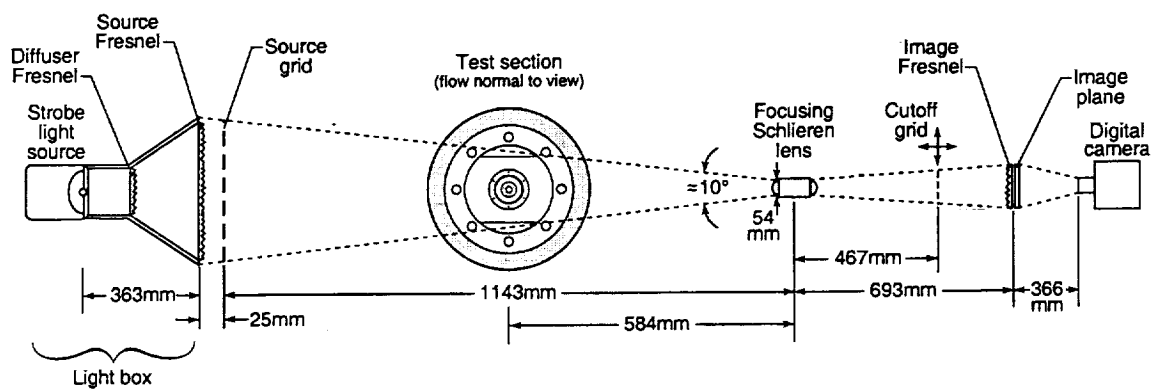


**Figure 12: Focusing Schlieren Flow Visualization System**

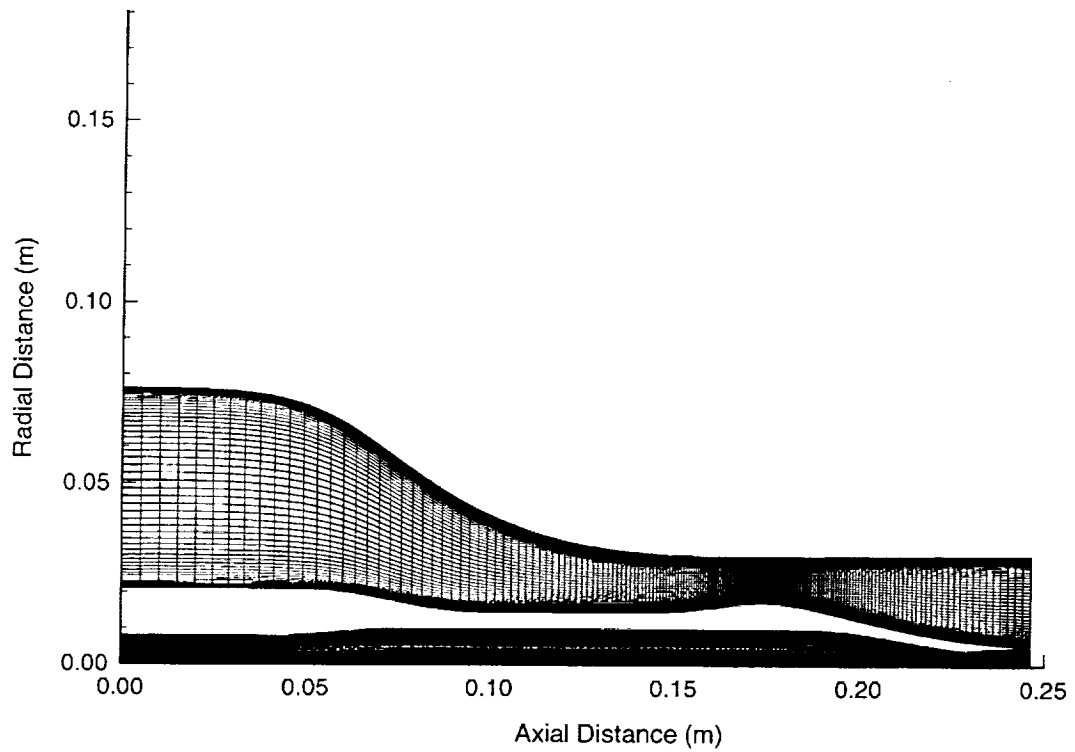


**Figure 13:Computational Grids - 201x51 Coflow, 201x25 Centerjet**

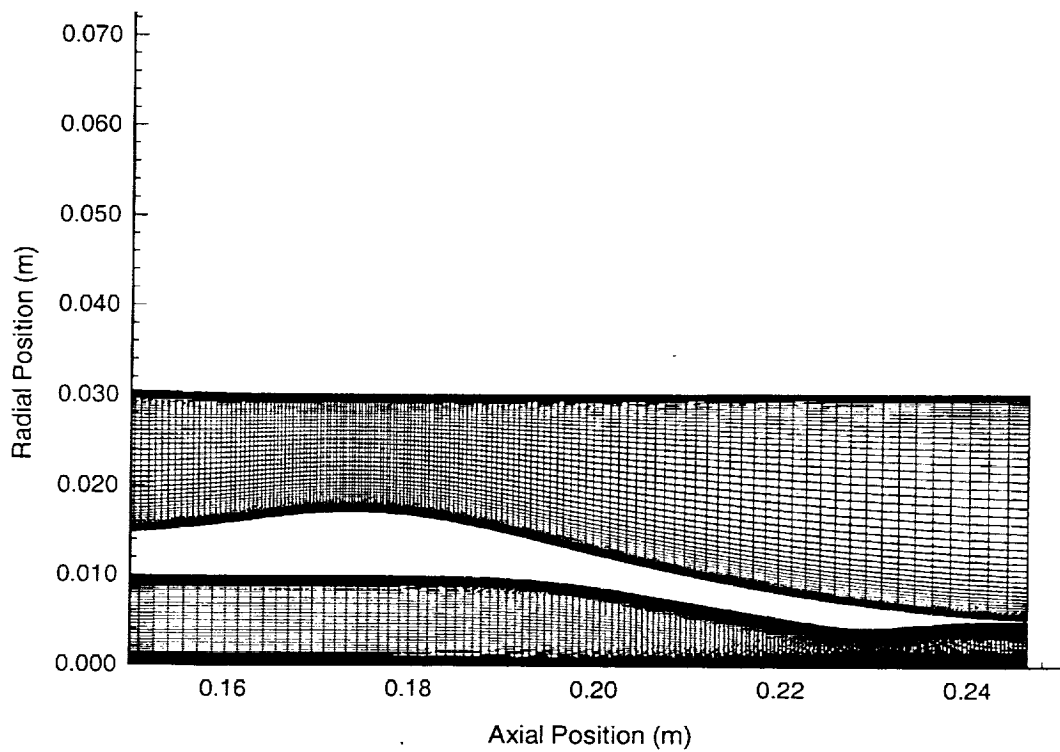


**Figure 14:Computational Grids - Clustering in Throat Regions**

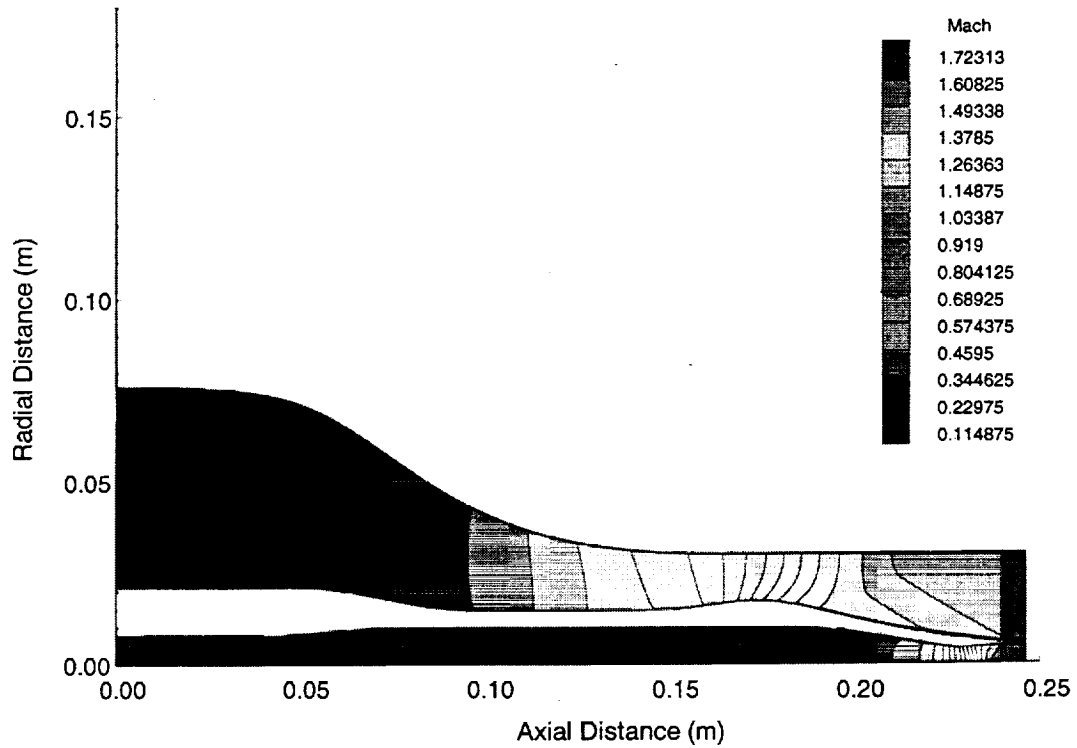


Figure 15:CFD Mach Contour Calculation - Air / He

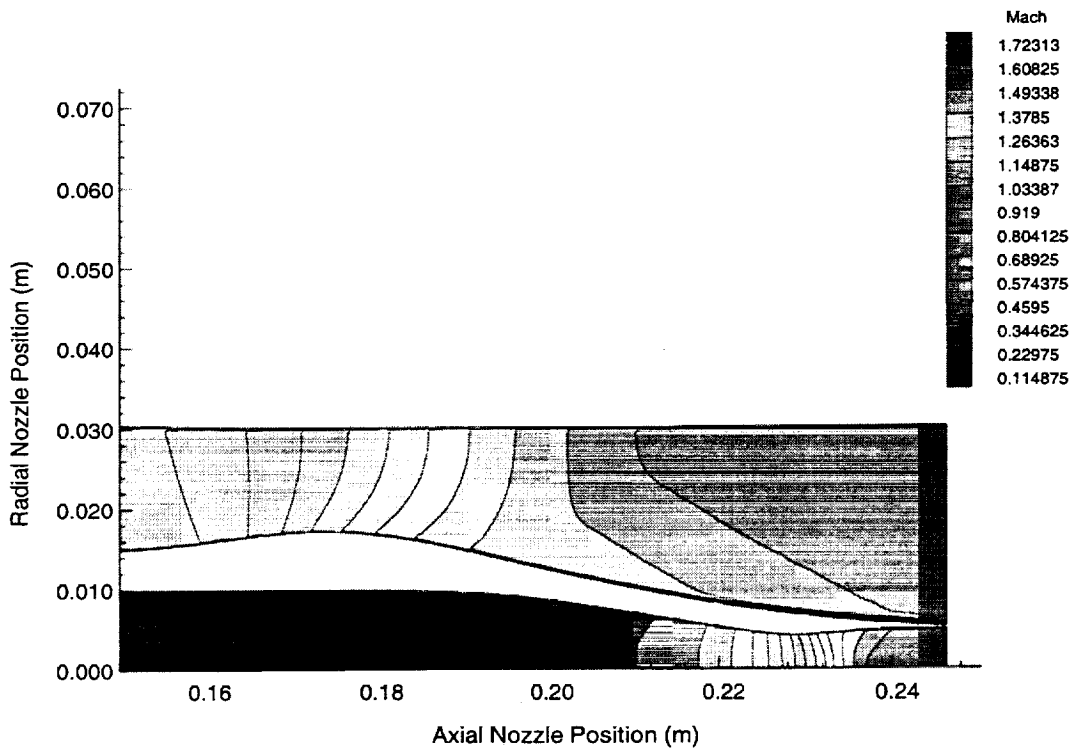


Figure 16:CFD Mach Contour Calculation - Air / He

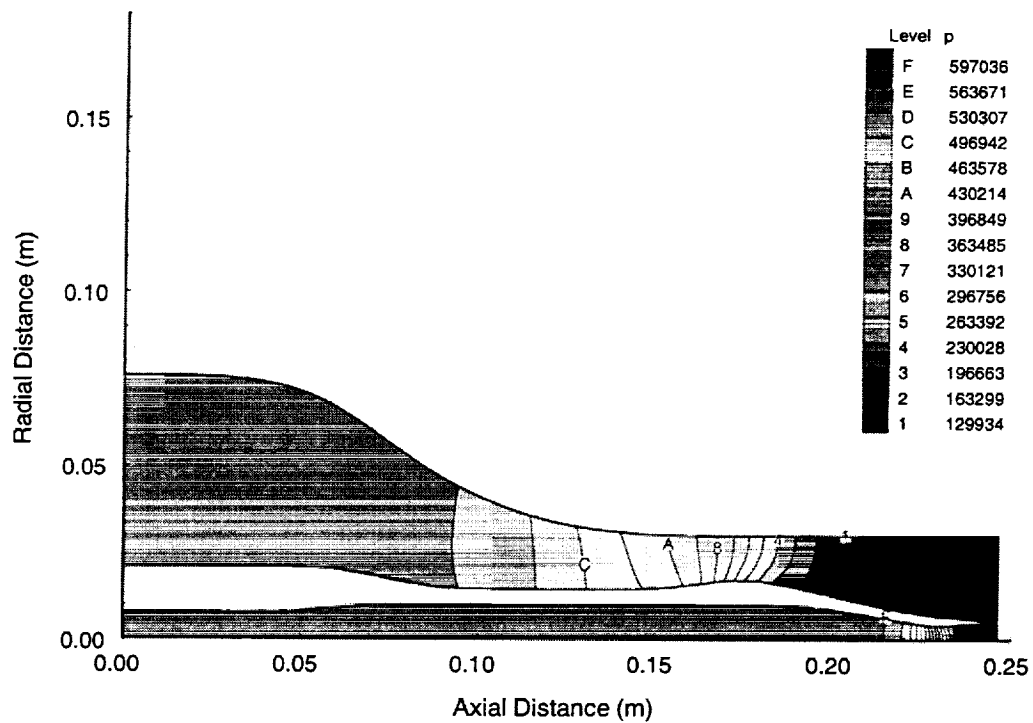


Figure 17:CFD Pressure Contour Calculation - Air / He

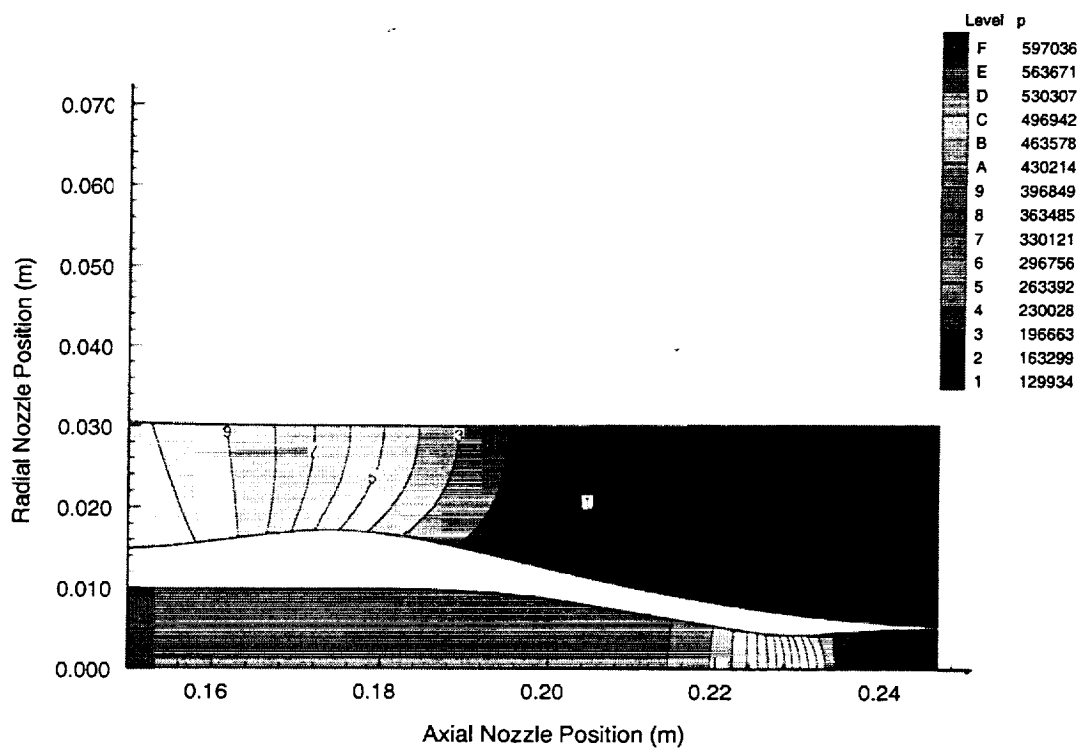
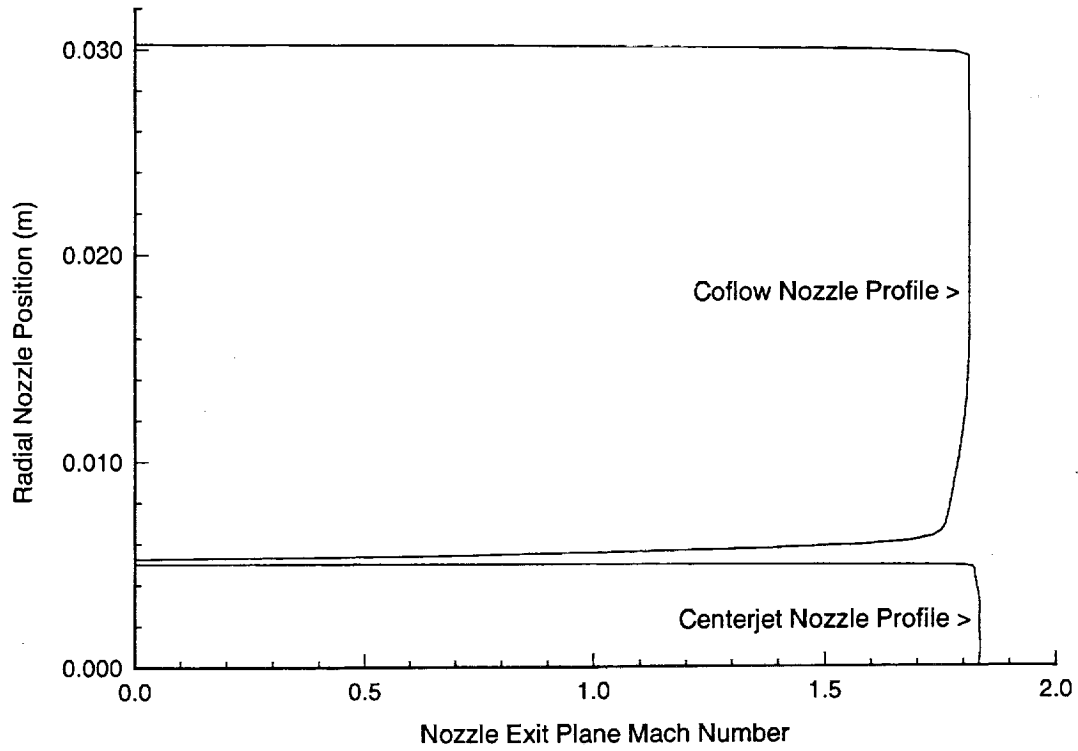
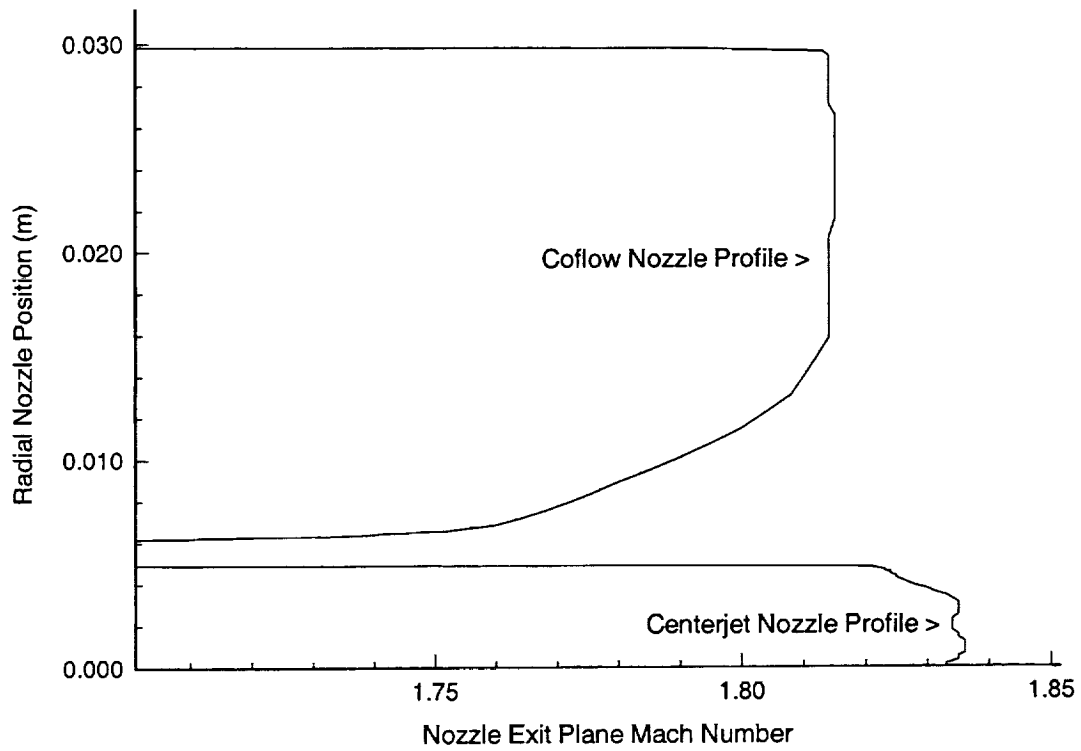


Figure 18:CFD Pressure Contour Calculation - Air / He



**Figure 19:Exit Plane Mach Profile**



**Figure 20:Exit Plane Mach Profile: Detail**

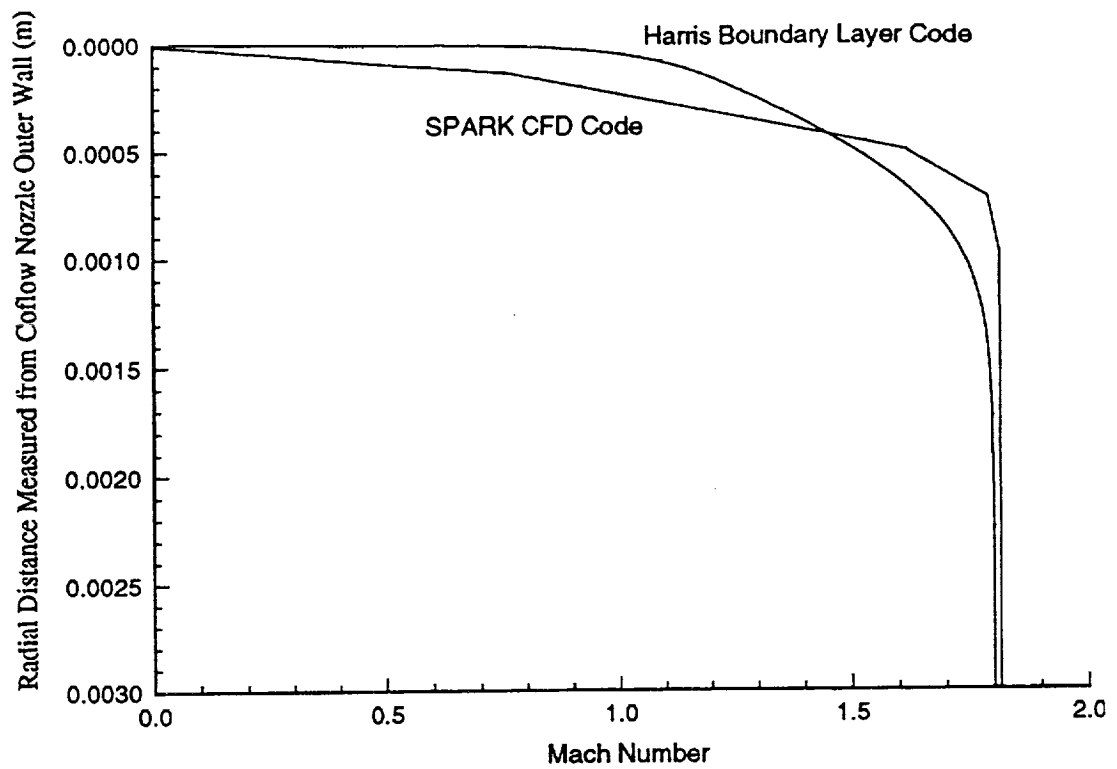


**Figure 21: Coflow Nozzle Exit Plane Boundary Layer: Outer Wall**

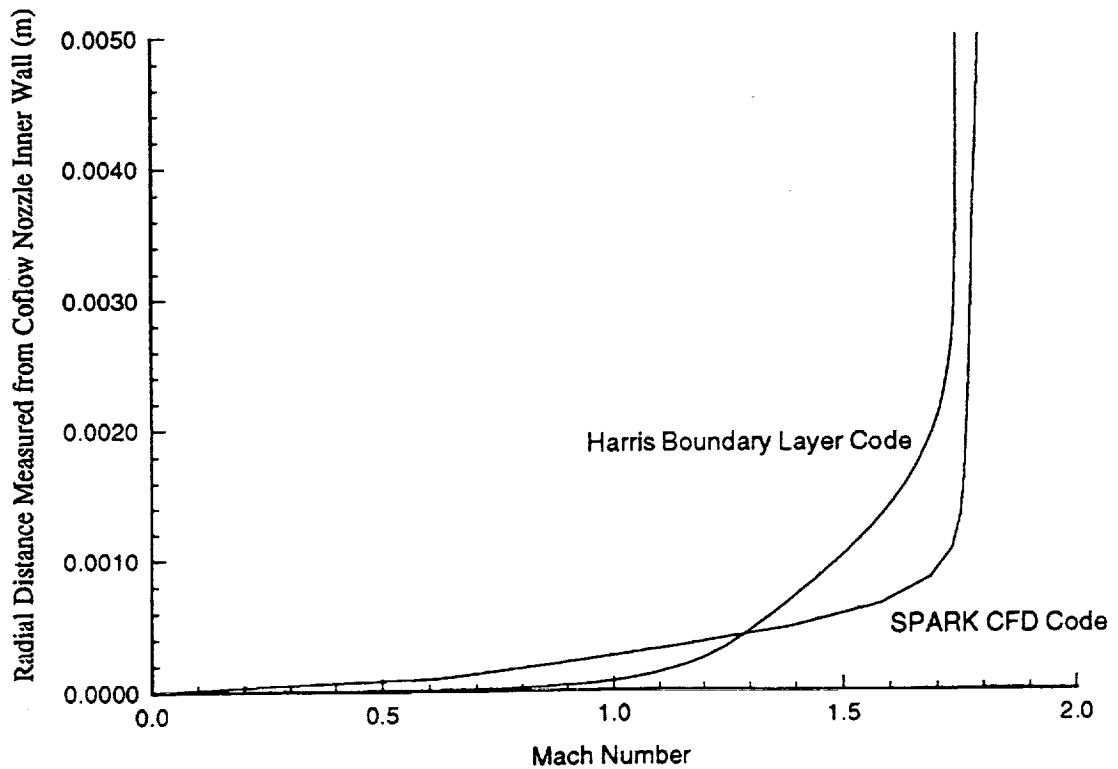


**Figure 22: Coflow Nozzle Exit Plane Boundary Layer: Inner Wall**



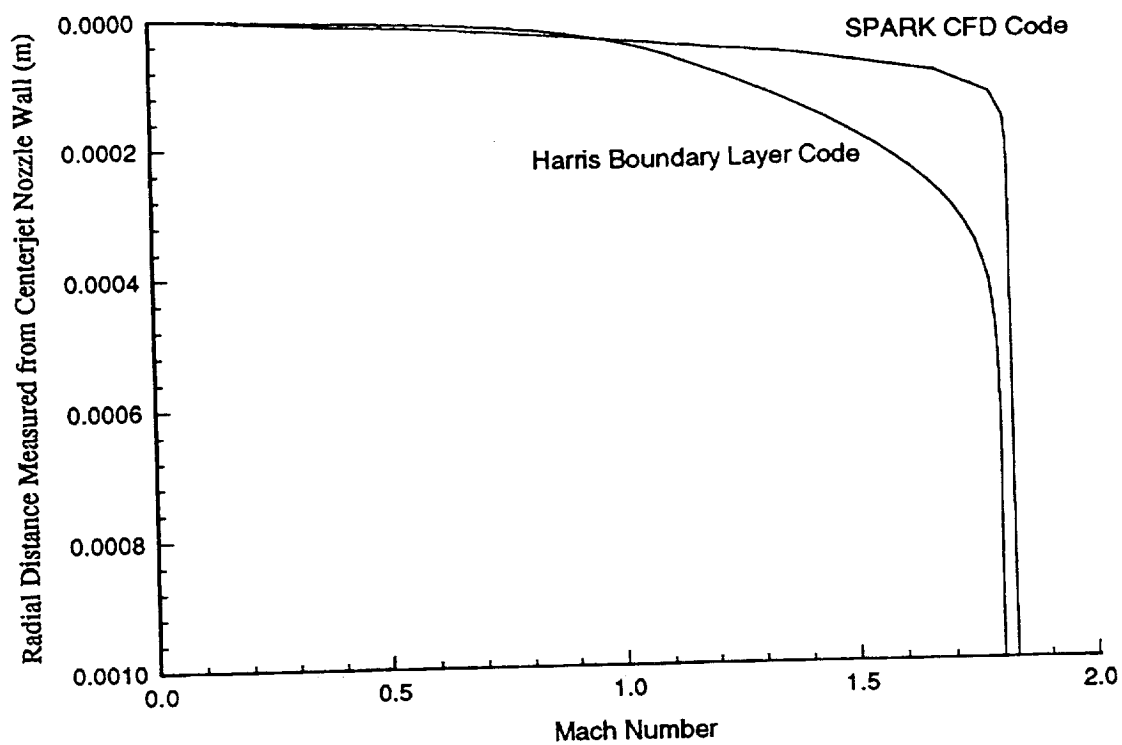


**Figure 23: Centerjet Nozzle Exit Plane Boundary Layer**

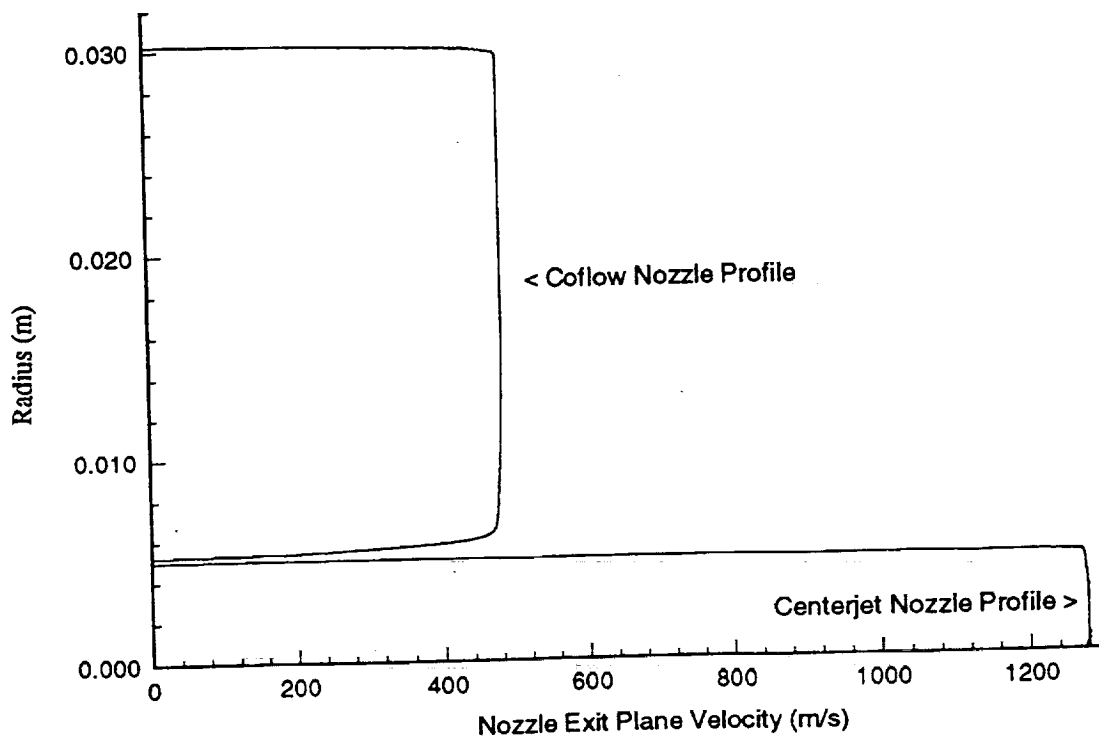
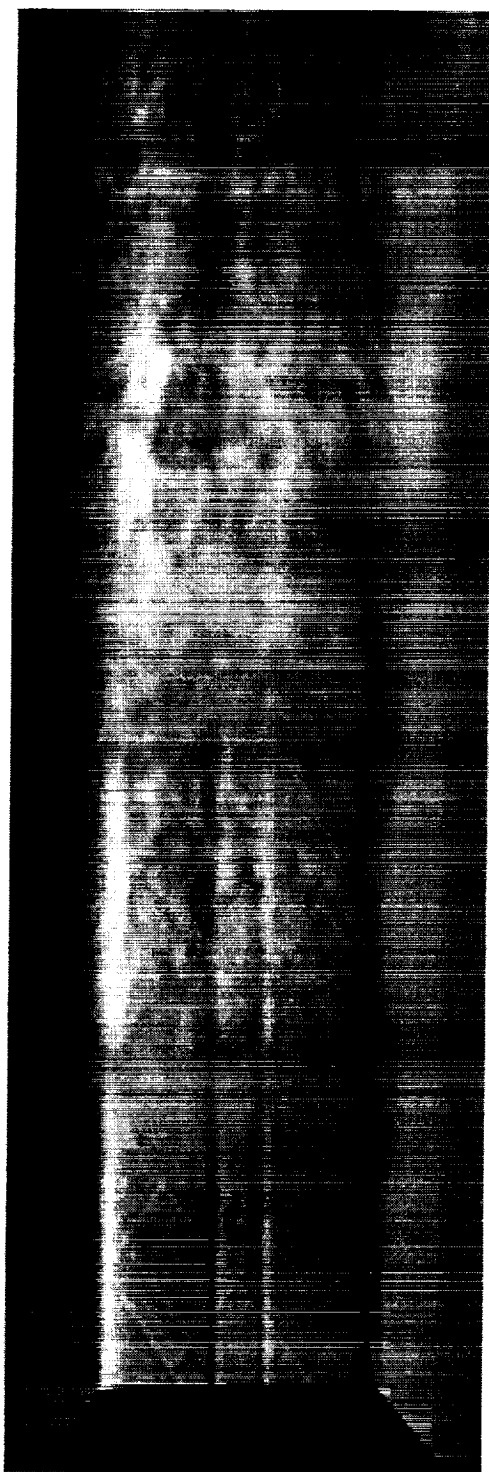
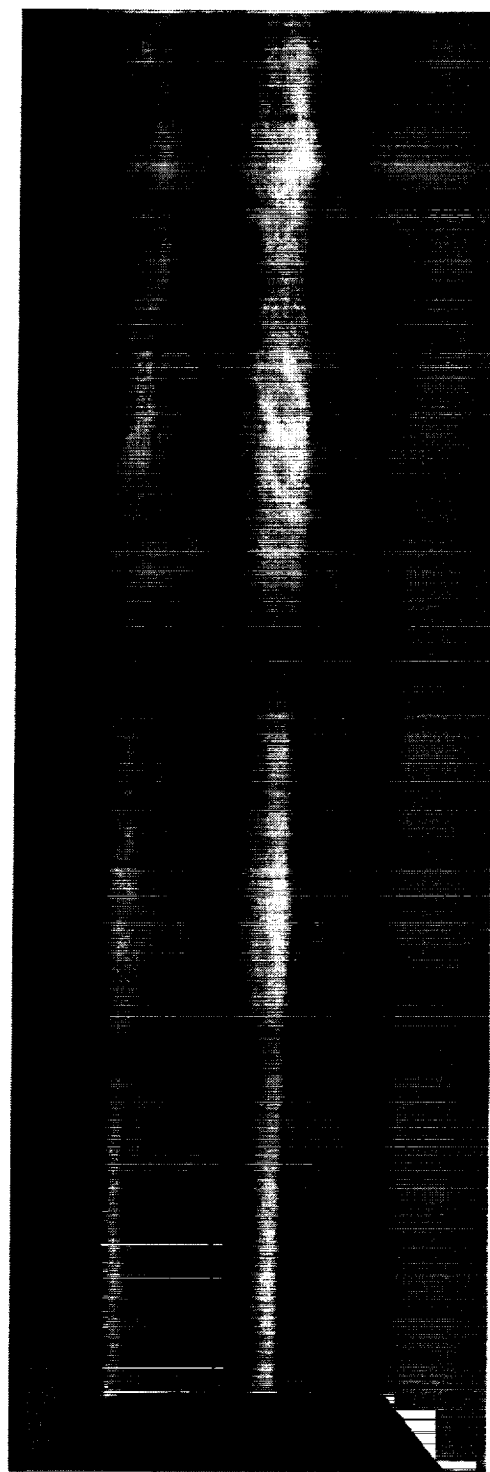


**Figure 24: Exit Plane Velocity Profile - Air Centerjet**



a)  $M=1.8$  Air coflow - Air centerjet



b)  $M=1.8$  Air coflow - He centerjet

**Figure 25: Focusing Schlieren Images Comparing Air and Helium Centerjet Flows**

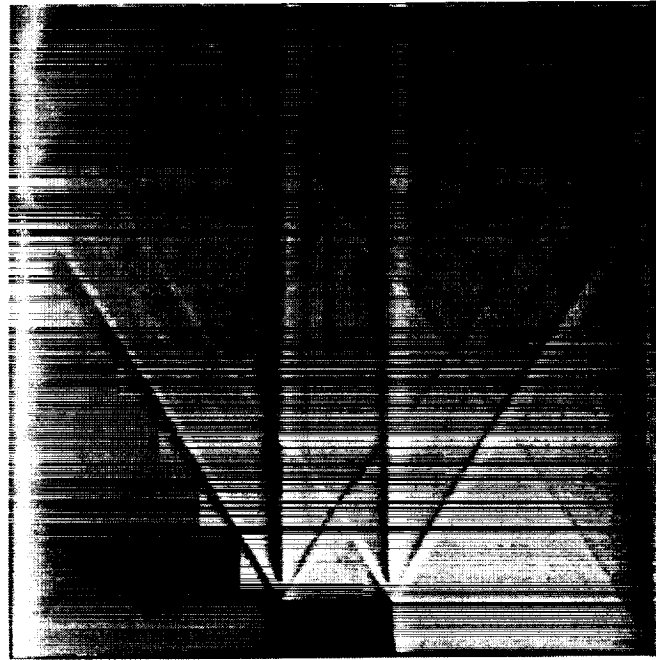


**Figure 26:Focusing Schlieren Image in Vicinity of Air Centerjet Nozzle Exit**

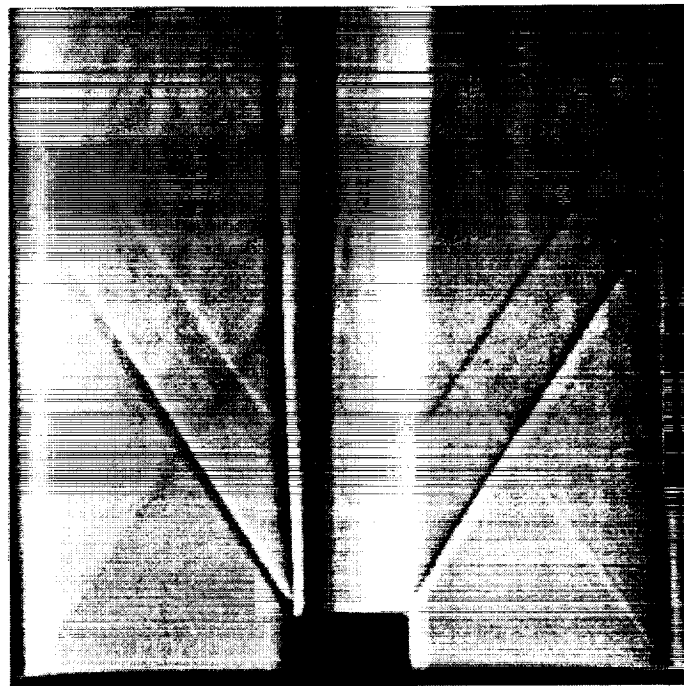


**Figure 27:Focusing Schlieren Image in Vicinity of Helium Centerjet Nozzle Exit**

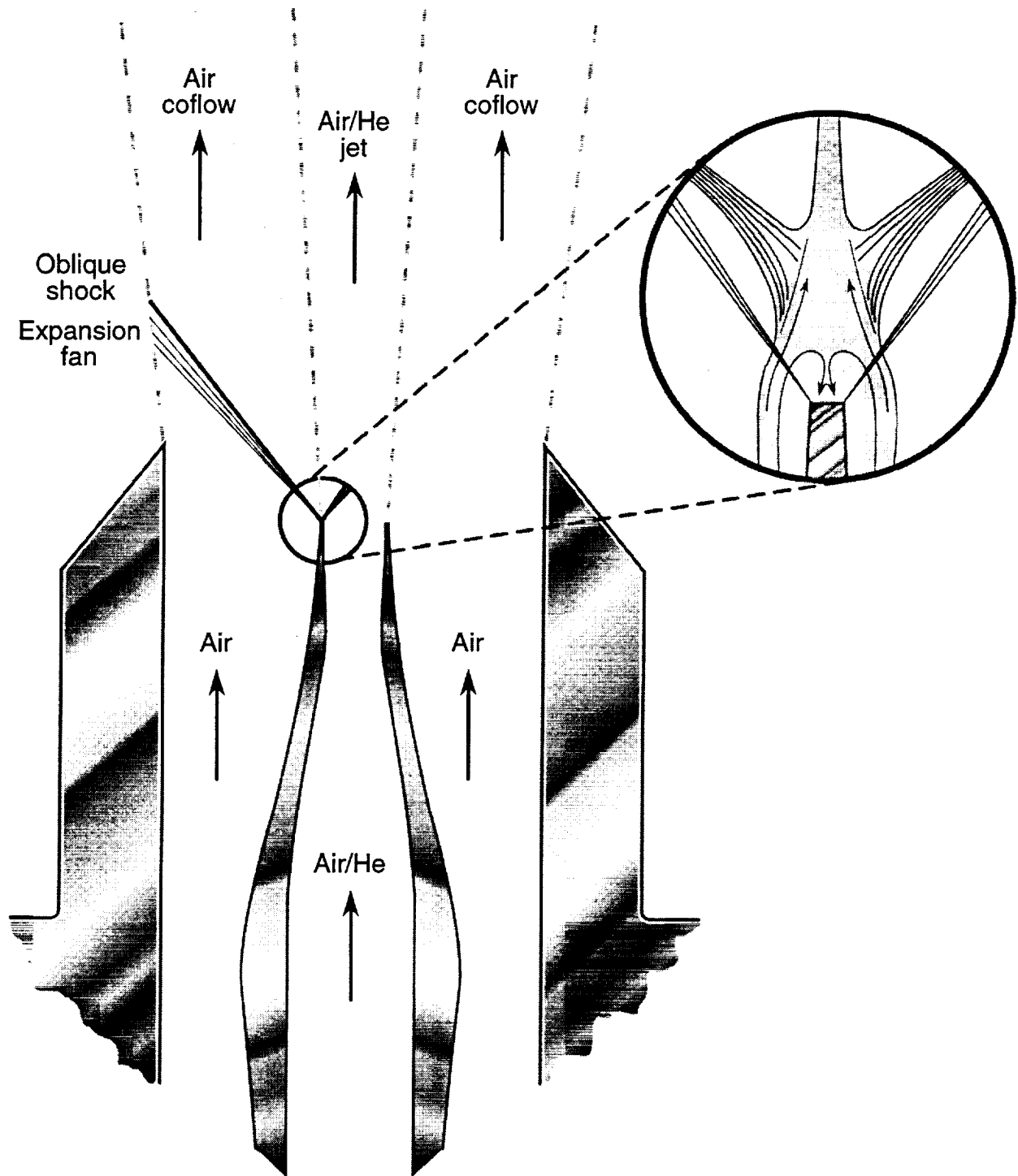


**Figure 28: Centerjet Nozzle Exit Flow Structure**

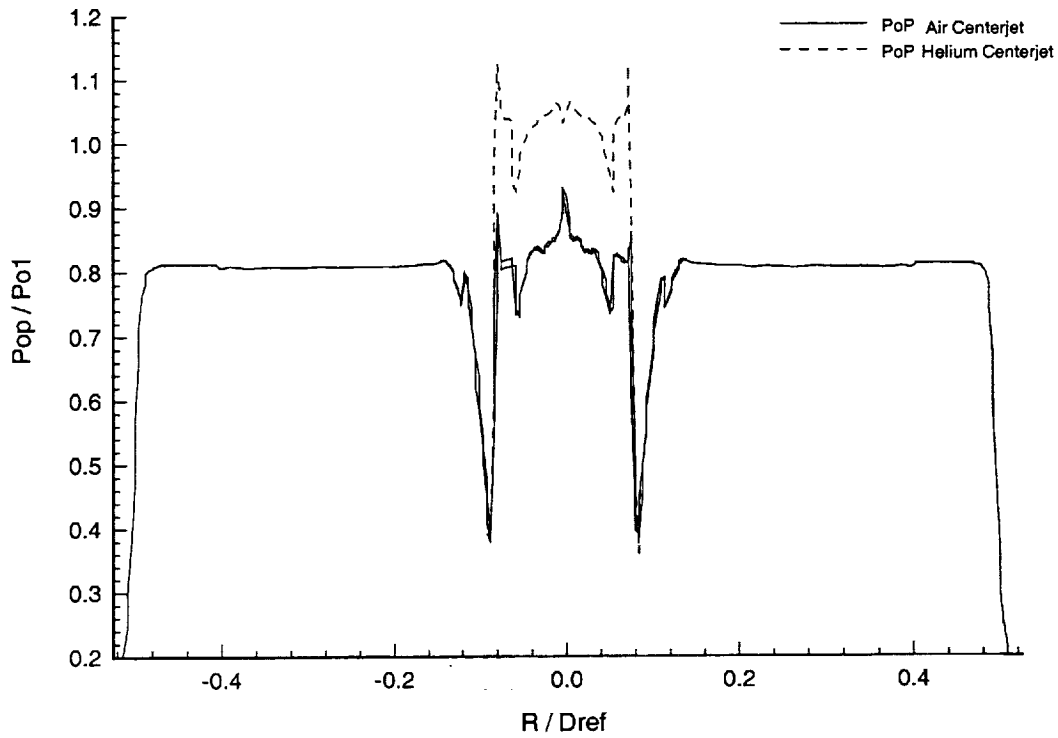


**Figure 29: Pitot Pressure Surveys - 3-4mm**

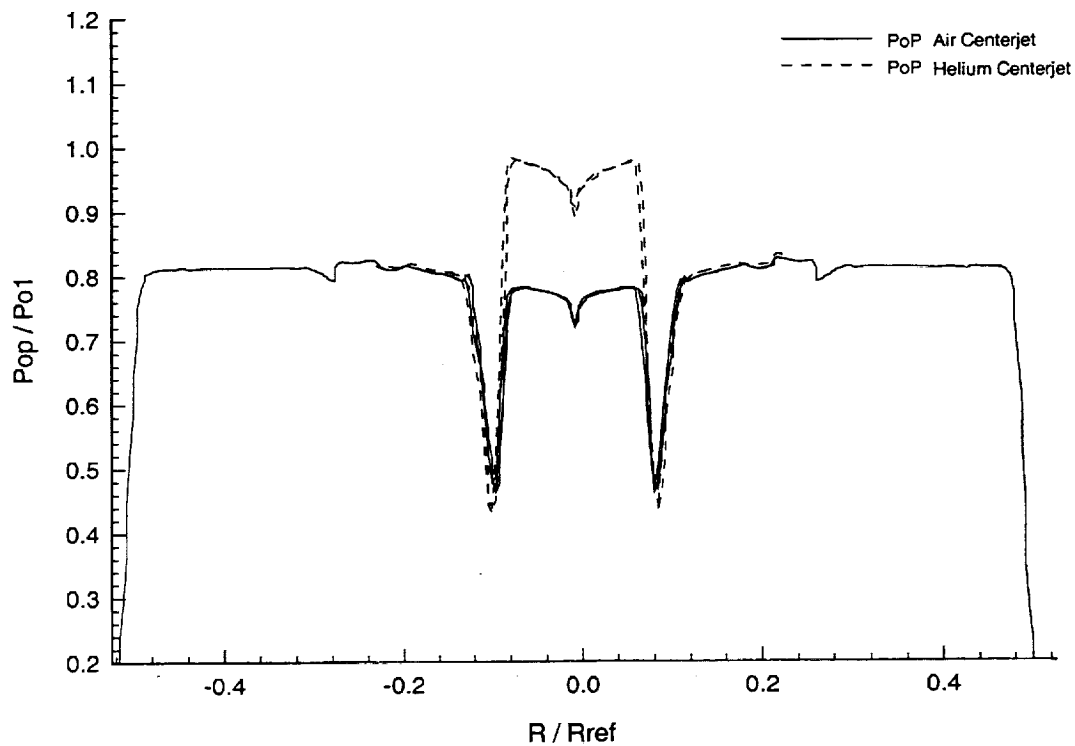


**Figure 30: Pitot Pressure Surveys - 13mm**

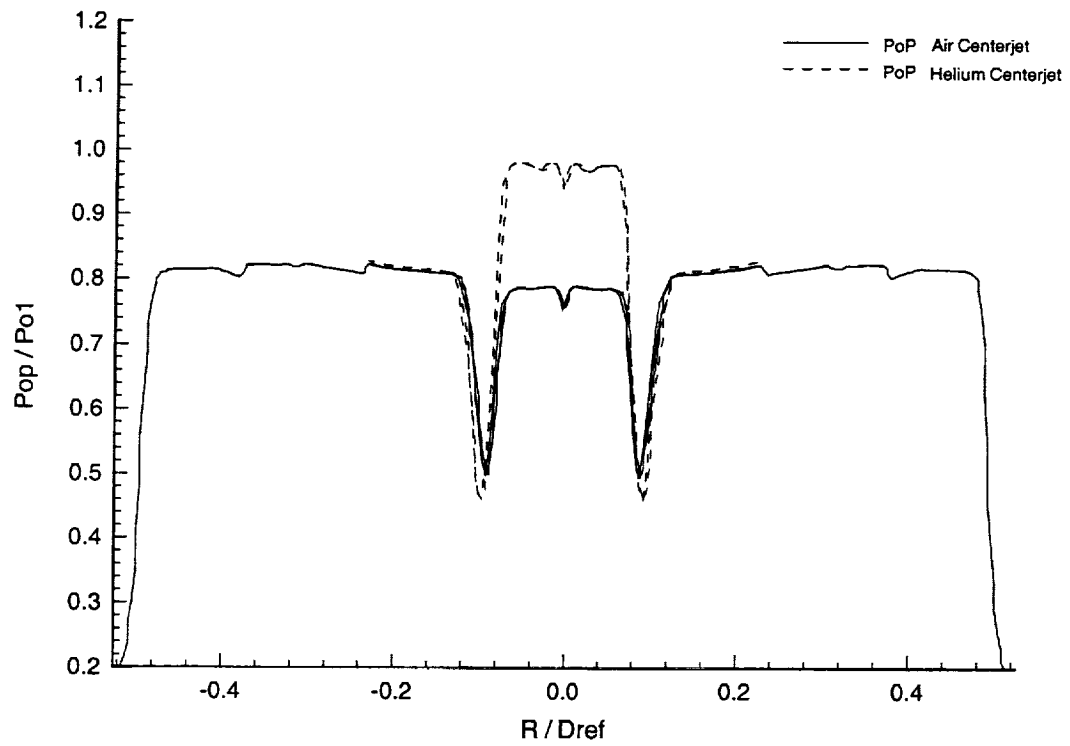


**Figure 31: Pitot Pressure Surveys - 23mm**

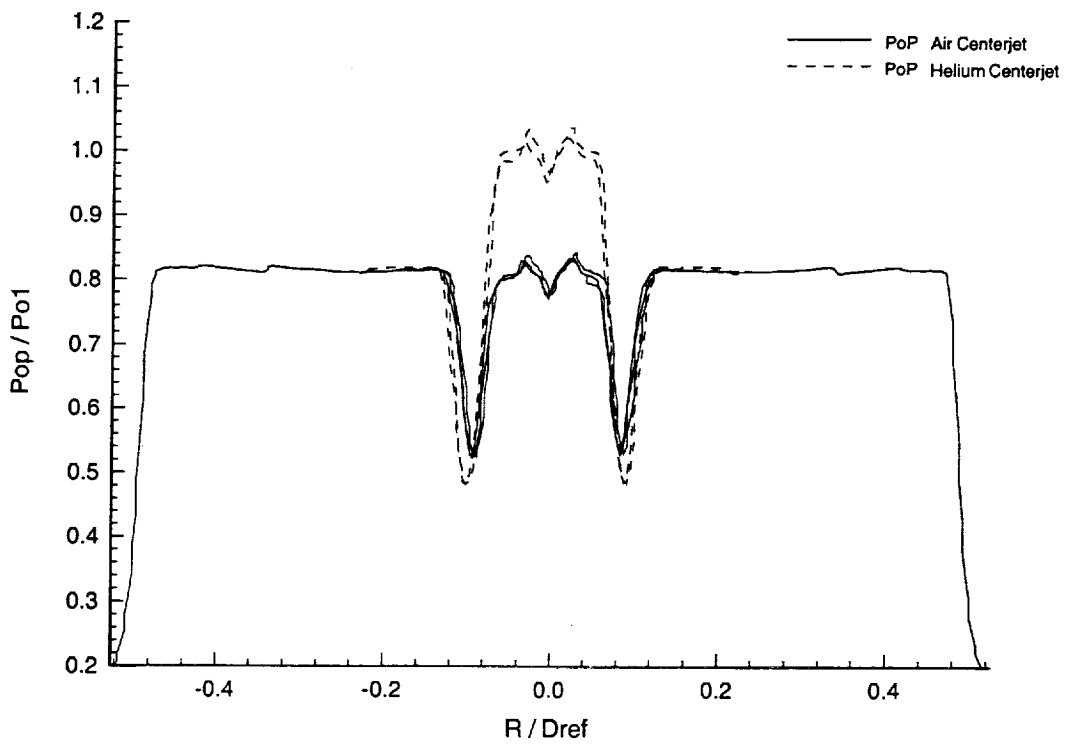


**Figure 32: Pitot Pressure Surveys - 33mm**

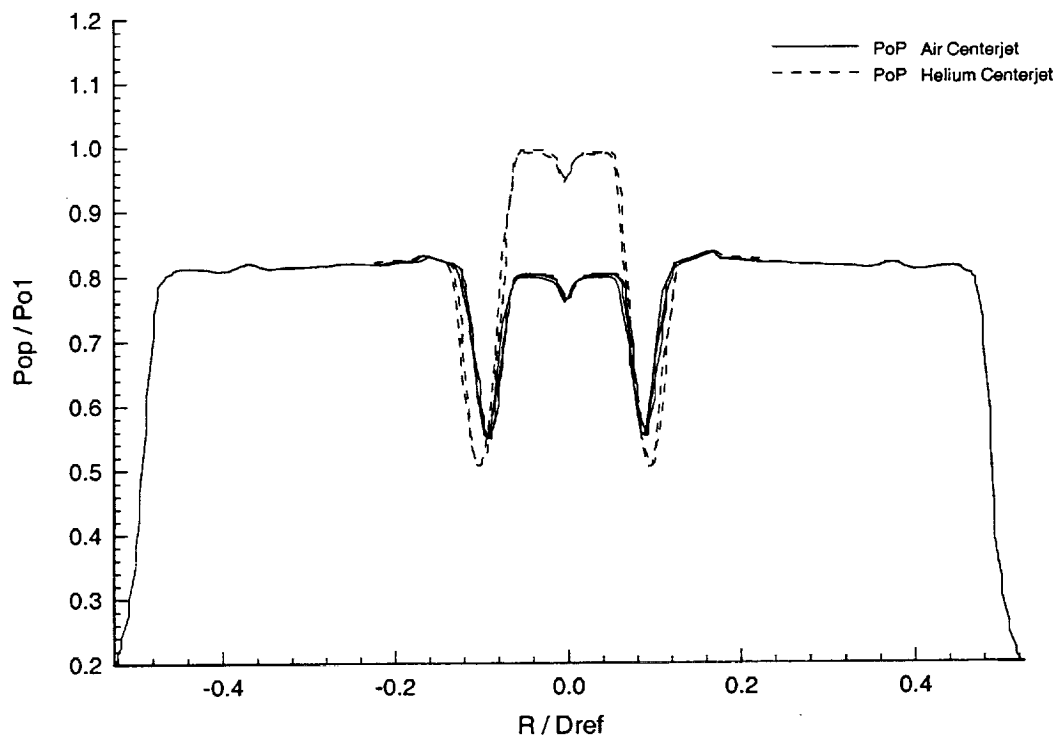


**Figure 33: Pitot Pressure Surveys - 43mm**

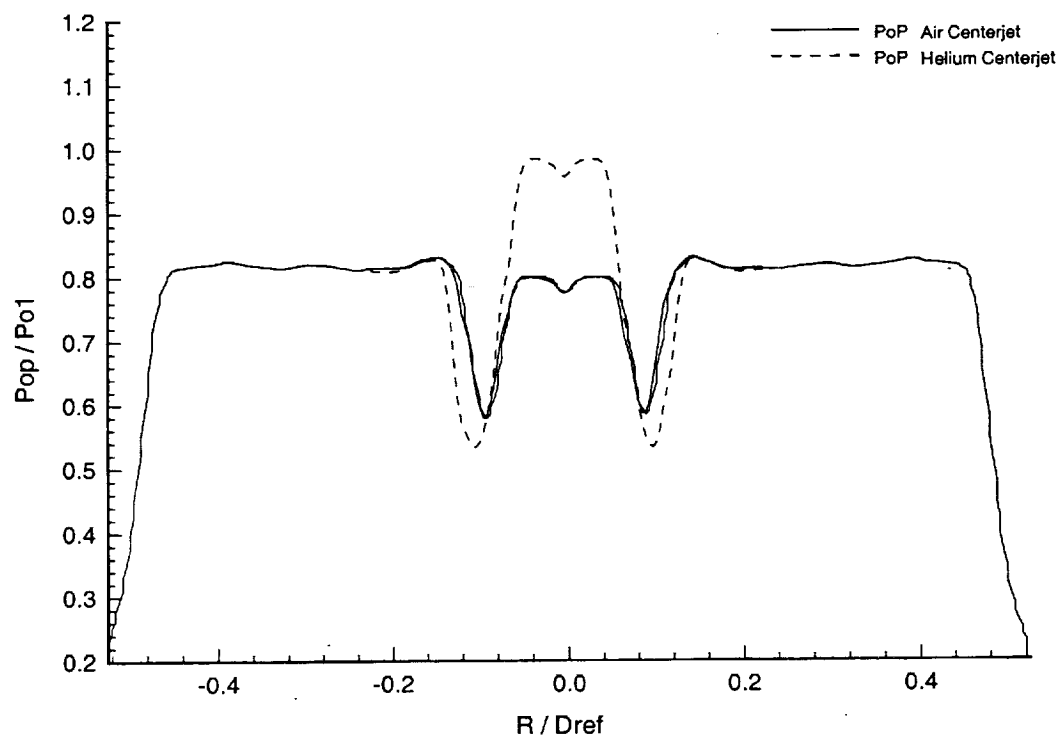


**Figure 34: Pitot Pressure Surveys - 63mm**

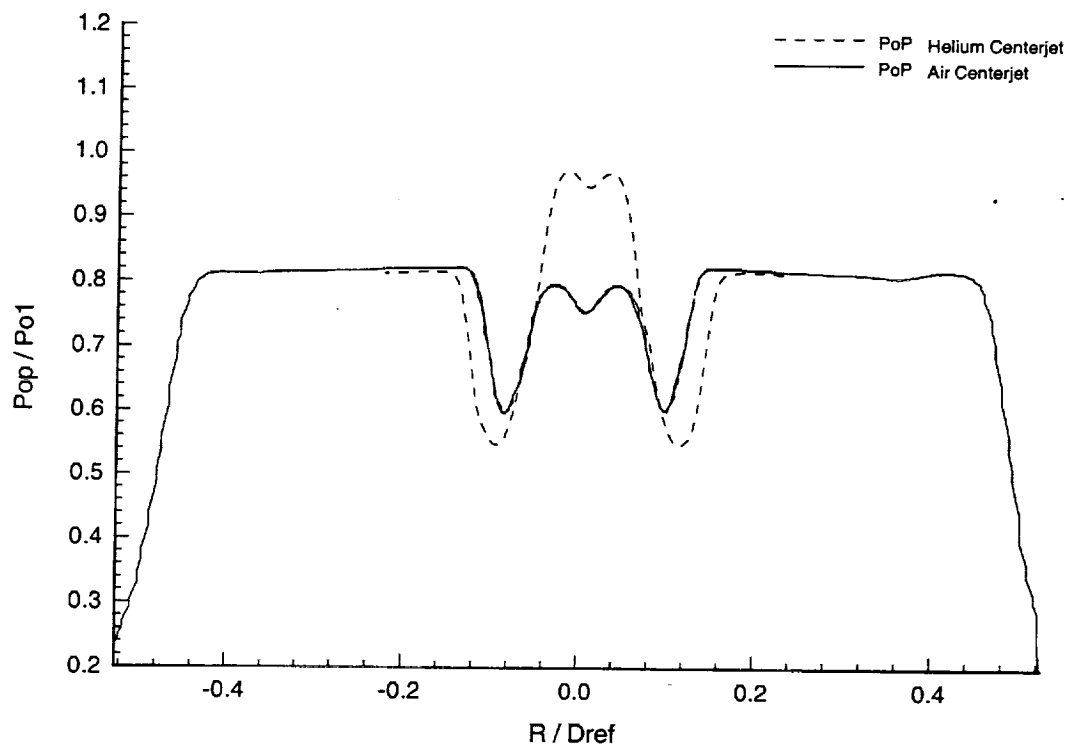


**Figure 35: Pitot Pressure Surveys - 83mm**

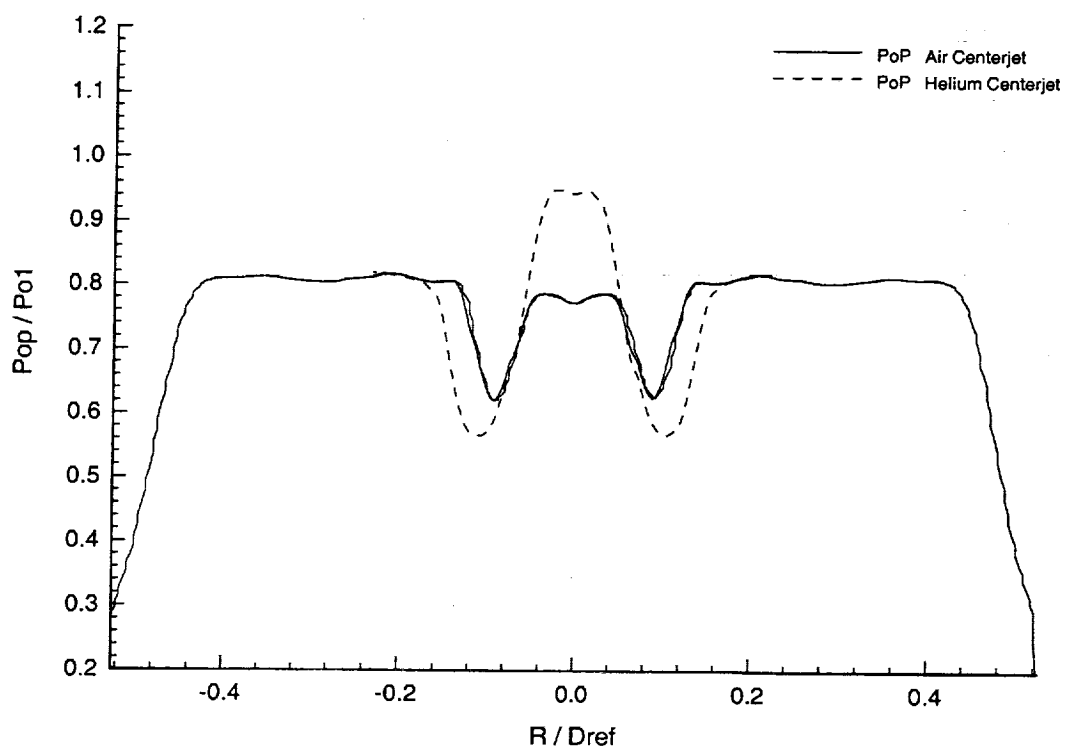


**Figure 36: Pitot Pressure Surveys - 103mm**



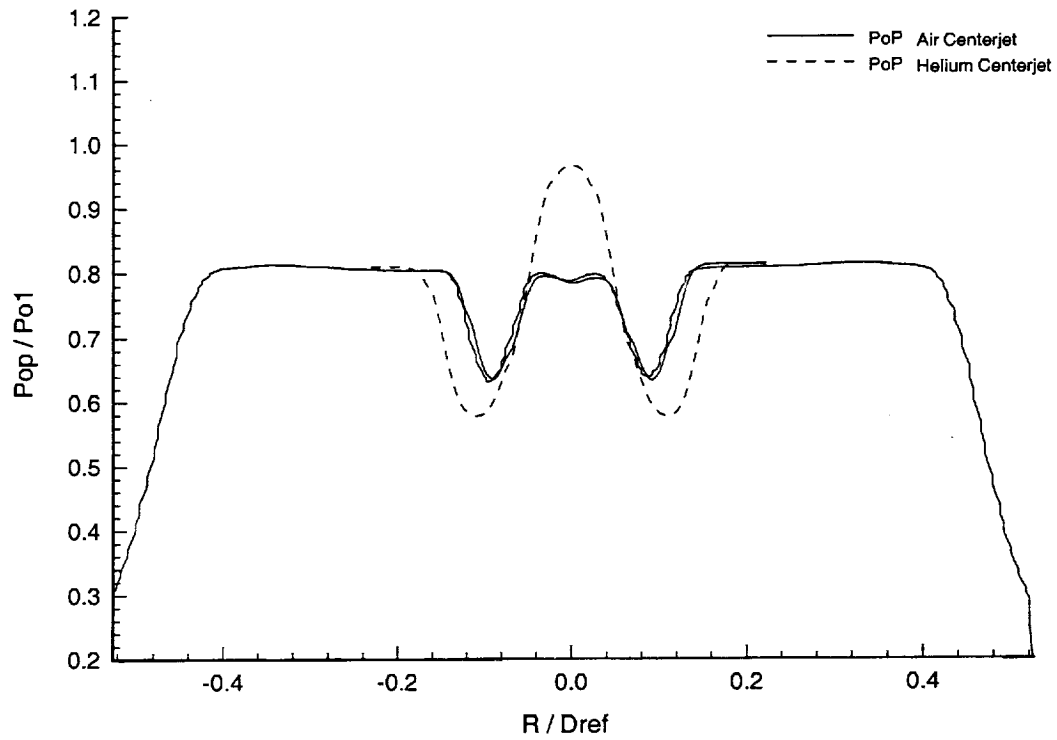


**Figure 37: Pitot Pressure Surveys - 123mm**

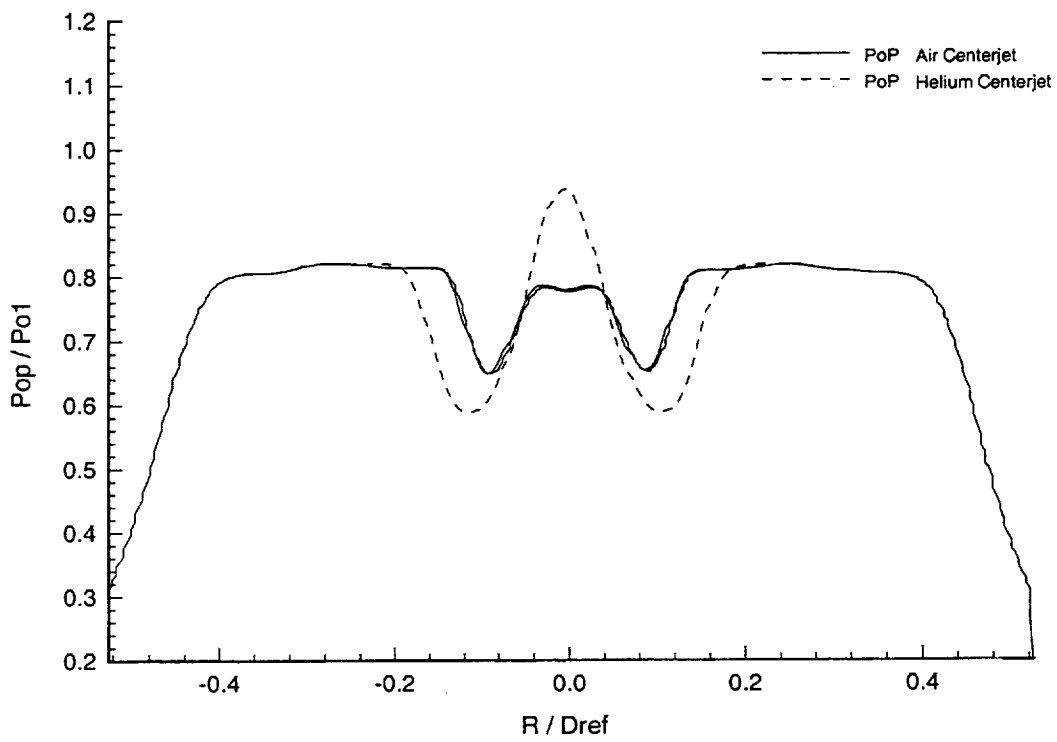


**Figure 38: Pitot Pressure Surveys - 143mm**

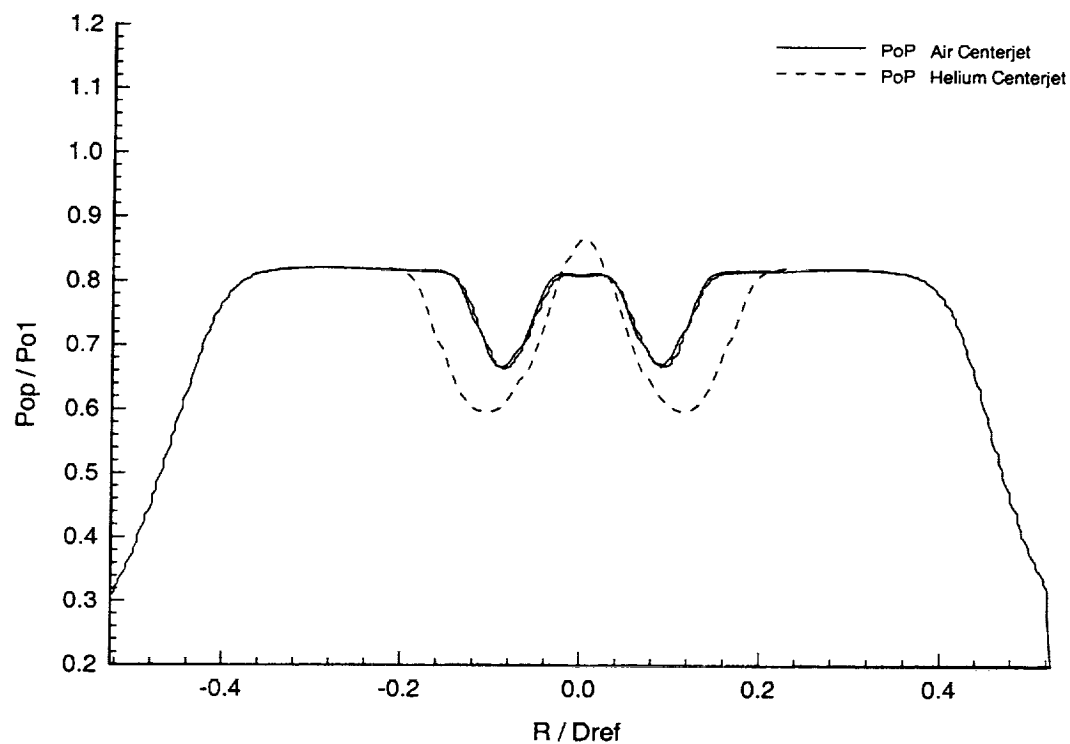


**Figure 39: Pitot Pressure Surveys - 163mm**

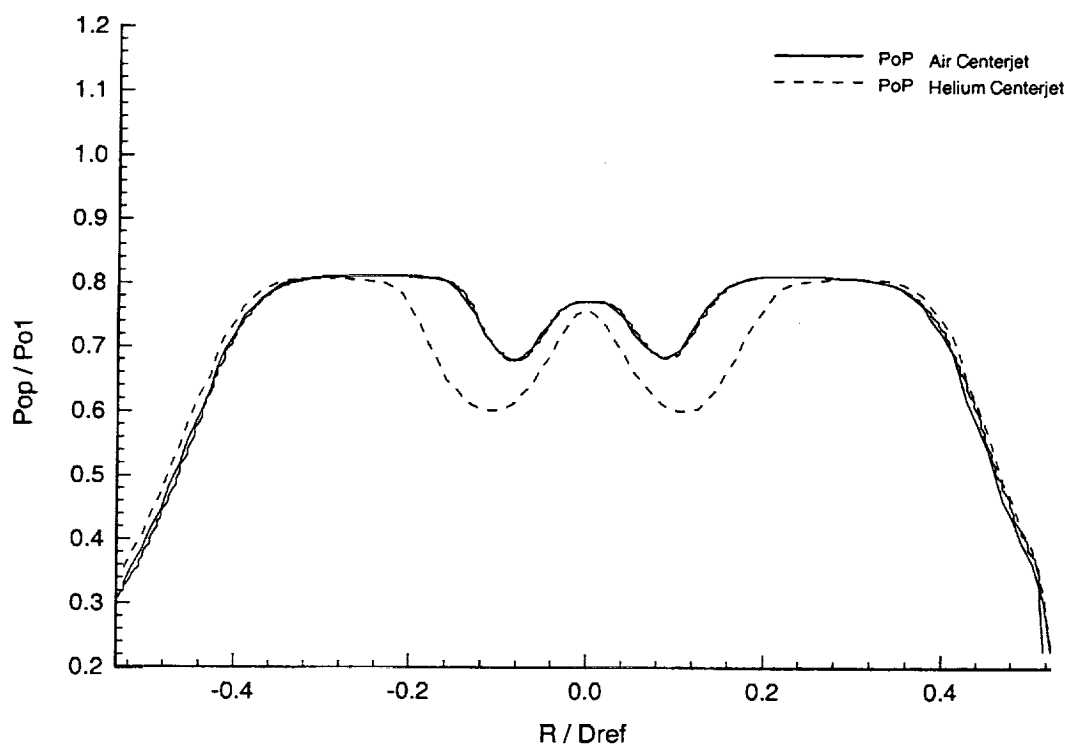


**Figure 40: Pitot Pressure Surveys - 203mm**

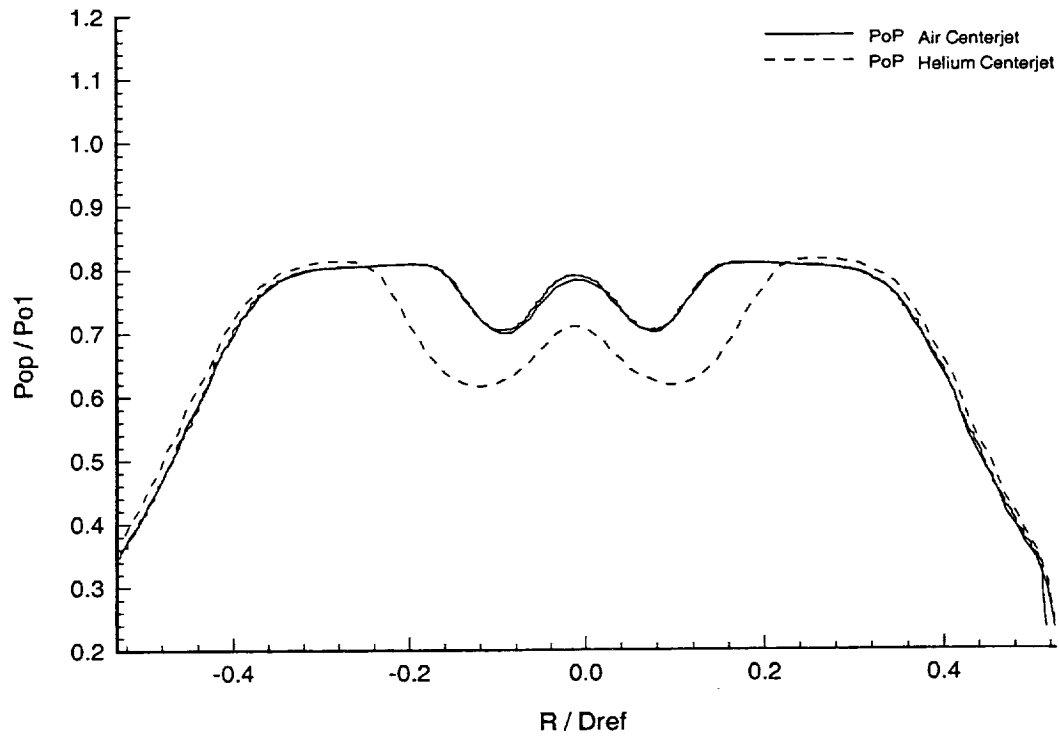


**Figure 41: Pitot Pressure Surveys - 243mm**

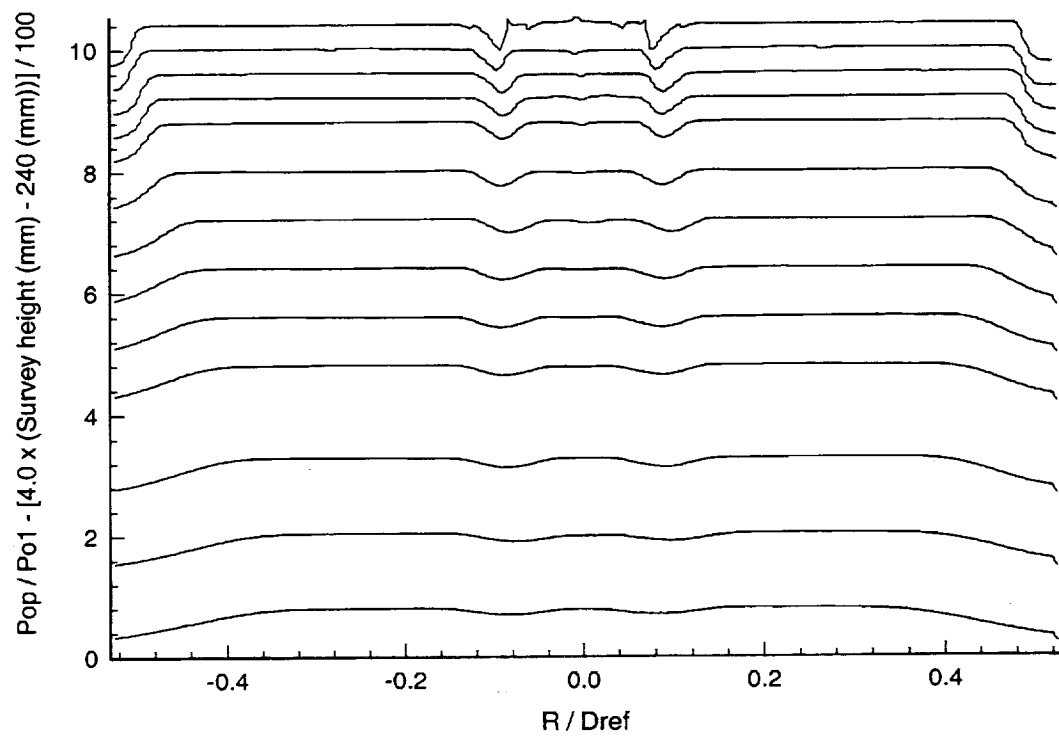


**Figure 42: 400 pt. Air Centerjet Nozzle Surveys - 3mm through 243mm**

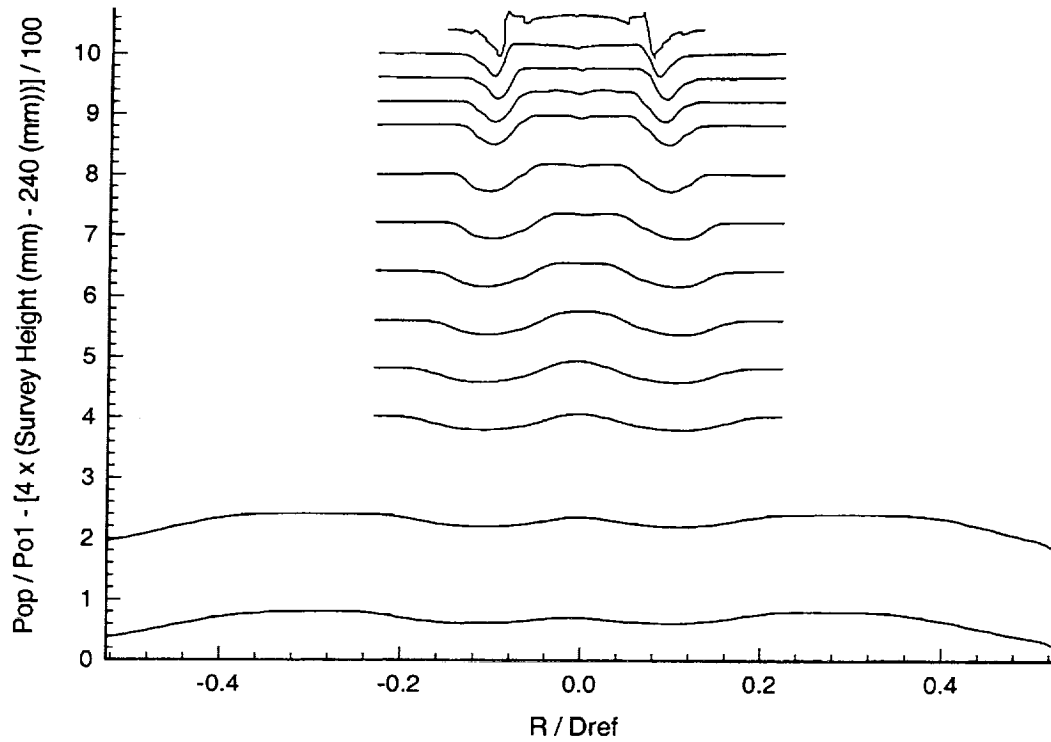


**Figure 43: 100 pt. Helium Centerjet Nozzle Surveys - 3mm through 243 mm**

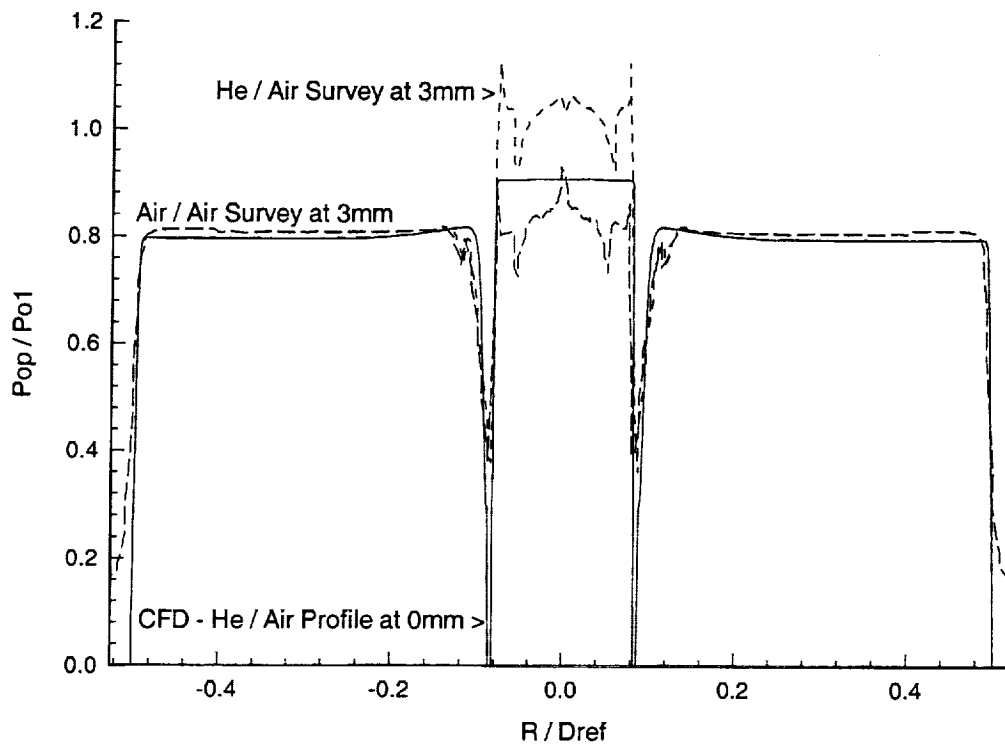


**Figure 44: Comparison of CFD and Experimental Survey Results at Exit Plane**

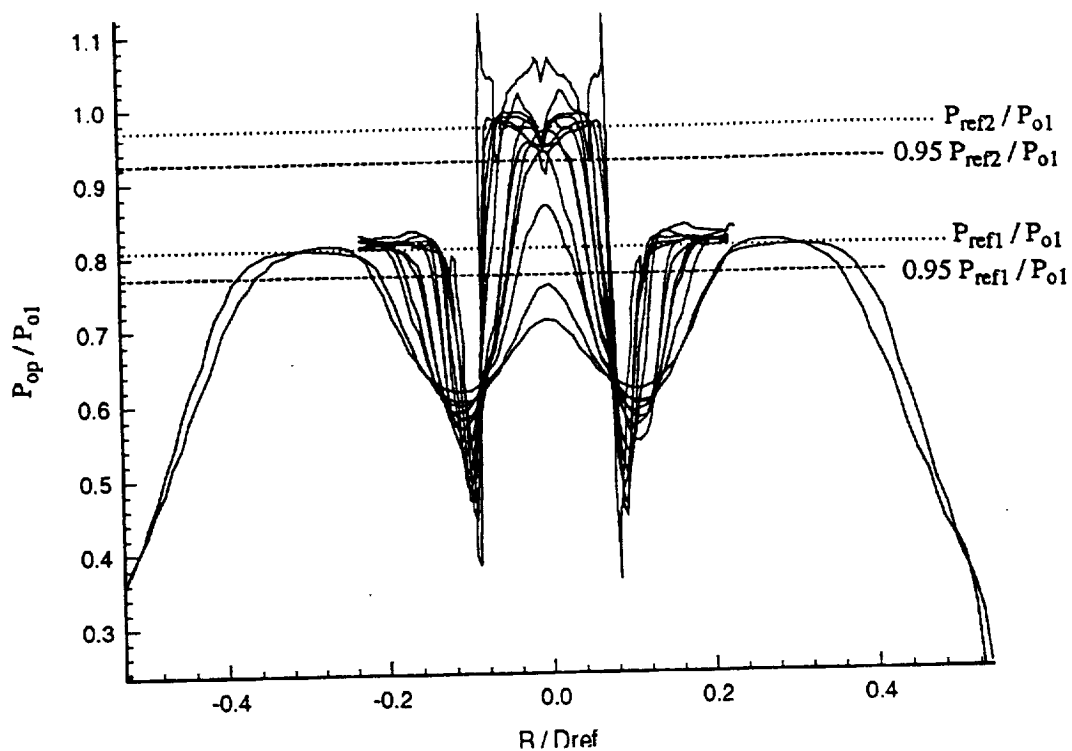


**Figure 45: Helium Centerjet Nozzle Surveys with Specified Reference Planes**

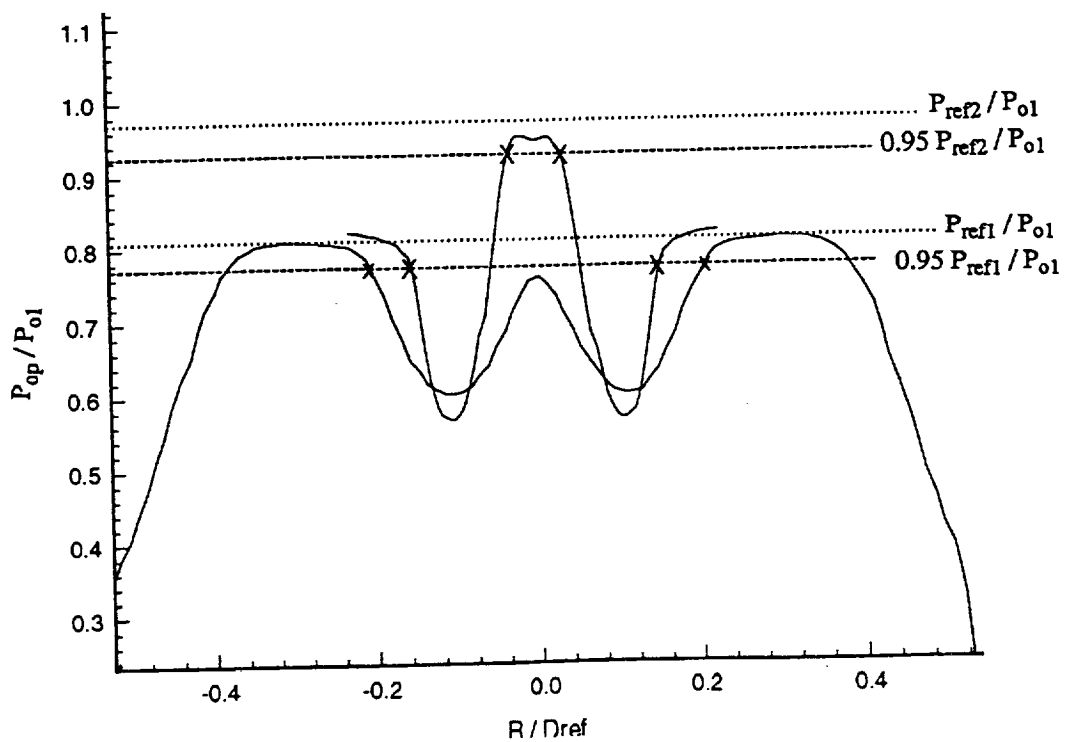


**Figure 46: Helium Centerjet Nozzle Surveys - Definition of Mixing Layer Edges**

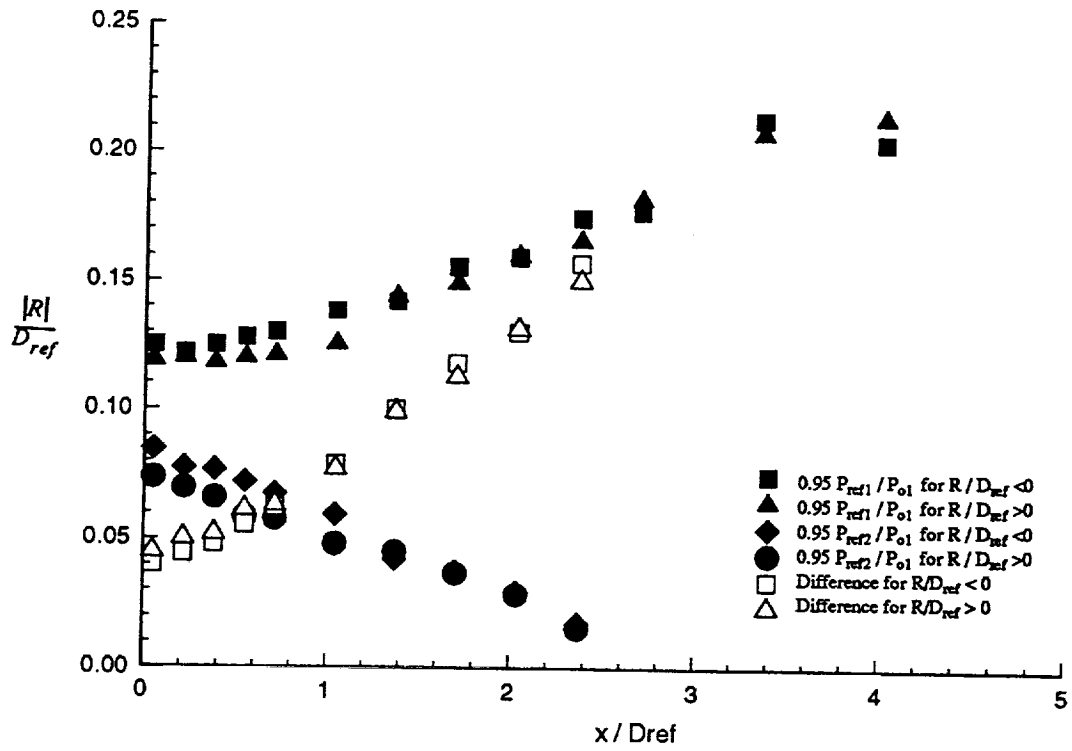


Figure 47: Coannular Jet Growth

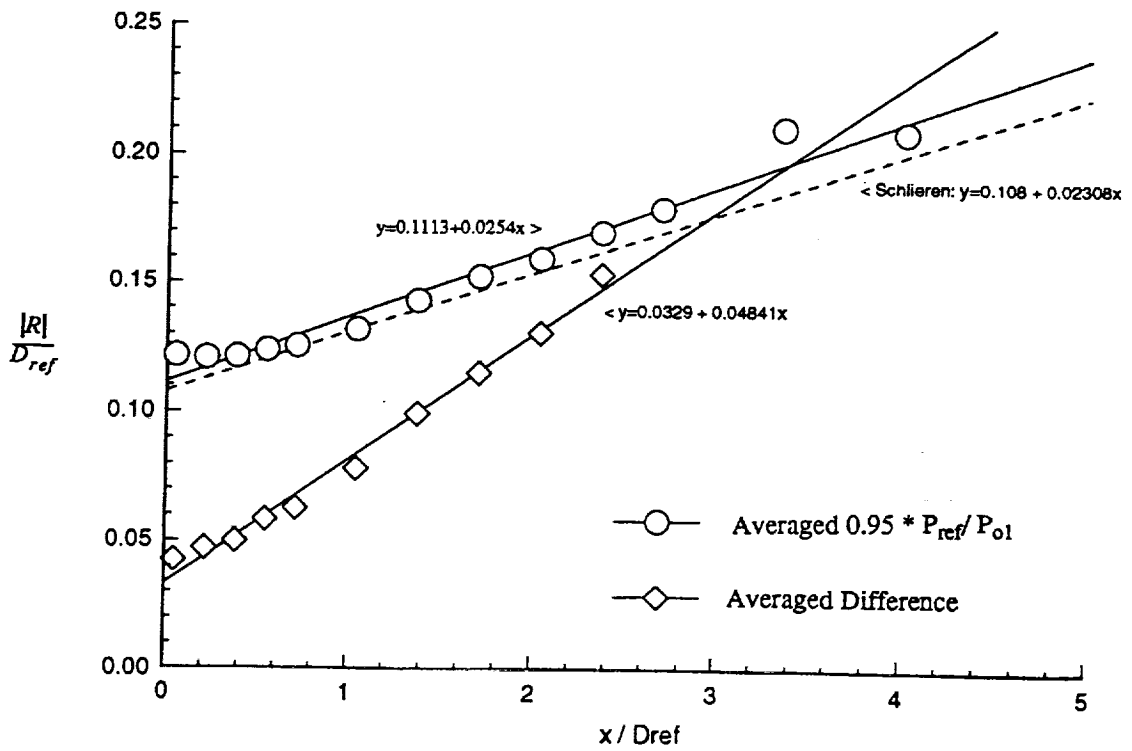
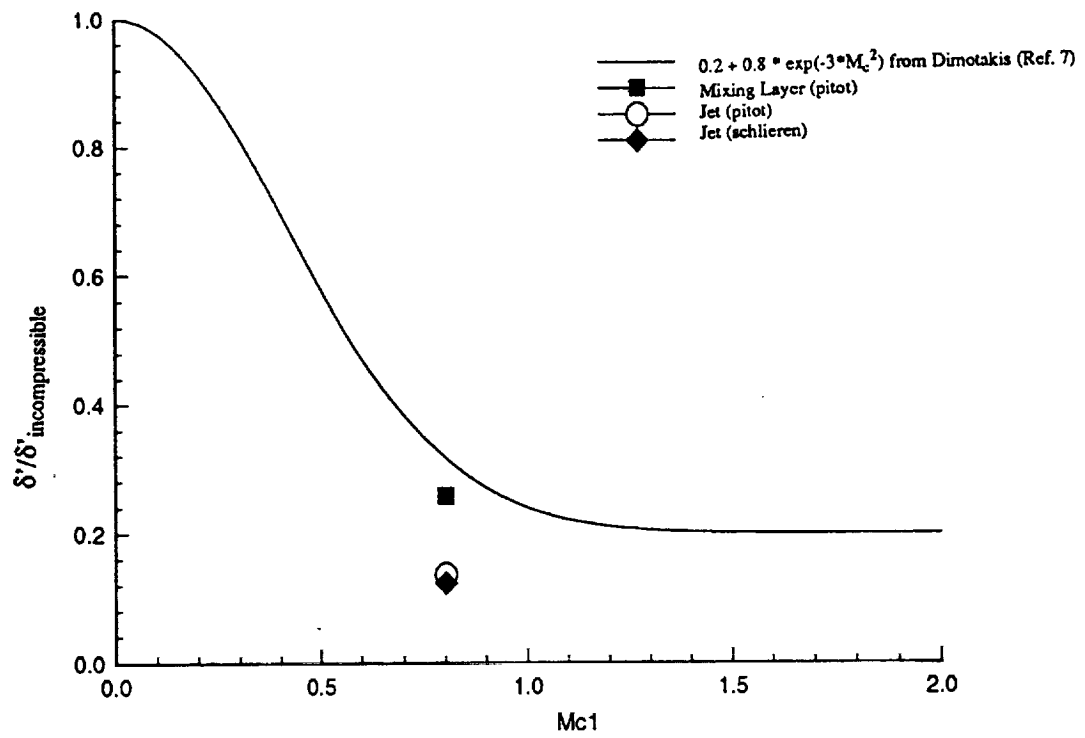
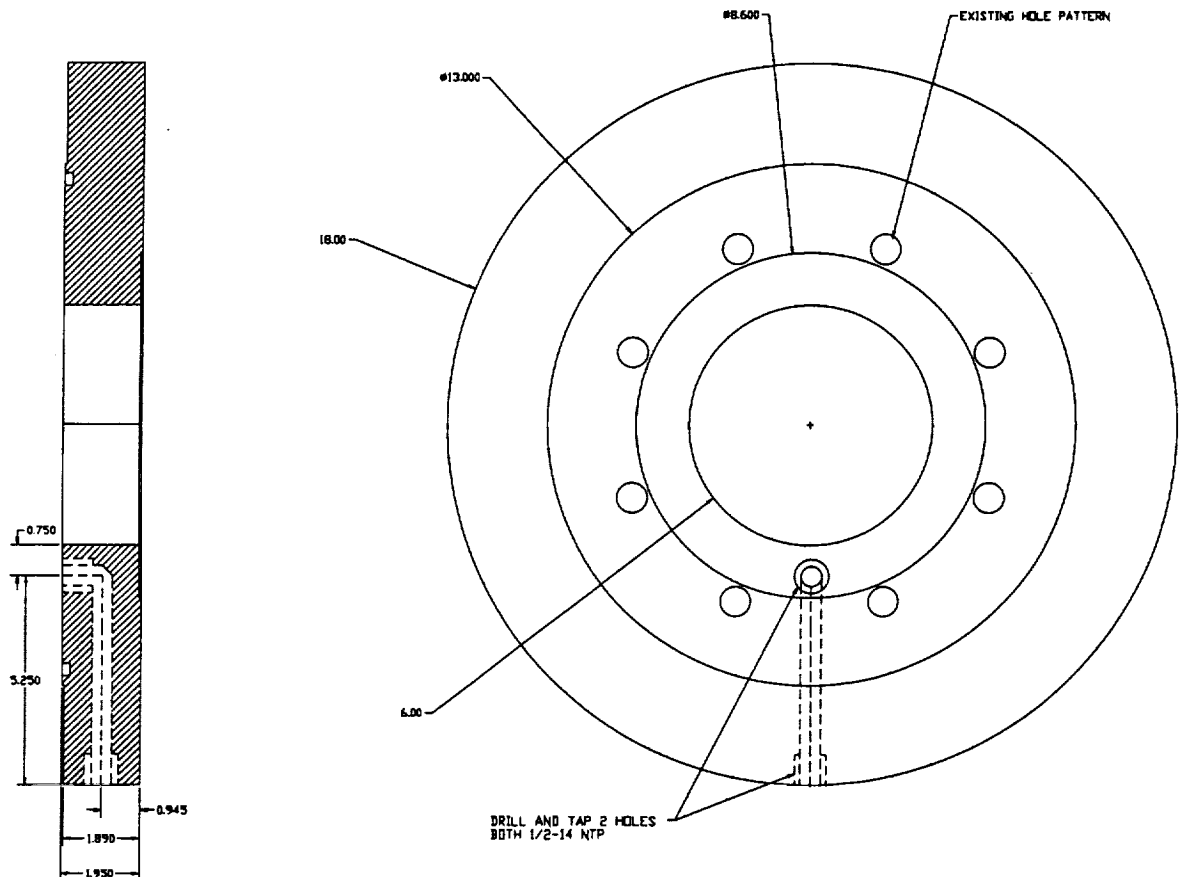


Figure 48: Averaged Coannular Jet Growth



**Figure 49: Normalized Spreading Rate Comparison with Dimotakis Correlation**



COAXIAL NOZZLE
MODIFICATION TO EXISTING ADAPTOR FLANGE
<ul style="list-style-type: none"> <li>✱ ALL DIMENSIONS IN INCHES</li> <li>✱ MATERIAL IS STAINLESS STEEL</li> </ul>
DRILL AND TAP 1/2-14 NPT ON SPCKET FACE AS WELL AS FROM OUTER WALL RADIALY INTO FLANGE IN ORDER TO OBTAIN A 0.5 DIA. FLOW CHANNEL THROUGH FLANGE.

**Figure 50: Transverse Jet Facility Adaptor**



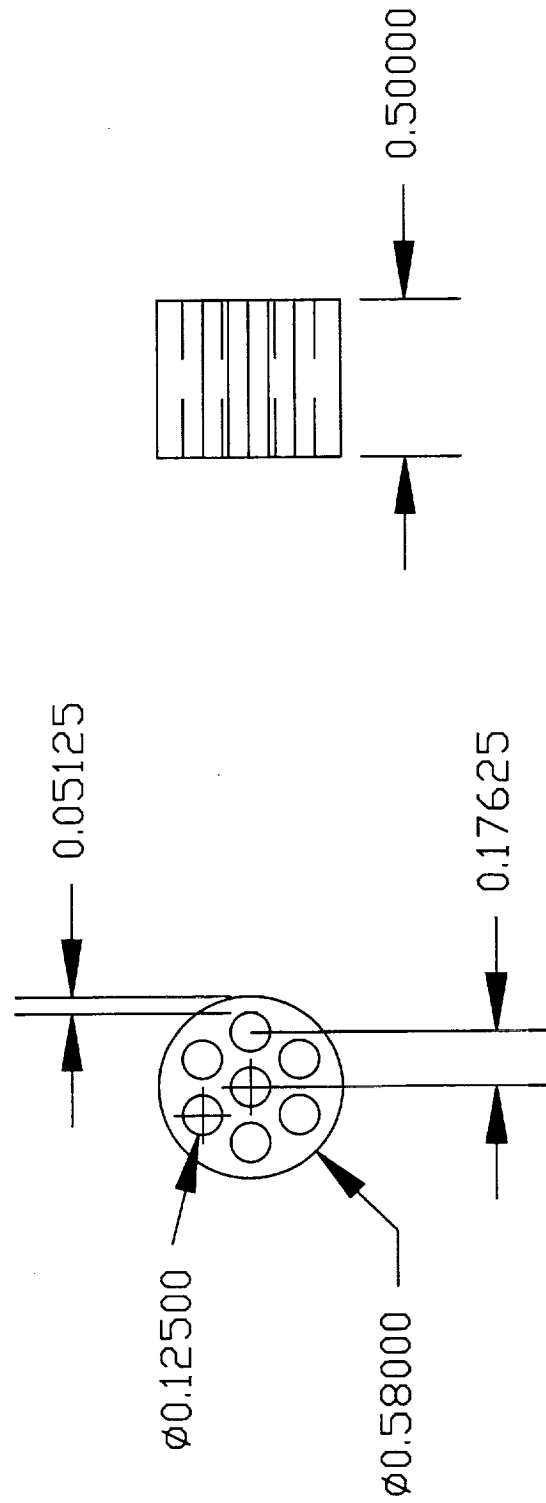
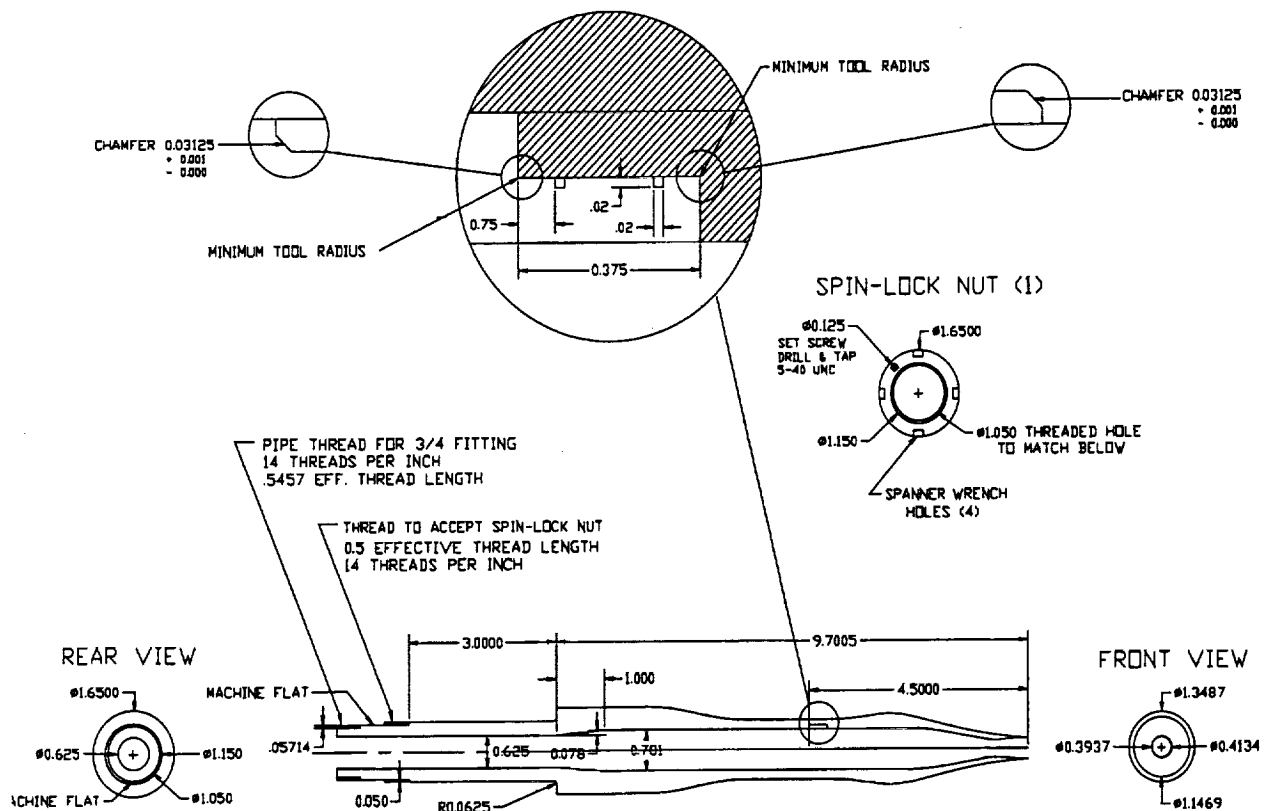


**Figure 51:Centerjet Flow Straightener**





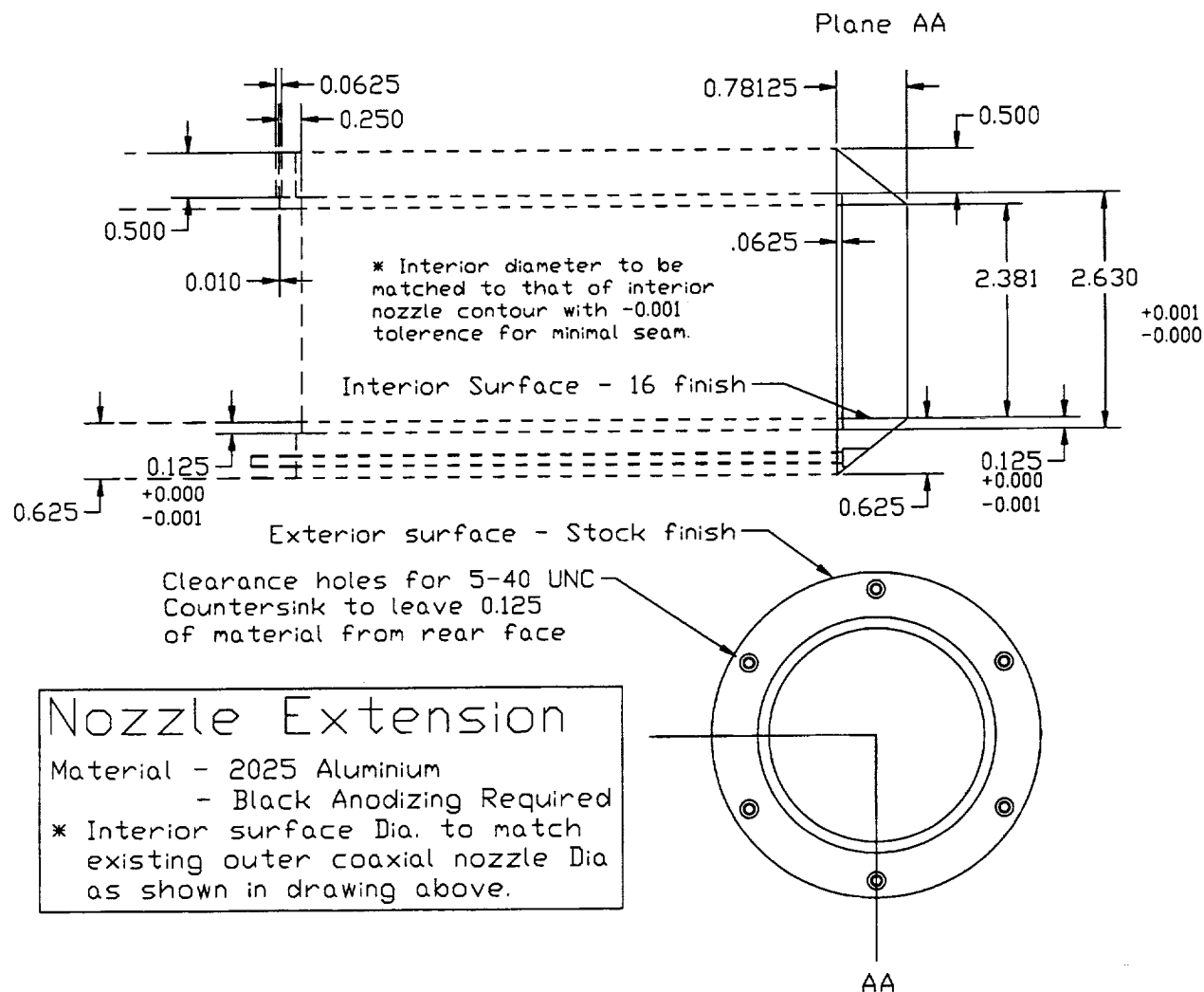
COAXIAL NOZZLE DRAWN BY > ATHERTON CARTY.  
864-6240

### INNER NOZZLE AND SPIN-LOCK NUT

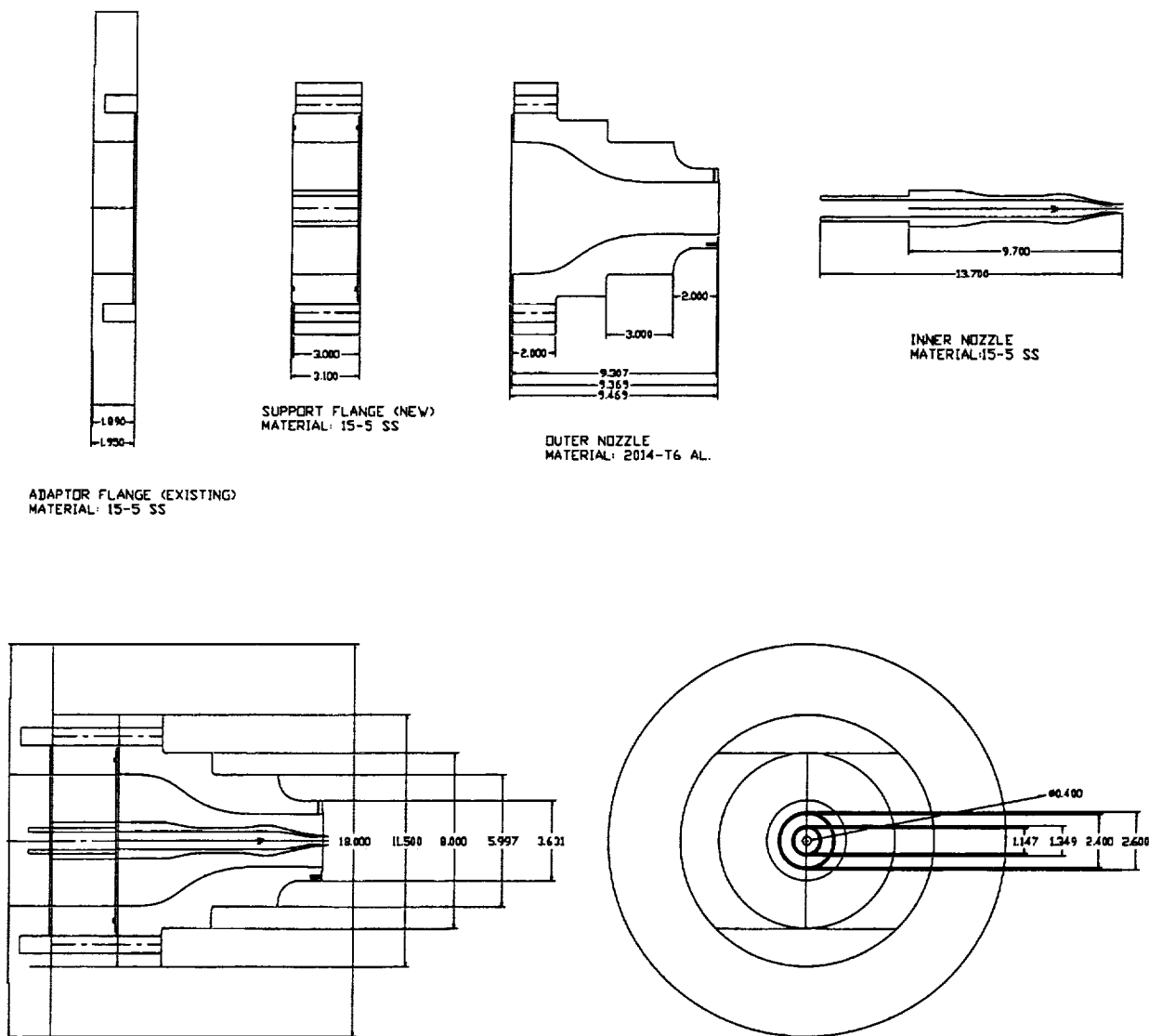
- \*FINISHED NOZZLE REQUIRES COPPER BRAZE OF 2 COMPONENTS
- NOZZLE HEAD REQUIRES 16 FINISH .001 OF CONTOURED SURF.
- NOZZLE SHAFT REQUIRES 32 FINISH .001 OF WALL SURFACES
- \*MATERIAL IS 15-5PH SS
- \*HEAT TREAT TO 1025
- \*ALL DIMENSIONS IN INCHES
- \*NOZZLE CONTOUR POINTS PROVIDED SEPERATELY ON DISC
- EXTERIOR CONTOUR POINTS IN FILE 'CMIDDLE.DAT'
- INTERIOR CONTOUR POINTS IN FILE 'CINNER.DAT'

Figure 53:Centerbody





**Figure 55: Coflow Nozzle Extension Cap**



**Figure 56: Model Assembly Drawing**

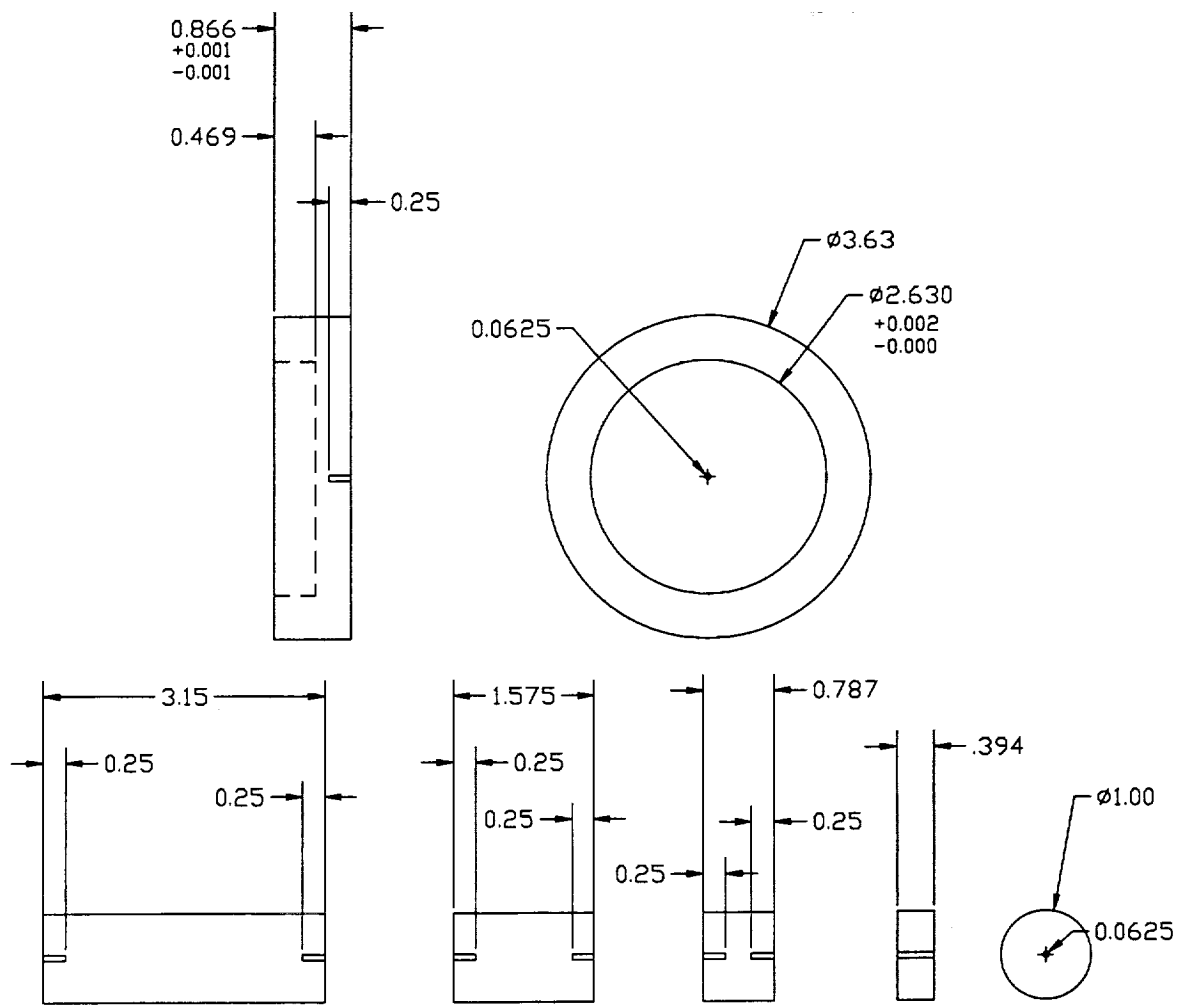


**Figure 57:Alignment Hardware**

REPORT DOCUMENTATION PAGE			Form Approved OMB No. 0704-0188	
Public reporting burden for this collection of information is estimated to average 1 hour per response, including the time for reviewing instructions, searching existing data sources, gathering and maintaining the data needed, and completing and reviewing the collection of information. Send comments regarding this burden estimate or any other aspect of this collection of information, including suggestions for reducing this burden, to Washington Headquarters Services, Directorate for Information Operations and Reports, 1215 Jefferson Davis Highway, Suite 1204, Arlington, VA 22202-4302, and to the Office of Management and Budget, Paperwork Reduction Project (0704-0188), Washington, DC 20503				
1. AGENCY USE ONLY (Leave blank)		2. REPORT DATE November 1999		3. REPORT TYPE AND DATES COVERED Contractor Report
4. TITLE AND SUBTITLE Development and Validation of a Supersonic Helium-Air Coannular Jet Facility			5. FUNDING NUMBERS  NCC1-217 522-51-31-10	
6. AUTHOR(S) Atherton A. Carty and Andrew D. Cutler				
7. PERFORMING ORGANIZATION NAME(S) AND ADDRESS(ES) The George Washington University Joint Institute for Advancement of Flight Sciences NASA Langley Research Center Hampton, VA 23681-2199			8. PERFORMING ORGANIZATION REPORT NUMBER	
9. SPONSORING/MONITORING AGENCY NAME(S) AND ADDRESS(ES)  National Aeronautics and Space Administration Langley Research Center Hampton, VA 23681-2199			10. SPONSORING/MONITORING AGENCY REPORT NUMBER  NASA/CR-1999-209717	
11. SUPPLEMENTARY NOTES The information submitted in this report was offered as a thesis by the first author in partial fulfillment of the requirements for the Degree of Master of Science, The George Washington University, JIAFS. Langley Technical Monitor: Glenn S. Diskin				
12a. DISTRIBUTION/AVAILABILITY STATEMENT Unclassified-Unlimited Subject Category 07                      Distribution: Standard Availability: NASA CASI (301) 621-0390			12b. DISTRIBUTION CODE	
13. ABSTRACT (Maximum 200 words) Data are acquired in a simple coannular He/air supersonic jet suitable for validation of CFD codes for high speed propulsion. Helium is employed as a non-reacting hydrogen fuel simulant, constituting the core of the coannular flow while the coflow is composed of air. The mixing layer interface between the two flows in the near field and the plume region which develops further downstream constitute the primary regions of interest, similar to those present in all hypersonic air breathing propulsion systems. A computational code has been implemented from the experiment's inception, serving as a tool for model design during the development phase.				
14. SUBJECT TERMS High speed mixing, supersonic mixing, coaxial jets, coannular jets			15. NUMBER OF PAGES 114	
			16. PRICE CODE A06	
17. SECURITY CLASSIFICATION OF REPORT Unclassified	18. SECURITY CLASSIFICATION OF THIS PAGE Unclassified	19. SECURITY CLASSIFICATION OF ABSTRACT Unclassified	20. LIMITATION OF ABSTRACT UL	